Microwire crossbar arrays for chemical, mechanical, and thermal stimulation of cells

Philipp Rinklin

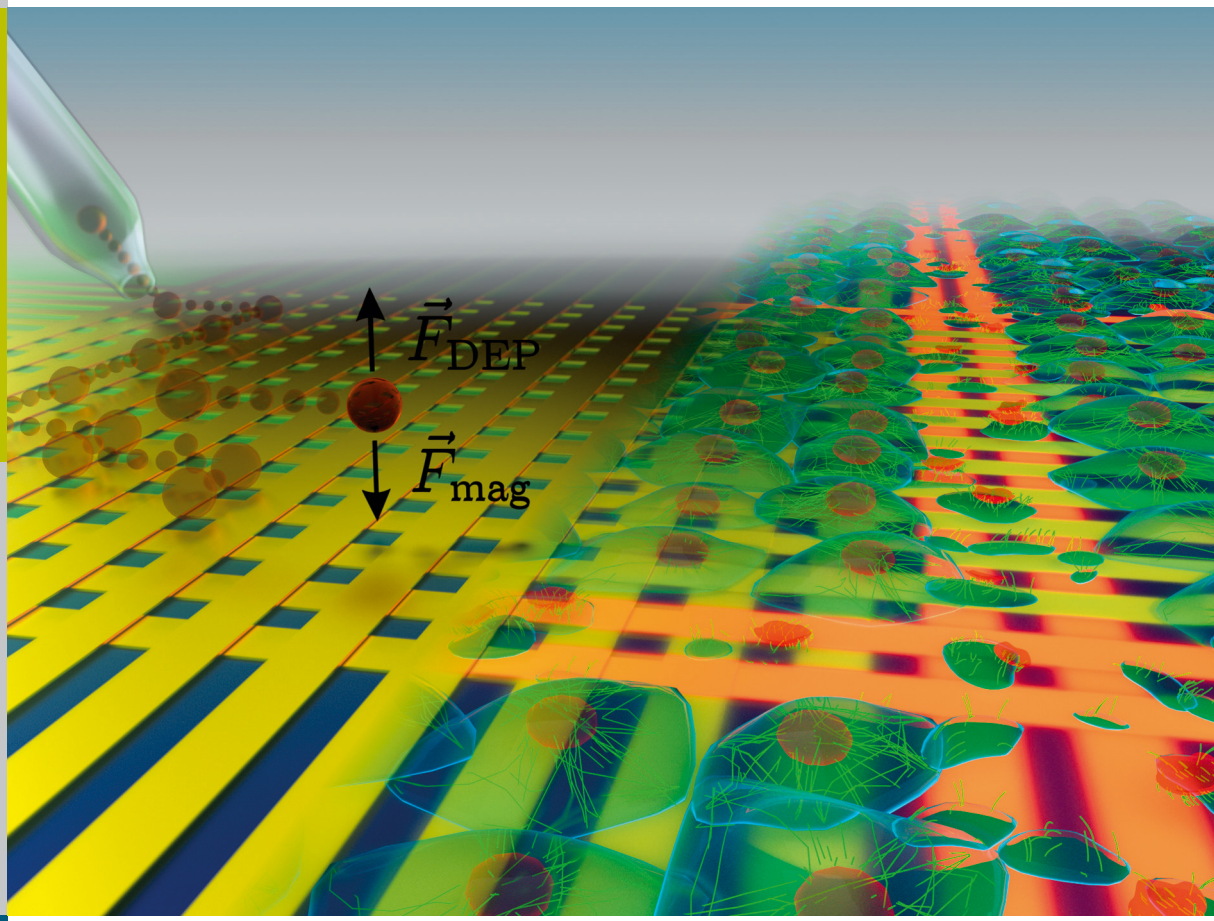

Schlüsseltechnologien / Key Technologies
Band / Volume 100
ISBN 978-3-95806-022-7

JÜLICH FORSCHUNGSZENTRUM

Schriften des Forschungszentrums Jülich
Reihe Schlüsseltechnologien / Key Technologies Band / Volume 100

Forschungszentrum Jülich GmbH
Peter Grünberg Institute / Institute of Complex Systems
Bioelectronics (PGI-8 / ICS-8)

Microwire crossbar arrays for chemical, mechanical, and thermal stimulation of cells

Philipp Rinklin

Schriften des Forschungszentrums Jülich
Reihe Schlüsseltechnologien / Key Technologies Band / Volume 100

ISSN 1866-1807 ISBN 978-3-95806-022-7

Bibliographic information published by the Deutsche Nationalbibliothek.
The Deutsche Nationalbibliothek lists this publication in the Deutsche Nationalbibliografie; detailed bibliographic data are available in the Internet at http://dnb.d-nb.de.

Publisher and Distributor: Forschungszentrum Jülich GmbH
Zentralbibliothek
52425 Jülich
Tel: +49 2461 61-5368
Fax: +49 2461 61-6103
Email: zb-publikation@fz-juelich.de
www.fz-juelich.de/zb

Cover Design: Grafische Medien, Forschungszentrum Jülich GmbH

Printer: Grafische Medien, Forschungszentrum Jülich GmbH

Schriften des Forschungszentrums Jülich
Reihe Schlüsseltechnologien / Key Technologies, Band / Volume 100

D 82 (Diss. RWTH Aachen University, 2014)

ISSN 1866-1807
ISBN 978-3-95806-022-7

The complete volume is freely available on the Internet on the Jülicher Open Access Server (JuSER) at www.fz-juelich.de/zb/openaccess.

ZUSAMMENFASSUNG

Miniaturisierte biophysikalische Werkzeuge, auch als *lab-on-a-chip* oder *micro-total-analysis-systems* bekannt, sind in den letzten zwei Jahrzehnten zu einem lebhaften Bereich interdisziplinärer Forschung geworden. Diese Entwicklung liegt darin begründet, dass solche Werkzeuge einen verringerten Bedarf an Material und Zeit versprechen. Gleichzeitig bieten sie eine Auflösung an, die mit klassischen Methoden oftmals nicht zu erreichen ist. In diesem Zusammenhang untersucht die vorliegende Arbeit die Verwendung von orthogonalen Mikrodrahtarrays zur chemischen, mechanischen und thermischen Stimulation von biologischen Zellen.

Der erste Teil der Arbeit betrifft den Einsatz magnetischer Mikropartikel als Träger chemischer und mechnischer Stimuli. An dieser Stelle wird ein chip-basierter Ansatz zur präzisen Kontrolle dieser Partikel untersucht. Zu diesem Zweck werden die oben erwähnten Mikrodrahtarrays als miniaturisierte Elektromagnete zur Generierung hochlokalisierter magnetischer Felder genutzt. Diese Felder werden wiederum zur Ausübung präziser Kontrolle über mangetische Mikropartikel verwendet. Um ein erfolgreiches Absetzen der Partikel sicherzustellen werden simple aber effiziente Protokolle zum Transport besagter Partikel un-

tersucht. Bezüglich der Anwendung dieser Protokolle wird ein neuer Ansatz zum Absetzen und zur Kontrolle individueller Partikel vorgestellt. Diese Methode eliminiert das Risiko ungewollter Partikellieferung zu einer anderen als der Zielzelle und erlaubt dadurch die kontrollierte und verlässliche Stimulation einzelner Zellen. Zur Demonstration der exzellenten Kontrolle über den Partikel wird eine analytische Simulation des Systems mit experimentellen Daten verglichen. Letztere werden unter Verwendung eines Bildverarbeitungsalgorithmus erhalten, der eine Detektion des Partikels mit Submikrometerauflösung erlaubt.

Im zweiten Teil der Arbeit wird die parallele Erzeugung magnetischer und dielektrophoretischer Kräfte als ein Mittel zur Vermeidung adhesiver Partikel-Oberflächeninteraktion untersucht. Unter Verwendung von Simulationen mittels der Methode finiter Elemente, werden die von den Arrays erzeugten magnetischen und elektrischen Felder analysiert. Die theoretischen Ergebnisse dieser Simulationen werden dann mit experimentellen Daten verglichen, welche durch die Levitation individueller Partikel auf dem Chip erhalten wurden. Schließlich werden Feldkonfigurationen präsentiert, welche eine vollständige dreidimensionale Kontrolle über den Partikel erlauben. Diese Ergebnisse demonstrieren erstmalig die dreidimensionale Aktuation durch Elemente in einer Ebene. Als chip-basierte Version von *magnetic tweezers* stellt dieser Ansatz ein vielfältiges Werkzeug für biophysikalische Untersuchungen dar.

Der letzte Teil der Arbeit befasst sich mit der Verwendung von Mikrodrahtarrays als Mittel zur thermalen Stimulation von Zellen. Im Speziellen werden durch resistives Aufheizen der Mikrodrähte Stimuli hoher thermaler Energie appliziert. Diese Technik wird anschließend a mögliche chip-basierte Methode zur Erzeugung hochaufgelöster Lä-

sionen in biologischen Netzwerken untersucht. Als Beispiel eines funktionalen Zellnetzwerkes werden kardiomyozytenähnliche HL-1-Zellen auf den Chips kultiviert. Die Lokalisierung der Läsion wird mittels Fluoreszenzfärbung untersucht. Die Funktionalität des Netzwerkes vor und nach der Läsion wird mittels Ca^{2+} *imaging* analysiert. In diesem Zusammenhang werden Korrelations- und Frequenzanalysen verwendet um eine Einsicht in die Signalpropagation in dem Netzwerk zu erhalten. Schließlich wird die Separation funktional intakter Subnetzwerke von weniger als 100 Zellen demonstriert.

Zusammenfassend beschreibt die vorliegende Arbeit Mikrodrahtarrays als vielfältige Plattformen in der chip-basierten Applikation chemischer, mechanischer und thermischer Stimuli. Die dreidimensionale Aktuation von Partikeln, die in den ersten beiden Teilen präsentiert wird, ermöglicht die parallele Durchführung zahlreicher biophysikalischer Studien. Die vorgestellte Methode zur thermalen Einbringung von Läsionen in Zellnetzwerke ermöglicht eine höhere Auflösung als bisherige Methoden. Gleichzeitig bietet sie eine simple Fabrikation und eine direkte Implementierbarkeit in aktuelle chip-basierte Zellanalysesysteme.

Abstract

Over the past two decades, miniaturized biophysical tools, referred to as lab-on-a-chip or micro-total-analysis-systems, have become a vivid field of interdisciplinary research. This development is owed to the fact that these tools promise lower sample and time consumption and higher parallelization than classical wet-lab experiments. At the same time, these tools can offer a resolution that is often impossible to achieve with classical probe-based techniques. In this context, the present thesis investigates the use of microwire crossbar arrays to deliver chemical, mechanical, and thermal stimuli to networks of biological cells.

The first part of this work considers magnetic microparticles as transducers of chemical and mechanical stimuli. To this end, a chip-based approach to exert precise control over these particles is examined. Here, microwire crossbar arrays are used as miniaturized electromagnets to generate highly localized magnetic fields. These fields, in turn, are used to exert precise control over the particles at subcellular resolution. In order to ensure successful delivery of the particles, simple but efficient protocols for the transport of particles are investigated. In the application of these protocols, a new approach to deploy and control individual particles on-chip is introduced. This method effectively

cancels the risk of undesired delivery to another than the target cell allowing reliable and controlled stimulation of single cells. In order to demonstrate the excellent control over the particle, an analytical simulation of the system is compared to experimental data. The latter is obtained using an image processing algorithm that allows for particle detection at submicron resolution.

In the second part, the parallel generation of magnetic and dielectrophoretic forces is investigated as a means to avoid particle immobilization due to adhesive particle/surface interactions. Using finite elements simulations, the magnetic and electric fields generated by the arrays are analyzed. The theoretical results from these simulations are then compared to experimental data obtained from individual particles levitated on the chip. Finally, field configurations that allow full three-dimensional control over the particle are presented. These results demonstrate for the first time the precise three-dimensional actuation of a single particle using only in-plane actuators. As an on-chip version of magnetic tweezers, this method poses a versatile tool to a number of biophysical investigations.

The last part of the thesis examines microwire crossbar arrays as a tool for the thermal stimulation of cells cultured on the chip. In particular, stimuli of high thermal energy are applied via resistive heating of the microwires. The technique is then examined as a possible chip-based method to generate highly resolved lesions in biological networks. As an exemplary functional cell network cardiomyocyte-like HL-1 cells are grown on the chips. The localization of the lesion is examined using fluorescent staining methods. The functionality of the network before and after the lesion is analyzed via Ca^{2+} imaging. Here, correlation and frequency analyses are used to give an insight

into the signal propagation in the network. Finally, the dissection of functionally intact subnetworks of less than 100 cells is demonstrated.

Overall, this thesis illustrates the applicability of microwire arrays as versatile platforms in the chip-based application of chemical, mechanical, and thermal stimuli. The three-dimensional actuation of particles presented in the first two parts allows for the parallel conduction of a number of new biophysical studies. The presented method for the thermal introduction of lesions allows for a significantly higher resolution than current methods. At the same time, it offers simple fabrication and straight-forward implementation into current on-chip cell analysis systems.

Contents

CHAPTER 1

INTRODUCTION

Biological systems, such as the organs of the human body, are among the most complex systems known to mankind [1, 2]. The human brain, for instance, can be estimated to have more synapses than there are stars in the milky way[1]. A thorough understanding of these systems is of central interest from a fundamental-research and a medical point of view.

In this context, biophysics is a particularly interesting research discipline. Biophysics refers to the analysis of biological systems by physical means [6][2]. The benefits of this approach can be twofold. On the one hand, biophysical research offers an insight into biological systems that is not available by classical biological means. In the framework of cellular biophysics, the elucidation of the mechanisms

[1]The number of stars in the milky way is approximately 10^{11}–10^{12} [3]. An adult male human brain comprises approximately 8.6×10^{10} neurons that each have approximately 38 000 synapses [4, 5].

[2]These systems can generally range from a molecular to an ecological scale.

underlying membrane currents during the 1950s poses a prominent example [7–11]. On the other hand, biophysical research can yield tools that enable new levels of biological research. Here, the development of the patch clamp technique for single ion channel or single cell intracellular recordings in the 1970s could be given as one of many examples [12, 13].

Over the past two decades, lab-on-a-chip approaches have emerged as a new field in biophysics or physical chemistry [14–17]. This field employs fabrication methods originating in the microelectronic industry (e.g. photolithography) to create miniaturized sensors or systems for different fields of research. In the context of electrical or electrochemical recording from cellular networks, multielectrode or multitransistor arrays are a prominent example of the advantages offered by this field. These platforms offer a grade of parallelization and spatio-temporal resolution virtually impossible to reach with standard methods like the above mentioned probe-based techniques [18–23]. Furthermore, enhanced recording concepts open insights into other communication pathways than that of electrogenic cells [24, 25]. Apart from the extraction of information from biological networks, on-chip technologies may also be used to deliver information into these systems. Chemical information in the form of dyes, proteins, or nucleic acids, for instance, can be delivered using structural elements incorporated in to the chip [26–30]. Mechanical stimulation, for instance, was demonstrated using the substrate or magnetic nanoparticles [31, 32]. Magnetic micro- and nanoparticles are a common transducer used in the delivery, as well as the extraction, of information to biological systems [33–36]. They were, for instance, used to probe mechanical properties of cells [37, 38], to remotely activate ion channels in cells [39], and to localize cytosolic

reactions *in vitro* and *in vivo* [40–42]. In most of the examples given above, the actuation of the magnetic particles is performed using lab-sized electromagnets. In particular, so-called magnetic tweezers are a common tool to exert controlled forces on magnetic entities [43, 44]. However, while offering the possibility to apply large forces, these systems cannot directly be implemented into lab-on-a-chip devices.

In order to use micro- and nanoparticles for chemical and mechanical stimulation, the surface of the particle, as well as that of the substrate, have to be functionalized. In the former case, this is to bind a given cargo to the particle, while in the latter case most cells require protein-coated substrates for adhesion and growth. Depending on the types of functionalization, however, adhesive forces can lead to an immobilization of the particle. In this case, the application of repulsive forces to maintain particle mobility is necessary. A prominent way to generate such forces in on-chip tools is dielectrophoresis (DEP). Dielectrophoresis refers to the motion of polarizable particles in non-uniform electric fields. In terms of biophysics, it was used as early as 1966 to separate live from dead cells [45]. In the framework of lab-on-a-chip technologies, dielectrophoresis has been applied to various tasks [46–48]. As the forces exerted by dielectrophoresis act selectively and are strongly localized to the vicinity of the electrodes, it is an excellent tool for flow-based sorting applications [49–51]. Ahn *et al.*, for instance, have reported of single droplets being reliably sorted out of a 1.6 kHz droplet flow [51]. It was also shown to be applicable to the label-free cell cycle synchronization of mammalian and yeast cells [52, 53]. Apart from its application in microfluidics, dielectrophoresis has also been applied in other chip-based settings. In terms of parallelization, for instance, DEP chips with tens of thousands of individually controllable

electrodes have been presented [54, 55]. These chips, however, require complex complementary metal-oxide-semiconductor (CMOS) fabrication. In contrast, Chiou *et al.* reported applications without the need of complex fabrication [56]. Using photoconductive layers as electrodes implemented in a microscope setup, simultaneous manipulation of 15 000 particle traps was shown.

In addition to chemical and mechanical stimulation, the controlled application of lesions to biological networks is a classical method to elucidate a cell network's function, as well as its regeneration mechanisms. In the study of neuronal networks, for instance, this technique is of great value [57–59]. In order to create highly-resolved lesions, lasers are an established tool [60–62]. In an *in-vitro* setting, the laser is usually coupled into the beam path of a microscope [63, 64]. However, the use of advanced cell-analysis systems including microfluidic cell culture setups and opaque functional substrates (as those mentioned above [22, 23]) can make it difficult or impossible to integrate laser-based stimulation. Recently, several groups have thus directed efforts towards the combination of lesion techniques with the advantages of on-chip technologies [15, 65–69]. These efforts have, for instance, resulted in the successful introduction of microfluidic models of axotomy [70–74]. Although these methods allow for high sample throughput via parallelization, they intrinsically impose certain constraints. On the one hand, the flow-based nature of microfluidic systems, renders intersecting or orthogonal lesion patterns difficult to realize. On the other hand, the generation of local lesions without otherwise constraining the culture's growth is problematic.

The present thesis investigates the use of microwire arrays to deliver chemical, mechanical, and thermal stimuli. In the first part, a chip-

based approach to the precise control of magnetic particles is examined. To this end, microwire crossbar arrays are used as miniaturized electromagnets to generate highly localized magnetic fields. The use of these arrays was pioneered by Lee *et al.*, who demonstrated their application for the actuation of clouds of nanoparticles, as well as particles coupled to yeast cells [75–78]. Advancing their work, simple but efficient protocols for the transport of particles are investigated to ensure successful particle delivery. Furthermore, in order to eliminate the risk of undesired stimulation or delivery, methods to deploy and control single microparticles are examined. The intended use of these methods is the chemical or mechanical stimulation of individual cells via guided delivery or direct application of mechanical stimuli. To ensure particle mobility in this context, the second part of the present thesis examines the parallel generation of magnetic and dielectrophoretic forces. Using accompanying simulations, the magnetic and electric fields generated by the arrays are investigated. The results are then applied to achieve full three-dimensional control over an individual particle trapped on the chip. The last part of the thesis examines microwire crossbar arrays as an on-chip tool for the thermal introduction of lesions. To this end, resistive heating of the microwires is used to apply localized stimuli of high thermal energy. The results are analyzed in terms of localization of the lesion, functionality in the network, and the possibility to dissect small subnetworks. In this way, the use of microwire crossbar arrays as a flexible tool in the chip-based application of chemical, mechanical, and thermal stimuli is demonstrated. Using this tool, biophysical experiments with a higher resolution and a greater ease of parallelization than possible before can be performed.

CHAPTER 2

FUNDAMENTALS & THEORY

2.1 MAGNETOPHORESIS

The term magnetophoresis is derived from the words 'magnet' (from Greek $\mu\alpha\gamma\nu\eta\tau\iota\varsigma\ \lambda\iota\theta\mathrm{o}\varsigma$, "stone from magnesia") and 'phoresis' (from Greek $\phi\mathrm{o}\rho\varepsilon\sigma\iota\varsigma$, "the act of bearing") and describes the motion of a magnetic material due to a surrounding magnetic field[79, 80]. The concept of magnetic fields has been particularly employed in a nautical setting in the form of the compass for almost a millenium[80]. However a detailed theoretical understanding of magnetic fields and the forces generated by them was only developed during the 19^{th} century. In particular, the findings of Ørstedt, Ampère, Biot and Savart, Faraday, and Maxwell contributed to the understanding of magnetic fields[81].

A significant part of the present work is concerned with the collection and actuation of magnetic microparticles in non-uniform magnetic fields. The following sections are thus intended to give the reader an overview over fundamental concepts regarding the theory of magnetic fields, basic magnetic properties of materials, and forces exerted on particles that are subjected to magnetic fields.

2.1.1 MAGNETIC FIELDS

In the experiments conducted in this thesis, electric currents are used to induce magnetic fields. The following section will thus give an overview about how magnetic fields can be calculated from current densities[1]. To this end, the current and current density will be defined. Subsequently, Biot-Savart's law will be introduced as a mean to calculate magnetic fields from arbitrary current densities.

[1] More thorough descriptions of the general theory of magnetic fields can be found in standard text books about electromagnetism [82–84].

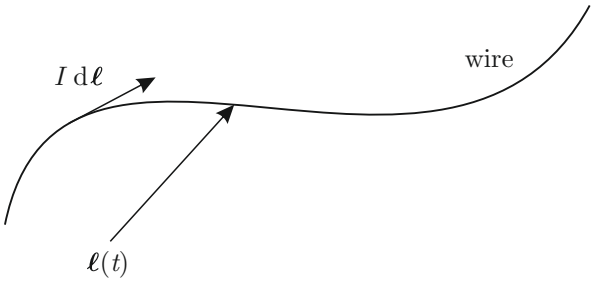

FIGURE 2.1: A thin wire can be described by a parametrized curve, $\boldsymbol{\ell}(t)$. Each segment of the wire, $\mathrm{d}\boldsymbol{\ell}$, gives a contribution of $I\mathrm{d}\boldsymbol{\ell}$ to the total current in the system.

CURRENT AND CURRENT DENSITY An electric field applied to a conductor will cause the movement of electric charges inside of the conductor. The amount of charge passing the cross-section of the conductor per time is defined as the current, I:

$$I = \frac{\mathrm{d}q}{\mathrm{d}t}, \tag{2.1}$$

where $\mathrm{d}q$ is an amount of charge and $\mathrm{d}t$ a corresponding time interval. The *current density*, j, is defined as a given current per cross-sectional area, A.

$$j = \frac{I}{A} \tag{2.2}$$

In order to define a vectorial current density, $\boldsymbol{j}$, a thin wire is considered. This wire can mathematically be described as a parametrized curve $\boldsymbol{\ell}(t)$, with t being the parameter (see Fig. 2.1). Assuming the tangential vector $\frac{\mathrm{d}\boldsymbol{\ell}}{\mathrm{d}\ell}$ is oriented in the direction of the current, the vectorial current density can be defined as

$$\boldsymbol{j} = \frac{I}{A}\frac{\mathrm{d}\boldsymbol{\ell}}{\mathrm{d}\ell}. \tag{2.3}$$

The current density in a given system of conductors can thus be described as a vector field.

BIOT-SAVART'S LAW When bringing two current-carrying wires in proximity, a force between the wires can be noted. The force on a small segment of one of the wires, $\mathrm{d}\boldsymbol{F}$, is proportional to the current $\mathrm{d}\boldsymbol{F} \propto I$, proportional to the length of the segment $\mathrm{d}\boldsymbol{F} \propto \mathrm{d}\boldsymbol{\ell}$, and orthogonal to the orientation of the segment $\mathrm{d}\boldsymbol{F} \perp \mathrm{d}\boldsymbol{\ell}$. In summary, the relation for this force can thus be written as

$$\mathrm{d}\boldsymbol{F}(\boldsymbol{r}) = I\,\mathrm{d}\boldsymbol{\ell} \times \boldsymbol{B}(\boldsymbol{r}). \tag{2.4}$$

The vector field $\boldsymbol{B}(\boldsymbol{r})$ defined by Eq. 2.4 is referred to as magnetic flux density or simply magnetic field[2]. The force in Eq. 2.4 is commonly referred to as Lorentz force.

After using Eq. 2.4 to define the magnetic field, the field induced by a small wire segment $\mathrm{d}\boldsymbol{\ell}$ located at $\boldsymbol{r}'$ and carrying a constant current I can be determined. Experimentally, the following properties of this field can be determined:

$$\begin{aligned} &\mathrm{d}B \propto I\,\mathrm{d}\ell, \quad \mathrm{d}\boldsymbol{B} \perp \mathrm{d}\boldsymbol{\ell}, \quad \mathrm{d}\boldsymbol{B} \perp (\boldsymbol{r} - \boldsymbol{r}'), \\ &\mathrm{d}B \propto \frac{1}{|\boldsymbol{r} - \boldsymbol{r}'|}, \quad \mathrm{d}B \propto \sin\left(\angle(\mathrm{d}\boldsymbol{\ell}, \boldsymbol{r} - \boldsymbol{r}')\right). \end{aligned} \tag{2.5}$$

[2]The term "magnetic field" can is commonly used to refer to the magnetic flux density $\boldsymbol{B}$, as well as the magnetic field strength $\boldsymbol{H}$. In the following, however, the terms "magnetic field" and "magnetic flux density" will be used for $\boldsymbol{B}$ only. This is to highlight the analogy between $\boldsymbol{B}$ and the electric field $\boldsymbol{E}$ in the sections concerned with both, magnetophoresis and dielectrophoresis.

Combining these properties yields

$$\mathrm{d}\boldsymbol{B}(\boldsymbol{r}) = \frac{\mu_0}{4\pi}\, I\, \mathrm{d}\boldsymbol{\ell} \times \frac{\boldsymbol{r} - \boldsymbol{r}'}{|\boldsymbol{r} - \boldsymbol{r}'|^3} \tag{2.6}$$

as the field contribution $\mathrm{d}\boldsymbol{B}(\boldsymbol{r})$ of a wire segment $\mathrm{d}\boldsymbol{\ell}$ at $\boldsymbol{r}'$. The constant μ_0 in Eq. 2.6 is referred to as magnetic constant or vacuum permeability. Its value is determined experimentally and amounts to $\mu_0 = 4\pi \times 10^{-7}\,\mathrm{V\,s\,A^{-1}\,m^{-1}}$.

Inserting $I\,\mathrm{d}\boldsymbol{\ell} = \boldsymbol{j}(\boldsymbol{r}')\,\mathrm{d}^3r'$ in Eq. 2.6 and summing all contributions gives

$$\boldsymbol{B}(\boldsymbol{r}) = \frac{\mu_0}{4\pi} \int \mathrm{d}^3r'\, \boldsymbol{j}(\boldsymbol{r}') \times \frac{\boldsymbol{r} - \boldsymbol{r}'}{|\boldsymbol{r} - \boldsymbol{r}'|^3}, \tag{2.7}$$

which is known as Biot-Savart's law [84]. Eq. 2.7 allows to calculate the magnetic field $\boldsymbol{B}(\boldsymbol{r})$ for an arbitrary current density $\boldsymbol{j}(\boldsymbol{r})$.

2.1.2 MAGNETIC FIELDS INDUCED BY MICROWIRE CROSSBAR ARRAYS

The previous section introduced fundamental equations necessary to calculate magnetic fields. In the following, these equations will be used to calculate the magnetic field generated by a wire with rectangular cross-section, such as those used in the present thesis. Subsequently, the fields derived in this way will be added to yield the localized magnetic fields that are used to trap and actuate particles in the experiments presented in later chapters.

MAGNETIC FIELD OF A WIRE WITH RECTANGULAR CROSS SECTION

Figure 2.2 shows a schematic of the geometry used for the following calculation. The wire is assumed to have a width of W and a height

of H. The microwires used in the present thesis, exhibit this geometry along a center region of approximately 2 mm. The actual microwire array, however, only has a total width of approximately 250 µm and is located in the center of the wire. For the calculation of the magnetic fields in this center region, the microwires can thus be considered of infinite length.

Assuming the microwire carries a homogeneous current I in the y-direction, the current density in the system is given by

$$\boldsymbol{j}(\boldsymbol{r}) = \begin{cases} \frac{I}{WH}\,\boldsymbol{u}_{\mathrm{y}} & \text{for } -\frac{W}{2} < x < \frac{W}{2} \text{ and} -\frac{H}{2} < z < \frac{H}{2} \\ 0 & \text{everywhere else} \end{cases} \tag{2.8}$$

where $\boldsymbol{u}_{\mathrm{y}}$ refers to the unit vector in y-direction. Using Eq. 2.7, the magnetic field can thus be calculated as:

$$\begin{aligned} \boldsymbol{B}(\boldsymbol{r}) &= \frac{\mu_0 I}{4\pi WH} \int_{-\frac{W}{2}}^{\frac{W}{2}} \mathrm{d}x' \int_{-\infty}^{\infty} \mathrm{d}y' \int_{-\frac{H}{2}}^{\frac{H}{2}} \mathrm{d}z'\, \boldsymbol{u}_y \times \frac{\boldsymbol{r} - \boldsymbol{r'}}{|\boldsymbol{r} - \boldsymbol{r'}|^3} \\ &= \frac{\mu_0 I}{4\pi WH} \int_{-\frac{W}{2}}^{\frac{W}{2}} \mathrm{d}x' \int_{-\infty}^{\infty} \mathrm{d}y' \int_{-\frac{H}{2}}^{\frac{H}{2}} \mathrm{d}z' \\ &\qquad \frac{(z - z')\,\boldsymbol{u}_x - (x' - x)\,\boldsymbol{u}_z}{\left((x - x')^2 + (y - y')^2 + (z - z')^2\right)^{3/2}}. \end{aligned} \tag{2.9}$$

As can be seen, the magnetic field of the wire does not have a component in y-direction, which is in accordance with the symmetry of the system. In order to solve the integration over $\mathrm{d}^3 r$, the x- and z-components of the magnetic field can be treated individually.

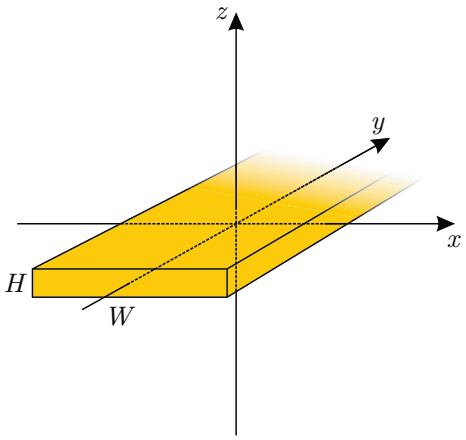

FIGURE 2.2: Schematic of an infinitely long rectangular wire of width W and height H located in the coordinate origin.

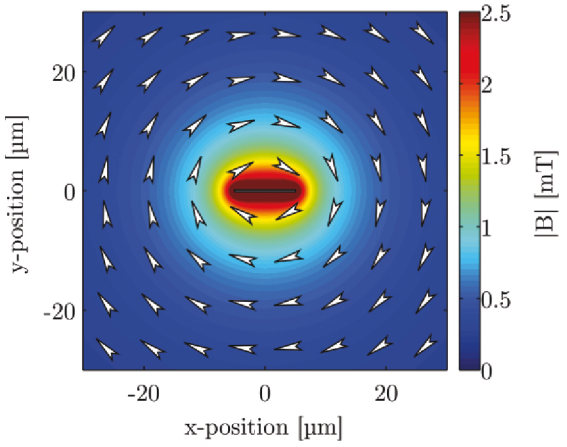

FIGURE 2.3: Magnetic field induced by an infinitely long wire of width $W = 10\,\mu\text{m}$ and height $H = 0.3\,\mu\text{m}$ carrying a current of $I = 50\,\text{mA}$. The color plot shows the magnitude of the field, while the arrows indicate the direction of the field. The wire is indicated by the white rectangle in the center.

Additionally, the integral with respect to $\mathrm{d}y'$ can separated as follows

$$B_x(\boldsymbol{r}) = \frac{\mu_0 I}{4\pi W H} \int_{-\frac{W}{2}}^{\frac{W}{2}} \mathrm{d}x' \int_{-\frac{H}{2}}^{\frac{H}{2}} \mathrm{d}z' \, (z - z') \int_{-\infty}^{\infty} \mathrm{d}y' \, \frac{1}{\left((x - x')^2 + (y - y')^2 + (z - z')^2\right)^{3/2}}. \quad (2.10)$$

Substituting $\xi = y - y'$, this integral can then be solved using the following relation [85].

$$\int \mathrm{d}\xi \, (\xi^2 + C)^{-3/2} = \left(\frac{\xi}{C\sqrt{C + \xi^2}} \right) \Bigg|_{-\infty}^{\infty} \approx {}^2/_C$$

Solving the remaining two integrals gives the following expressions for the magnetic field components in x- and z-direction

$$\begin{aligned} B_x(\boldsymbol{r}) &= -\frac{\mu_0 I}{2\pi W H} \int_{-\frac{W}{2}}^{\frac{W}{2}} \mathrm{d}x' \int_{-\frac{H}{2}}^{\frac{H}{2}} \mathrm{d}z' \, \frac{(z - z')}{(x - x')^2 + (z - z')^2} \\ &= \frac{\mu_0 I}{2\pi W H} \left[\frac{W - 2x}{4} \ln \left(\frac{(H + 2z)^2 + (W - 2x)^2}{(H - 2z)^2 + (W - 2x)^2} \right) \right. \\ &\quad \left. + \frac{W + 2x}{4} \left(\frac{(H + 2z)^2 + (W + 2x)^2}{(H - 2z)^2 + (W + 2x)^2} \right) \right] \\ &\quad + \frac{H - 2z}{2} \left(\arctan\left(\frac{W + 2x}{2z - H} \right) + \arctan\left(\frac{W - 2x}{2z - H} \right) \right) \\ &\quad + \frac{H + 2z}{2} \left(\arctan\left(\frac{W + 2x}{2z + H} \right) + \arctan\left(\frac{W - 2x}{2z + H} \right) \right) \end{aligned} \quad (2.11a)$$

$$
\begin{aligned}
B_z(\boldsymbol{r}) &= \frac{\mu_0 I}{2\pi W H} \int_{-\frac{W}{2}}^{\frac{W}{2}} \mathrm{d}x' \int_{-\frac{H}{2}}^{\frac{H}{2}} \mathrm{d}z' \, \frac{(x-x')}{(x-x')^2+(z-z')^2} \\
&= \frac{\mu_0 I}{2\pi W H} \left[\frac{H-2z}{4} \ln\left(\frac{(H-2z)^2+(W-2x)^2}{(H-2z)^2+(W+2x)^2} \right) \right. \\
&\quad \left. + \frac{H+2z}{4} \left(\frac{(H+2z)^2+(W-2x)^2}{(H+2z)^2+(W+2x)^2} \right) \right] \\
&\quad + \frac{2x-W}{2} \left(\arctan\left(\frac{H-2z}{2x-W} \right) + \arctan\left(\frac{H+2z}{W-2x} \right) \right) \\
&\quad + \frac{W+2x}{2} \left(\arctan\left(\frac{-H-2z}{W+2x} \right) + \arctan\left(\frac{H-2z}{W+2x} \right) \right)
\end{aligned}
\tag{2.11b}
$$

Figure 2.3 shows the magnetic field of a rectangular wire calculated using Eq. 2.11. As can be seen, the magnetic field strongly decreases with distance from the wire. The field lines (indicated by the white arrows) form closed loops around the wire, which is due to the solenoidal property of magnetic fields [84]. In the vicinity of the wire, they are deformed to an elliptical shape. With increasing distance from the wire, however, their shape is more circular, as would be the case for a wire of infinitesimal cross-section [84].

MAGNETIC FIELDS OF MULTIPLE RECTANGULAR WIRES The experiments presented in this thesis make use of an array of two orthogonal layers of microwires each identical to the one described in the previous section. In order to generate localized magnetic fields, several of these wires are used simultaneously. The following paragraphs will thus illustrate the magnetic fields induced by exemplary arrangements of multiple wires.

The most basic combination of more than a single wire is that of two parallel wires. In this case, the currents in both wires can be of parallel or antiparallel orientation. Referring to Figure 2.3, however, it can

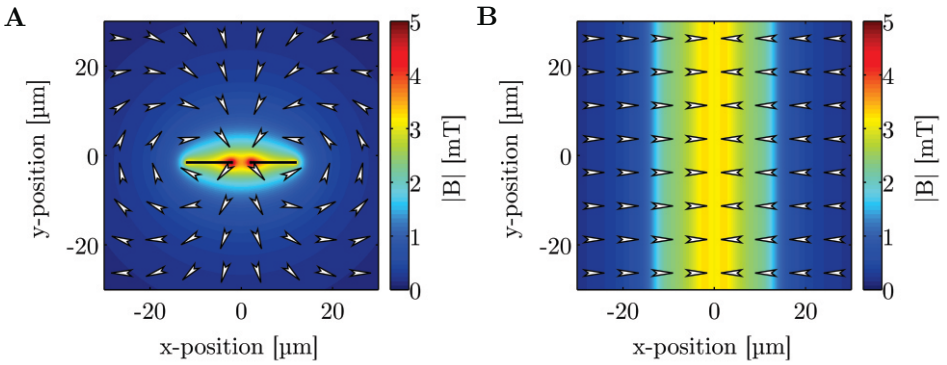

FIGURE 2.4: Magnetic field induced by two parallel infinitely long wires with rectangular cross-section ($W = 10\,\mu m$ and $H = 0.3\,\mu m$). The wires are placed at an interwire spacing of $4\,\mu m$ and at $z = -1.55\,\mu m$. The wires carry a current of $50\,mA$ in the positive an negative y-direction (left and right wire, respectively). The color plot shows the magnitude of the field, while the arrows indicate the direction of the field. **A:** Magnetic field in the x-z-plane. The field is strongest in between the wires. In particular the inner edges of the wires exhibit high fields strengths. **B:** At $z = 0$, this edge effect is less pronounced. The high-field region, however, remains localized to the region in between the wires.

be seen that only an antiparallel orientation will result in a stronger localization of the magnetic field. This is due to the fact that in this case the magnetic fields of both wires add up in the region between the wires. In the remaining regions, both fields point in opposing directions and thus weaken each other.

Figure 2.4 shows the corresponding magnetic fields calculated using Eq. 2.11. In analogy to the microwire arrays used in the experiments, the wires are placed at an interwire spacing of $4\,\mu m$ and at $z = -1.55\,\mu m$. In this way, the surface of the microwire array chip is located at $z = 0\,\mu m$ (for fabrication details see Section 3.2.1). The left

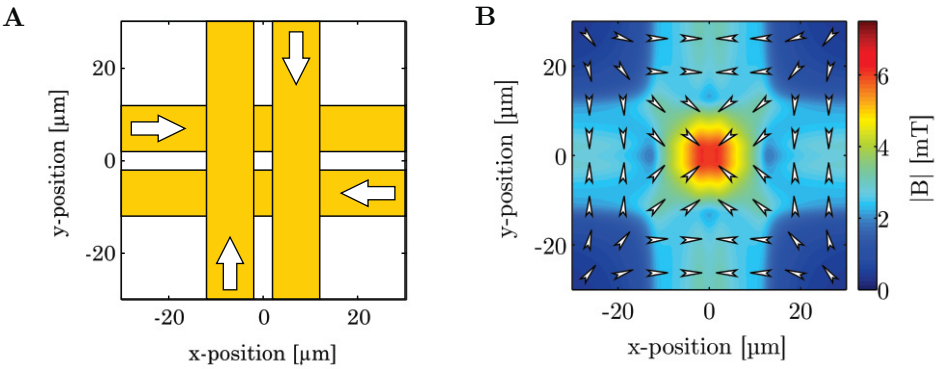

FIGURE 2.5: Magnetic field induced by two orthogonal pairs of wires with rectangular cross-section ($W = 10\,\mu m$ and $H = 0.3\,\mu m$). **A:** Schematic illustration of the current directions in the wires. **B:** Magnetic field induced by two horizontal and two vertical wires (located at $z = -1.9\,\mu m$ and $z = -1.55\,\mu m$, respectively) supplied with currents of $I = 50\,mA$ as illustrated in **A**. The magnetic field exhibits a clear peak in the center of the four wires.

wire carries a current of 50 mA in the positive y-direction and the right wire carries a current of 50 mA in the negative y-direction.

As described above, the magnetic field in the x-z-plane is strongest in between the wires (see Figure 2.4A, wires indicated by white rectangles). In particular the edges of the wires exhibit high field strengths. At the chip's surface ($z = 0$, Figure 2.4B), the effect of the edges is less pronounced. The region of highest field strength, however, is still located in between the wires.

In order to further localize the magnetic field, the second layer of wires can be used. In analogy to the argument given above, the currents in two parallel wires in this layer have to be of antiparallel orientation. Similarly, the relative orientation between both layers has to be chosen so that the fields of all wires overlap in the center region.

Figure 2.5A shows a schematic of four wires carrying currents oriented in this way. With respect to the center of the wires, the currents are arranged in a way that is similar to a current-driven loop (see, for instance, [83, 84]). Figure 2.5B shows the magnetic field calculated for a set of wires arranged in this way. Similar to Figure 2.4, the second set of wires was placed at $z = -1.9\,\mu\text{m}$ in analogy to the chips used in the experiments (see Section 3.2.1 for fabrication details).

As illustrated by Figure 2.5B, the magnetic field induced by a set of wires arranged in this way exhibits a clear peak in the center of the wires. This peak extends approximately $10\,\mu\text{m}$ in x- and y-direction. It has to be noted, however, that this localization only depends on the relative orientation of the currents. Inverting all currents inverts the direction of the magnetic field, but maintains the distribution of the field strength shown by the color plot in Figure 2.5B.

2.1.3 MATTER IN MAGNETIC FIELDS

The previous section introduced the calculation of the magnetic field induced by a current density using Biot-Savart's law. In the experiments presented in Chapters 3 and 4, these fields will be used to exert forces on magnetizable particles. The following section will thus describe the interaction of magnetic fields with matter. To this end, the magnetic field strength, $\boldsymbol{H}$, as well as the magnetization $\boldsymbol{M}$ will be introduced. Subsequently, different classes of magnetism in matter will be described. In this context, mainly diamagnets and superparamagnets are of relevance to the experiments presented herein. For the sake of completion, however, paramagnets and ferromagnets will also be presented.

When a material is placed in a magnetic field, the magnetic field in the material differs from that in vacuum. This difference can be approximated as a linear factor according to

$$\boldsymbol{B} = \mu_\mathrm{r}\, \boldsymbol{B}_0 = \mu_\mathrm{r}\, \mu_0\, \boldsymbol{H}_0, \tag{2.12}$$

where μ_r is a material constant referred to as relative permeability, $\boldsymbol{B}_0$ and $\boldsymbol{H}_0$ refer to the magnetic flux density and the magnetic field strength in the absence of the material, respectively [83].

This change in the field can originate in two ways. In materials comprised of atoms without permanent magnetic dipole moments, the external field induces dipoles. In materials that possess permanent dipole moments, the magnetic field orients these dipoles. In both cases, the result is a net dipole moment per volume. This quantity is referred to as magnetization

$$\boldsymbol{M} = \frac{\boldsymbol{m}_\mathrm{mag}}{V}. \tag{2.13}$$

The magnetic field inside of the material can thus be expressed as the sum of the external field strength and the magnetization of the material

$$\boldsymbol{B} = \mu_0\, (\boldsymbol{H}_0 + \boldsymbol{M})\,. \tag{2.14}$$

At moderate field strengths, the relation between the field strength and the magnetization can be assumed as linear. This linear relation can be expressed using a material constant χ_mag, which is referred to as magnetic susceptibility. Inserting $\boldsymbol{M} = \chi_\mathrm{mag}\, \boldsymbol{H}_0$ in Eq. 2.14 gives

$$\boldsymbol{B} = \mu_0\, (1 + \chi_\mathrm{mag})\, \boldsymbol{H}_0. \tag{2.15}$$

Comparing Eqs. 2.12 and 2.15 shows the following relation between a material's relative permeability and its magnetic susceptibility

$$\mu_{\mathrm{r}} = (1 + \chi_{\mathrm{mag}})\,. \tag{2.16}$$

Based on their response to an external magnetic field (i.e. the sign and magnitude of χ_{mag}) and its cause on an atomic scale, all materials can be sorted in one of the following categories: diamagnets, paramagnets, ferromagnets, antiferromagnets, and ferrimagnets. As mentioned in the beginning of this section, the following paragraphs will give the reader an overview about the classes of materials relevant to the experiments presented herein [83].

DIAMAGNETS In a diamagnet, the magnetic moments of the protons, neutrons, and electrons add up so that the overall magnetic moment of the atom is 0. When placed in a magnetic field, however, an induced dipole moment will result in the atoms. These dipole moments will oppose the external field, which results in a lower field inside of the material. Consequently, $\chi_{\mathrm{mag}} < 0$ for these materials (i.e. $\mu_{\mathrm{r}} < 1$). The magnetic susceptibilities of common diamagnets are listed in Table 2.1[86]. As can be seen, the magnetic susceptibilities of diamagnets take rather small values. The relative permeability thus remains ≈ 1 and these materials only have negligible effects on magnetic fields.

It has to be noted that all materials exhibit a diamagnetic response. However, in materials that additionally show, for instance, paramagnetic behaviour, the diamagnetic effects are negligable. Concerning the experiments described herein, all materials except for the magnetic particles were diamagnets. Their influence on the magnetic fields is thus neglected.

TABLE 2.1: Volume magnetic susceptibilities χ_{mag} for common materials (adapted from [83, 86–92]).

Material	$\boldsymbol{\chi_{\mathrm{mag}}}$
Diamagnets	
Pyrolytic carbon	-40.9×10^{-5}
Silver	-2.6×10^{-5}
Diamond	-2.1×10^{-5}
Graphite	-1.6×10^{-5}
Water	-0.9×10^{-5}
Paramagnets	
Tungsten	1.5
Aluminium	0.06
Lithium	0.007
Magnesium	0.02
Sodium	0.007
Ferromagnets	
Iron	500–10 000
Cobalt	80–200
Permalloy (78% Ni, 19% Fe, 3% Mo)	10^4–10^5

PARAMAGNETS In contrast to diamagnets, the atoms in paramagnets exhibit permanent magnetic dipole moments. The orientation of these dipole moments is strongly affected by thermal fluctuations and is thus randomly distributed. Consequently, the overall resulting magnetic moment amounts to 0. When placed in an external magnetic field, however, an orientation along the field is energetically favorable and an overall magnetic moment parallel to the direction of the field results. As the thermal energy has to be balanced against the energy gained by orienting a single dipole, the overall orientation (and thus the resulting moment) depends on the temperature, as well as the strength of the external field. Since the resulting magnetic moment is oriented along the field, the field strength in the material increases, which is expressed by magnetic suceptibilities > 0 (i.e. $\mu_\mathrm{r} > 1$). Table 2.1 lists the magnetic susceptibilities of exemplary paramagnetic materials [87–92].

FERROMAGNETS Unlike the aforementioned materials, ferromagnetic materials exhibit a spontaneous magnetization without the presence of an external field. Similar to paramagnets, this magnetization is the result of individual atomic molecular moments. Due to a strong exchange interaction between these moments, however, their orientation is less subject to thermal fluctuations [93]. This leads to the mutual alignment of neighboring moments. In a bulk material, this alignment is restricted to microscopic regions that are referred to as magnetic domains or Weiss domains. Under normal circumstances, these domains are randomly distributed and the overall magnetization is zero. When subjected to an external field, an orientation along the field is energetically favored and the corresponding domains will grow depending on the field strength. Due to the weak thermal influence

on the magnetic moments, the resulting magnetization is maintained even if the field is removed. Because of this permanent magnetization, ferromagnets are among the materials commonly termed "permanent magnets". Their magnetic susceptibility shows very high positive values that depend on their specific history. Table 2.1 lists some values for common ferromagnets [83].

SUPERPARAMAGNETS Superparamagnetism is a special form of ferromagnetism. It can be observed when considering a population of small crystals of ferromagnetic materials. If these crystals are small enough to comprise only a single magnetic domain, all of the atomic dipole moments will be aligned. The total magnetic moment of each crystal is then equal to the sum of the individual moments. Without the presence of a magnetic field, however, the individual crystals will be of random orientation [94]. The total magnetic moment of the population is thus zero. When subjected to a magnetic field, the magnetic moments of the crystals will align according to the external field.

The above given description is analogous to that of an atomic paramagnet. Compared with atomic paramagnetism, however, the magnetic moment of each crystal corresponds to the sum of approximately 10^5 atomic dipole moments [95]. Consequently, the magnetic susceptibility of such materials is approximately 10^5 times larger than for conventional paramagnets. Hence, they are referred to as "superparamagnets" [94, 95].

Superparamagnets are of particular interest in biophysical research [33, 35]. The main advantages of these materials are twofold. Superparamagnets only exhibit a magnetic moment in the presence of a magnetic field. As a result, superparamagnetic particles do not exhibit

a strong particle/particle interaction that could lead to agglomeration. At the same time, however, their magnetization in a magnetic field is significantly stronger than that of paramagnets. The fact that they exhibit a strong magnetic behavior only when it is needed, renders superparamagnetic materials excellent for on-chip applications. As such, the experiments presented in this thesis were conducted with superparamagnetic microparticles.

2.1.4 FORCE ON AN INDUCED MAGNETIC DIPOLE

The previous sections introduced expressions for the magnetic field generated by microwires as those used in the present thesis. Additionally, the behavior of the materials used in this thesis was discussed. The general aim of the experiments presented herein is the use of microwire arrays to exert defined forces on superparamagnetic particles. The following section is thus intended to introduce the force a magnetic field exerts on a superparamagnetic bead.

In general, the force $\boldsymbol{F}_{\mathrm{mag}}$ on a magnetic dipole moment $\boldsymbol{m}_{\mathrm{mag}}$ subjected to an external magnetic field $\boldsymbol{B}$ can be expressed as follows [84, 96].

$$\boldsymbol{F}_{\mathrm{mag}} = \nabla \cdot (\boldsymbol{m}_{\mathrm{mag}} \cdot \boldsymbol{B}) \tag{2.17}$$

Using Eq. 2.13, the magnetic moment of the particle can be expressed as a product of its magnetization $\boldsymbol{M}$ and its volume V.

$$\boldsymbol{F}_{\mathrm{mag}} = V \nabla \cdot (\boldsymbol{M} \cdot \boldsymbol{B}) \,, \tag{2.18}$$

The magnetization, in turn, can be related to the magnetic field via $\boldsymbol{M} = \frac{\Delta\chi_{\mathrm{mag}}}{\mu_{\mathrm{m}}\,\mu_0}\,\boldsymbol{B}(\boldsymbol{r})$, where $\Delta\chi_{\mathrm{mag}}$ represents the difference in magnetic

susceptibility of the particle and the surrounding medium and μ_m refers to the relative permeability of the medium. In the experiments presented in this thesis, the particle was actuated in water. As given in Table 2.1, the magnetic susceptibility of water amounts to -0.9×10^{-5}. It can thus be approximated that $\Delta\chi_\mathrm{mag} \approx \chi_\mathrm{particle}$ and $\mu_\mathrm{m} \approx 1$. Using this appoximation, Eq. 2.18 becomes

$$\boldsymbol{F}_\mathrm{mag} = \frac{V\,\chi_\mathrm{particle}}{\mu_0}\,\nabla \cdot \boldsymbol{B}^2\,, \tag{2.19}$$

which defines the force on a magnetized particle in a magnetic field. The motion of a particle due to this force is referred to as magnetophoresis.

Eq. 2.19 shows that the force on the particle is zero in the case of a uniform magnetic field (i.e. $\nabla \cdot \boldsymbol{B}^2 = 0$). In non-uniform magnetic fields, however, an attractive force towards regions of high field strength results. As this force depends on the square of the magnetic field $\boldsymbol{B}^2$, it is independent of the direction of the field. Referring to Figures 2.4-2.5, this indicates that, as long as the *relative* orientation of the currents is maintained, the particles will be attracted to the same positions.

It has to be noted that Eq. 2.17 is often given in the form $\boldsymbol{F}_\mathrm{mag} = \boldsymbol{m}_\mathrm{mag} \cdot (\nabla \cdot \boldsymbol{B})$. However, this is only correct if the magnetic moment of the particle does not depend on its position in space (i.e. $\nabla \cdot \boldsymbol{m}_\mathrm{mag} = 0$). For low field strengths, this condition is not fulfilled.

2.2 DIELECTROPHORESIS

Similar to the above described magnetophoresis, the word *dielectrophoresis* describes the motion of particles due to their dielectric properties. As with the phenomenological applications of magnetism

in nautic navigation, several dielectrophoretic effects have been known for more than 2000 years [48]. In particular, the fact that vigorously rubbed amber attracts feathers, straws, and other light object has been known since the ancient Greeks. A proper theoretical implementation into the modern physical understanding of electromagnetic effects, however, was established during the 1950s by H.A. Pohl [97]. Pohl also termed the effect as "dielectrophoresis" and used it for biophysical experiments as early as 1966 [45].

In the present thesis, dielectrophoresis is used to exert repellent forces on dielectric particles. In order to describe this effect, the following sections will introduce basic theoretical concepts concerning electrical fields, the interaction of matter with these fields, and finally the origin of dielectrophoretic forces[3].

2.2.1 ELECTRIC FIELDS

Similar to the definition of the magnetic field in 2.1.1, the electrical field can be defined by a force. To this end, one can experimentally determine the force N charges $q_1, \ldots, q_\mathrm{N}$ located at $\boldsymbol{r}_1, \ldots, \boldsymbol{r}_\mathrm{N}$ exert on a probe charge q located at $\boldsymbol{r}$. This force is found to be

$$\boldsymbol{F}(\boldsymbol{r}) = \frac{1}{4\pi\varepsilon_0} \sum_{i=1}^{N} q\, q_\mathrm{i} \frac{\boldsymbol{r} - \boldsymbol{r}_\mathrm{i}}{|\boldsymbol{r} - \boldsymbol{r}_\mathrm{i}|^3} = q\, \boldsymbol{E}(\boldsymbol{r}). \tag{2.20}$$

Eq. 2.20 is refered to as Coulomb's law and defines the electrical field $\boldsymbol{E}(\boldsymbol{r})$. $\varepsilon_0 \approx 8.854 \times 10^{-12}\,\mathrm{s^4\,A^2\,m^{-3}\,kg^{-1}}$ is an experimentally determined constant referred to as electric constant or vacuum permittivity.

[3] More thorough descriptions of the general theory of electric fields can be found in standard text books about electromagnetism [82–84].

The definition given in Eq. 2.20 only concerns the case of localized point charges. In most practical cases, however, a continuous charge density $\varrho(\boldsymbol{r})$ is more appropriate. Using this generalization, a more general definition of the electric field can be given [84].

$$\boldsymbol{E}(\boldsymbol{r}) = \frac{1}{4\pi\varepsilon_0} \int \mathrm{d}^3 r' \, \varrho(\boldsymbol{r}') \, \frac{\boldsymbol{r} - \boldsymbol{r}'}{|\boldsymbol{r} - \boldsymbol{r}'|^3} \, . \tag{2.21}$$

Similar to Biot-Savart's law for magnetic fields (see Eq. 2.7), Eq. 2.21 can be used to calculate the electric field generated by an arbitrary charge density.

As is the case for many practical problems, the charge density in the experiments described in Chapters 3 and 4 is not known. Instead, a defined electric potential Φ, is applied to a set of conductors. In this case, the calculation of the electric field generated by the conductors involves the solution of the differential equation $\Delta\Phi = 0$ [84, 96]. An analytical solution of this equation, however, is only possible for highly symmetric boundary conditions. As such, numerical methods such as finite differences or finite elements have to be applied.

2.2.2 MATTER IN ELECTRIC FIELDS

The previous sections introduced the electrostatic field equations and presented the electric fields produced by exemplary charge densities. Similar to the description of magnetic fields given above, the following section will discuss the interaction of matter and electric fields. With regard to their behavior in electric fields, however, materials can be classified in two distinct classes. These are conductors (i.e. metals)

and dielectrics[4]. These two types of materials will thus be treated in separate.

CONDUCTING BOUNDARIES In the traditional sense, a conductor is defined by the fact that the charge inside of the material can move freely. As the conductors used in this thesis are metals, the following considerations will be restricted to this type of material. The charge carriers in metals are electrons. As discussed in the previous section, an electric field will result in a force on the individual electrons. Since they are allowed to move freely, however, the electrons will follow this force. This movement will continue towards an equilibrium state, where the charge density is such that it cancels the electrical field. Hence, in the electrostatic case, there is no electric field inside of a metal:

$$\boldsymbol{E} = -\nabla\Phi = 0 \qquad \text{in metal} \tag{2.22}$$

and, as a direct consequence,

$$\Phi = const \qquad \text{in metal.} \tag{2.23}$$

In order to evaluate the electric field in the presence of a metal, the exact conditions at the boundary between the metal and the rest of the volume have to be evaluated. To this end, a similar argument to the one given above can be used. Directly at the boundary, the tangential component of the electric field has to be zero. This is due to the fact that any field contribution in this direction would result in a relocation of charge. As described above, the equilibrium case is

[4]The equivalent of a conductor in the case of a magnetic field would be a superconductor. Due to the lack of relevance for this thesis, however, this type of material is not treated in Section 2.1.3.

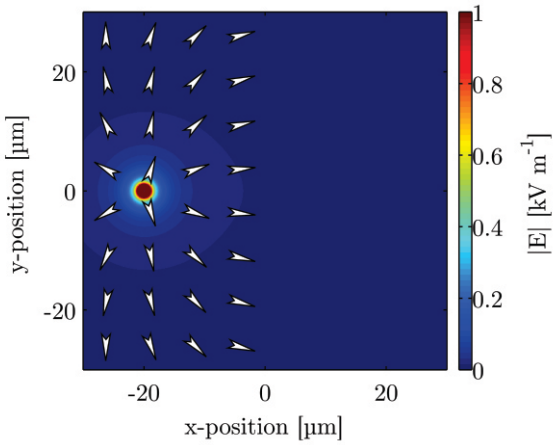

FIGURE 2.6: Field distribution of a point charge $q = 1.602 \times 10^{-19}\,\mathrm{C}$ located at $x = -d = -20\,\mu\mathrm{m}$. The field in the metallic domain ($x > 0$) is zero. Outside of this domain, the field lines originate from the charge and are deformed to meet the boundary at a right angle.

reached when the tangential component of the total electric field is zero. Consequently, electric field lines always form a right angle with a conducting surface.

In order to illustrate this boundary condition, Figure 2.6 shows a basic example. The electric field in this figure is that of a point charge $q = 1.6 \times 10^{-19}\,\mathrm{C}$ located at $x = -d = -20\,\mu\mathrm{m}$ on the x-axis. The positive part of the x-axis for $-\infty \leq y \leq \infty$ and $-\infty \leq z \leq \infty$ is assumed to be metallic and at a potential of zero. As the positive part of the x-axis is assumed to be metallic, the electric field in this region is zero. The electric field in the negative part of the x-axis can be described as follows [84, 96].

$$\boldsymbol{E}(\boldsymbol{r}) = \frac{q}{4\pi\varepsilon_0}\left(\frac{\boldsymbol{r} + d\,\boldsymbol{u}_x}{|\boldsymbol{r} + d\,\boldsymbol{u}_x|^3} - \frac{\boldsymbol{r} - d\,\boldsymbol{u}_x}{|\boldsymbol{r} - d\,\boldsymbol{u}_x|^3}\right) \tag{2.24}$$

Comparing Eqs. 2.21 and 2.24, however, it can be seen that the field described by Eq. 2.24 is that of two point charges. The second charge is located at $x = d = 20\,\mu\text{m}$ and of magnitude $-q$. The electric field of a single point charge in the vicinity of a metallic boundary is thus described by the sum of two point charges of opposing sign placed symmetrically with respect to the boundary.

This concept is commonly referred to as the concept of an "image charge". In principle, it can be generalized for more complicated charge densities or boundary geometries as follows. A potential function is generated as a sum of the charge density outside of the metallic domain and that of an arbitrary "image charge density" in the metallic domain. If this potential function satisfies the boundary conditions, it is the only solution to the system. This is due to the fact that the corresponding differential equation, $\Delta\Phi = \frac{\varrho(\boldsymbol{r})}{\varepsilon_0}$, only has a single solution [84].

Despite this general method, the practical calculation of electric fields can be challenging. This is a result of the fact that in many cases the charge density is not known. Additionally, in the case of several conductors, the potential distributions of the individual conductors cannot generally be added up. In this case, the potential distribution of one conductor would result in a varying potential at the position of another conductor. Since the potential in a conductor has to remain constant, however, this approach does not satisfy the boundary conditions.

This is in contrast to the calculation of magnetic fields using Biot-Savart's law. The reason for this is, that, unlike current densities, the charge densities in the individual conductors influence each other. Thus, in most cases, the solution of electrostatic problems can only be carried out using numerical methods. Notable examples are the

relaxation or finite difference method or finite element approaches as used in the present work.

DIELECTRIC BOUNDARIES Similar to Section 2.1.3, the following section will examine the influence of electric fields on non-conducting matter (i.e. dielectrics). In order to describe the response of such matter, the dielectric displacement $\boldsymbol{D}$ is introduced. In the presence of an electric field the following microscopic behavior can be assumed. The charge distribution of the individual atoms will rearrange so that the overall energy is minimized. The summed contribution of all atoms can be approximated as a dipole field, $\boldsymbol{P}$. Since the negative charges will rearrange towards regions of higher potential, this dipole will point in field direction. It has thus to be added to the electric field and $\boldsymbol{D}$ can described as

$$\boldsymbol{D} = \varepsilon_0 \, \boldsymbol{E} + \boldsymbol{P}. \tag{2.25}$$

Assuming a linear response of the material to the electric field, Eq. 2.25 can be written as

$$\boldsymbol{D} = \varepsilon_0 \, \boldsymbol{E} + \chi_{\mathrm{el}} \, \boldsymbol{E} = \varepsilon_0 \, (1 + \chi_{\mathrm{el}}) \boldsymbol{E} = \varepsilon_0 \, \varepsilon_{\mathrm{r}} \, \boldsymbol{E} = \varepsilon \, \boldsymbol{E}, \tag{2.26}$$

where the material dependent constants χ_{el} and ε_{r} were defined. χ_{el} is referred to as electric susceptibility and ε_{r} as relative permittivity. As can be seen from Eq. 2.26, they are related by $\varepsilon_{\mathrm{r}} = 1 + \chi_{\mathrm{el}}$. Table 2.2 gives a list of the electric susceptibilities of exemplary materials.

As can be seen from Table 2.2, the electric susceptibilities of materials can vary to a great extent. In contrast to diamagnetic materials in magnetic fields, the contribution of dielectric materials to electric fields is usually not negligible (compare Tab. 2.1). The following will

thus give an overview of how dielectric boundaries influence electric fields.

To this end, one can assume a system analogous to the one discussed above in the case of a conducting boundary [96]. A point charge q is located at $-d$ on the x-axis inside a medium of permittivity ε_1. The positive half of the x-axis is assumed to consist of a different medium of permittivity ε_2. In this case, the tangential components of the electric field on both sides of the boundary have to be identical. In addition, the normal components of the electric fields left and right of the boundary have to be related by the corresponding permittivities. The solution to this problem thus has to satisfy

$$\lim_{x\to 0^-} \left(\varepsilon_1 E_\mathrm{x}\, \boldsymbol{u}_\mathrm{x} + E_\mathrm{y}\, \boldsymbol{u}_\mathrm{y} + E_\mathrm{z}\, \boldsymbol{u}_\mathrm{z}\right) = \lim_{x\to 0^+} \left(\varepsilon_2 E_\mathrm{x}\, \boldsymbol{u}_\mathrm{x} + E_\mathrm{y}\, \boldsymbol{u}_\mathrm{y} + E_\mathrm{z}\, \boldsymbol{u}_\mathrm{z}\right). \quad (2.27)$$

Using this boundary condition, the electric field on both sides of the boundary can be calculated as

$$\boldsymbol{E}_{x<0}(\boldsymbol{r}) = \frac{1}{4\pi\varepsilon_1}\left(\frac{q\,(\boldsymbol{r}+d\,\boldsymbol{u}_x)}{|\boldsymbol{r}+d\,\boldsymbol{u}_x|^3} + \frac{q'\,(\boldsymbol{r}+d\,\boldsymbol{u}_x)}{|\boldsymbol{r}-d\,\boldsymbol{u}_x|^3}\right) \quad \text{and} \quad (2.28a)$$

$$\boldsymbol{E}_{x>0}(\boldsymbol{r}) = \frac{1}{4\pi\varepsilon_2}\,\frac{q\,(\boldsymbol{r}+d\,\boldsymbol{u}_x)}{|\boldsymbol{r}+d\,\boldsymbol{u}_x|^3}, \quad (2.28b)$$

where q' and q'' represent the following image charges [96].

$$q' = -\frac{\varepsilon_2-\varepsilon_1}{\varepsilon_2+\varepsilon_1}\,q \qquad q'' = \frac{2\,\varepsilon_2}{\varepsilon_2+\varepsilon_1}\,q \quad (2.29)$$

It can be seen from Eq. 2.28a, that the electric field for $x < 0$ is that of two point charges. Unlike in the case of a metallic boundary, however,

TABLE 2.2: Volume electric susceptibilities χ_{el} for common materials (adapted from [98]).

Material	χ_{el}
Air	5.89×10^{-4}
Polyimide	2.4
Silicon dioxide (SiO_2)	2.9
Silicon	10.68
Water	79.1

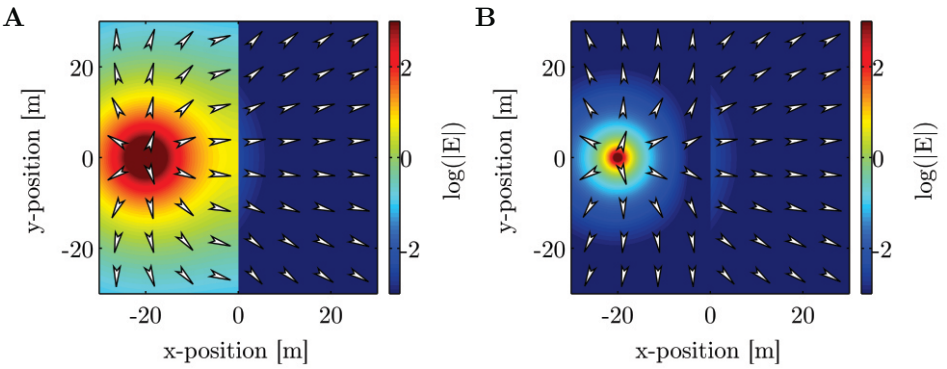

FIGURE 2.7: Field distribution of a point charge $q = 1.602 \times 10^{-19}\,\mathrm{C}$ located at $x = -d = -20\,\mu\mathrm{m}$ close to a dielectric boundary. **A:** Field distribution for $\varepsilon_1 = 3.4\,\varepsilon_0$ and $\varepsilon_2 = 80\,\varepsilon_0$. As can be seen, the electric field for $x > 0$ corresponds to that of a point charge located at $x = -d$. For $x < 0$, however, the field lines are deformed towards the surface by the image charge on the opposite side of the boundary. **B:** Field distribution for $\varepsilon_1 = 80\,\varepsilon_0$ and $\varepsilon_2 = 3.4\,\varepsilon_0$. As in **A**, the electric field to the right of the boundary remains that of a point charge. To the left of the boundary, however, the field lines are deformed away from the boundary. This is due to the fact, that for $\varepsilon_1 > \varepsilon_2$ the image charge q' is of the same sign as q.

the magnitude and sign of the image charge are determined by the factor $-\frac{\varepsilon_2-\varepsilon_1}{\varepsilon_2+\varepsilon_1}$. In the positive x-region, the electric field is that of a single point charge. Its sign is identical to that of q, but its magnitude is weakened by the factor $\frac{2\,\varepsilon_2}{\varepsilon_2+\varepsilon_1}$.

Figure 2.7 shows the electric field distributions for a charge of $q = 1.602 \times 10^{-19}\,\mathrm{C}$ located at $x = -d = -20\,\mu\mathrm{m}$. Figure 2.7A shows a calculation for $\varepsilon_1 = 3.4\,\varepsilon_0$ and $\varepsilon_2 = 80\,\varepsilon_0$. As in this case $\varepsilon_1 < \varepsilon_2$, the image charge q' has an opposing sign when compared to q (see Eq. 2.29). Similar to Figure 2.6, the field lines to the left of the boundary are thus deformed towards the boundary. To the right of the boundary, the field distribution is that of a point charge. Figure 2.7B shows the field distribution for $\varepsilon_1 = 80\,\varepsilon_0$ and $\varepsilon_2 = 3.4\,\varepsilon_0$. In this case q' is of the same sign as q and the field lines are thus deformed away from the surface. The right side of the boundary, however, remains equivalent to the field of a weakened point charge.

2.2.3 FORCE ON AN INDUCED ELECTRIC DIPOLE

The previous sections described fundamental properties of electric fields, as well as their interaction with conducting and non-conducting matter. In the experiments presented below, electric fields will be used to generate a repellent dielectrophoretic force on a polarizable particle. The following section will thus introduce the force an electric field exerts on a dielectric particle [48, 96].

The general expression for the force on an electric dipole can be given as follows [84].

$$\boldsymbol{F} = (\boldsymbol{m}_{\mathrm{el}} \cdot \nabla) \cdot \boldsymbol{E}, \tag{2.30}$$

where $\boldsymbol{m}_{\mathrm{el}}$ represents the electric dipole moment. For a dielectric particle, the induced dipole moment can be expressed as

$$\boldsymbol{m}_{\mathrm{el}} = 4\pi R^3 \varepsilon_{\mathrm{m}} \frac{\varepsilon_{\mathrm{p}} - \varepsilon_{\mathrm{m}}}{\varepsilon_{\mathrm{p}} + 2\,\varepsilon_{\mathrm{m}}} \boldsymbol{E}, \tag{2.31}$$

where R, refers to the radius of the particle and ε_{m} and ε_{p} refer to the permittivities of the medium and the particle, respectively. Combining Eqs. 2.30 and 2.31 yields

$$\begin{aligned} \boldsymbol{F} &= 4\pi R^3 \varepsilon_{\mathrm{m}} \frac{\varepsilon_{\mathrm{p}} - \varepsilon_{\mathrm{m}}}{\varepsilon_{\mathrm{p}} + 2\,\varepsilon_{\mathrm{m}}} \left(\boldsymbol{E} \cdot \nabla\right) \boldsymbol{E} \\ &= 2\pi R^3 \varepsilon_{\mathrm{m}} \frac{\varepsilon_{\mathrm{p}} - \varepsilon_{\mathrm{m}}}{\varepsilon_{\mathrm{p}} + 2\,\varepsilon_{\mathrm{m}}} \nabla \cdot \boldsymbol{E}^2, \end{aligned} \tag{2.32}$$

where $(\boldsymbol{E} \cdot \nabla) \cdot \boldsymbol{E} = \frac{1}{2} \nabla \cdot \boldsymbol{E}^2$ was used. The motion of a particle due to this force is referred to as dielectrophoresis. Similar to Eq. 2.18, this force depends on the gradient of the squared electric field. The overall sign of the force, however, also depends on the factor $\frac{\varepsilon_{\mathrm{p}} - \varepsilon_{\mathrm{m}}}{\varepsilon_{\mathrm{p}} + 2\,\varepsilon_{\mathrm{m}}}$. This factor is commonly referred to as the Clausius-Mosotti factor, f_{CM}. If the permittivity of the medium is greater than that of the particle (e.g. polymer particles in water), f_{CM} is positive and the force is attractive towards high-field regions. In the opposite case (e.g. polymer particles in air), $f_{\mathrm{CM}} < 0$ and these regions repel the particles. This is usually referred to as positive or negative dielectrophoresis, respectively.

The experiments in the present thesis make use of alternating electric fields to generate dielectrophoretic forces. In this case, Eq. 2.32 may be generalized for alternating electric fields as follows (see [48])

$$\boldsymbol{F}(\boldsymbol{r}) = 2\pi R^3 \varepsilon_{\mathrm{m}} f^*_{\mathrm{CM}} \nabla \cdot \boldsymbol{E}_{\mathrm{AC}}(\boldsymbol{r}, t)^2, \tag{2.33}$$

where f^*_{CM} refers to the Clausius-Mosotti factor in terms of complex permittivities

$$\varepsilon^*_{\mathrm{i}} = \varepsilon_0\,\varepsilon_{\mathrm{i}} - \mathrm{i}\,\frac{\sigma_{\mathrm{i}}}{\omega}. \tag{2.34}$$

$\boldsymbol{E}_{\mathrm{AC}}(\boldsymbol{r}, t)$ refers to an alternating electric field of the form

$$\boldsymbol{E}_{\mathrm{AC}}(\boldsymbol{r}, t) = E(\boldsymbol{r})\,\exp \mathrm{i}\,\omega t + \varphi. \tag{2.35}$$

The frequencies used in the experiments herein, are generally in the kHz regime and above. The effective force on the particle can thus be expressed as the temporal average of Eq. 2.33. Additionally, if a stationary field is used (i.e. $\varphi = 0$), Eq. 2.33 can be rewritten to

$$\langle \boldsymbol{F}(\boldsymbol{r}) \rangle = 2\pi R^3\,\varepsilon_{\mathrm{m}}\,\mathrm{Re}\,[f^*_{\mathrm{CM}}]\;\nabla \cdot \boldsymbol{E}_{\mathrm{rms}}(\boldsymbol{r})^2. \tag{2.36}$$

Here, $\mathrm{Re}\,[f^*_{\mathrm{CM}}]$ refers to the real part of the Clausius-Mosotti function described above. It has to be noted, however, that this factor is frequency dependent. This is due to the fact that at low frequencies the conductivity term in Eq. 2.34 dominates. At high frequencies, however, the permittivity term determines the behaviour. Depending on the materials in use and the medium, both of these terms can be functions of the frequency. The overall behavior of $\mathrm{Re}\,[f^*_{\mathrm{CM}}]$ is thus rather complex. Especially for particles like biological cells that are inhomogeneous or anisotropic, complicated frequency dependencies of $\mathrm{Re}\,[f^*_{\mathrm{CM}}]$ can result [47, 48]. For an isotropic polymer bead in water, however, $\mathrm{Re}\,[f^*_{\mathrm{CM}}]$ usually tends towards 1 for low frequencies (i.e. below $\approx$50 kHz) and towards -0.5 for high frequencies (i.e. above $\approx$50 MHz) [48].

2.3 RESISTIVE HEATING AND HEAT TRANSFER

The previous sections discussed fundamental aspects of magnetic and electric fields, their interaction with matter, and the forces exerted by these fields on susceptible particles. These aspects were described in the context of such particles as possible information transducers in the framework of highly-resolved mechanical or chemical stimulation of cells. The second part of this thesis, however, is concerned with the application of microwire array chips in the generation of highly-resolved thermal stimuli. The following section is thus intended to give the reader a fundamental information about the resistive heating of conductors, as well as the transport phenomena that apply in the spreading of this heat.

2.3.1 RESISTIVE HEATING

The following paragraphs are intended to give the reader a brief overview over resistive heating in conductors. A more rigorous and detailed treatment of this subject is given in standard references of solid state physics [99, 100].

As mentioned in the previous section, a conductor is classified by freely moving charge carriers. The majority of conducting materials are metals in which these charge carriers are represented by electrons. Referring to Bloch's theorem, the motion of these electrons can be described as that of free electrons in vacuum. In this setting, the effects of the potential created by the individual nuclei are summarized in an effective electron mass, m_{e}^{*}. Although m_{e}^{*} can deviate significantly

from the actual mass of the electron, m_e, this approximation is able to account for many effects in solid state physics [101].

When an electric field is applied to a metal, a force on the individual charge carriers results. This force is described in Eq. 2.20 and will accelerate the electrons in an opposite direction to that of the electric field. In the absence of an electric field, the velocity of the charge carriers is randomly distributed. The acceleration due to the electric field, however, will result in a net movement of the charge carriers. This net movement is macroscopically measured as a current. While moving through the solid, the charge carries will experience collisions with the surrounding lattice of nuclei. During these collisions, some of the kinetic energy of the electrons will be converted to vibrational energy in the lattice. These vibrations will result in an elevated density of the quasi-particles of the lattice vibrations (i.e. phonons). According to Debye's model, the effect of this increase in phonon density results in an increase in temperature in the conductor [99, 100, 102].

The microscopic treatment of this effect is discussed in more detail in the references given above. Macroscopically, the following dependence can be measured

$$P = U\,I, \tag{2.37}$$

where P is the power dissipated in the system, U the applied voltage, and I the current in the conductor. If Ohm's law applies to the conductor (i.e. $U = R\,I$), Eq. 2.37 can be rewritten as

$$P = \frac{U^2}{R}. \tag{2.38}$$

Here, R refers to the resistance of the conductor. For simple geometries, this resistance is expressed by Pouillet's law

$$R = \rho \frac{l}{A}, \tag{2.39}$$

with ρ as the material specific resistivity (i.e. the inverse of a material's conductivity σ), l as the length of the conductor parallel to the current direction, and A as the cross-sectional area normal to the current.

2.3.2 HEAT TRANSFER

As discussed in the previous section, the passage of a current through a conductor leads to the dissipation of power according to Eq. 2.37. The following section will introduce a basic differential equation for heat transfer by pure heat conduction. As with the previous section, the derivation will be restricted to a fundamental treatment. More detailed treatments can be found in standard references of statistical physics [103, 104].

In order to derive the differential equation governing heat transfer a gas in a non-equilibrium state may be assumed. This non-equilibrium state is assumed such that the temperature $T(x)$ at the positions $x_0 + \lambda$ and $x_0 - \lambda$ differs from that at x_0. The heat flux J (i.e. the heat per time and area) through this point can then be deduced as follows. The number of particles out of a volume $\mathrm{d}V$ that will cross an area $\mathrm{d}A$ at x_0 per time $\mathrm{d}t$ amounts to $\frac{n\,\mathrm{d}V}{\mathrm{d}A\,\mathrm{d}t} \approx \frac{1}{6}\,n\,\bar{v}$. Here n is the particle density in the system, which is assumed to be constant in space and $\bar{v}$ the average velocity of a particle in the system. If the heat capacity per particle is defined to be c, each of the particles crossing $\mathrm{d}A$ from $x_0 + \lambda$ will transport heat of $c\,T(x_0 - \lambda)$ through $\mathrm{d}A$. Similarly, the particles

from $x_0 - \lambda$ reduce this heat flux by $c\,T(x_0 + \lambda)$. The net heat flux through $\mathrm{d}A$ can thus be summed to

$$J \approx \frac{1}{6}\, n\, \bar{v}\, c \left(T(x_0 - \lambda) - T(x_0 + \lambda) \right) = -\frac{1}{3}\, n\, \bar{v}\, c\, \lambda\, \frac{\partial T}{\partial x}. \tag{2.40}$$

However, each particle will only reach $\mathrm{d}A$ if its velocity is not changed by a collision with another particle. The parameter λ thus has to be equal to the *mean free path* in the system. The factor $\frac{n\bar{v}c\lambda}{3}$ in Eq. 2.40 is commonly summarized as the thermal conductivity κ of a given material. Using this factor and generalizing for three dimensions, Eq. 2.40 becomes

$$\boldsymbol{J} = -\kappa\, \nabla T, \tag{2.41}$$

which defines the heat flux by conduction. While the above given derivation considered a gaseous system, the argumentation for Eq. 2.41 can be performed analogously for liquid systems. Using an appropriate quasi-particle system (e.g. phonons) it can also be extended to the case of solid materials.

Since heat is a conserved quantity, the continuity equation

$$\nabla \cdot \boldsymbol{J} - Q = -\kappa\, \Delta T - Q = 0, \tag{2.42}$$

with Q representing all heat sources in the system, has to be satisfied for all processes in the system[5]. As mentioned above, the heat flux is defined as energy per time and area. The heat flux emitted by a

[5]It has to be noted, however, that apart from a pure conductive heat flux as described above, convective and radiative heat transport (i.e. by the directed movement of mass or by radiation, respectively) can also participate in the overall heat flux in a system. These processes, however, are negligible in the systems presented in the current work and are thus not included in this section.

current-carrying conductor is thus related to the electrical power it dissipates and its surface. For a given set of boundary conditions and materials, the temperature distribution can thus be calculated using Eqs. 2.40 and 2.42. Since Eq. 2.42 represents a Poisson type equation, however, its analytical solution is only feasible for highly symmetric boundary conditions or simple geometries. In most practical systems, numerical methods (such as finite elements or relaxation methods) have to be used.

2.4 HIGH-RESOLUTION THERMOGRAPHY USING FLUORESCENCE LIFETIME IMAGING MICROSCOPY

The previous section presented basic information about resistive heating in conductors. Additionally, the theoretical background for the spreading of the heat in a system was presented. The direct measurement of temperature profiles or thermographs generated by micrometer-sized objects, however, can be challenging. This is due to multiple issues. Most standard measurement techniques (resistive/bimetallic sensors, laser thermometers, etc.) do not offer sufficient resolution or require direct contact with the sample. Infrared cameras cannot be combined with standard microscopy optics due to the limited transparency of optical glass in the infrared regime. Recently, several microscopy methods that operate in the visible range have been introduced to circumvent these limitations. These methods usually employ flourescence microscopy to measure temperature dependent changes in fluorescence intensity or lifetime [105]. The present work made use of

the latter approach via fluorescence lifetime imaging microscopy. The following is thus intended to give the reader a brief overview over the fundamental aspects of this measurement technique.

The intensity of an ensemble of fluorophores after excitation by a sufficiently short light pulse (i.e. much shorter than the lifetime of the fluorophore τ) is given as

$$I(t) = I_0 \exp -\frac{t}{\tau}, \tag{2.43}$$

where $I(t)$ is the intensity and τ the fluorophore's lifetime [106]. Using sufficiently fast detectors, this decay in fluorescence can be measured and the lifetime of the fluorophore can be determined. In order to measure temperatures, the lifetime's dependence on several factors is exploited. Besides temperature, the lifetime also depends on the solvent, as well as the electrolyte concentration. For a known set of parameters, however, the temperature at the measurement point can directly be deduced from the lifetime measurement.

Experimentally the quality of the measurement is often improved by averaging the expontial decay from multiple measurements before determining the lifetime by a fitting procedure. For performance reasons, pulsed lasers are excellent light sources in this context as they can deliver fast modulation at high intensities. In order to achieve high spatial resolution, the measurement can be coupled into a given microscope setup. The intrinsic reduction of stray light in confocal setups is a particular advantage in this context. In this way, it is possible to remotely probe temperatures of fL volumes with a relative accuracy in the low K regime [105].

2.5 Ca^{2+} WAVES IN CARDIOMYOCYTES

In this thesis, the effect of thermal stimuli of cells cultured on the microwire arrays was evaluated using cardiomyocyte-like HL-1 cells. In particular, monitoring of the intracellular Ca^{2+} concentration (via Ca^{2+} imaging) was performed to examine cell activity after stimulus or lesion. Thus, the following section is intended to give the reader a brief introduction into this cell type, as well as the concept of Ca^{2+} imaging.

2.5.1 CARDIOMYOCYTE EXCITATION-CONTRACTION COUPLING

The process referred to as excitation-contraction coupling is among the central processes in cardiomyocyte cell (i.e. heart muscle cells) [107]. This process describes the molecular pathways involved in the signalling between the electric excitation of a given cardiomyocyte (via an action potential; AP) and its mechanical contraction. It is thus fundamental to the heart's function.

The contraction of cardiomyocytes is perfomed by so-called myofilaments. Myofilaments are cytosceletal filaments that can be found in myocytes. They consist of actin and myosin filaments, referred to as thin and thick filaments, respectively. Upon binding to Ca^{2+}, actin-associated troponin exposes myosin binding sites on the thin filament. Consequently, myosin binding to the actin filaments can occur. After binding, the myosin filament pulls the actin filaments towards each other resulting in a contraction of the cardiomyocyte. The reversion of this process is an adenosin triphosphate (ATP) dependent cleavage of

the actin-myosin bond and an active removal of Ca^{2+}, which leads to a relaxation of the myocyte [108].

It can be seen that precise control over the intracellular Ca^{2+} concentration is crucial to the function of an individual myocyte and thus the heart as a whole. In mammals, this control is maintained by the mechanisms shown schematically in Figure 2.8. In the initial phase of the contraction, an influx of extracellular Ca^{2+} via voltage dependent Ca^{2+} channels is triggered by AP-associated depolarization (middle left in Fig. 2.8, voltage dependent Ca^{2+} channels depicted in yellow). In particular in the proximity of membrane invaginations referred to as t-tubules, this Ca^{2+} influx triggers so-called calcium-induced calcium release (CICR). This is due to the fact that in these regions, junctions between the sarcolemma and the sarcoplasmic reticulum (SR in Fig. 2.8) are present. As a result of these junctions, the Ca^{2+} influx directly triggers intracellular Ca^{2+} release from the SR by binding to ryanodine receptors (RyR in Fig. 2.8). In combination, the influx of extracellular Ca^{2+} and the intracellular Ca^{2+} release trigger the contraction of the myocyte as described above.

In order to relax the contraction, a decrease in intracellular Ca^{2+} concentration is required to trigger the dissociation of the Ca^{2+}-troponin complex described above [107]. This process is ATP-dependent and takes place via three main pathways. Firstly, the SR Ca^{2+} stores are refilled by the SR Ca^{2+} ATPase (ATP in the SR membrane in Fig. 2.8). The SR Ca^{2+} ATPase is located in the sarcolemmal membrane and transfers cytosolic Ca^{2+} into the lumen of the SR at the expense of ATP. Secondly, an exchange of Na^{+} and Ca^{2+}, as well as ATP dependent Ca^{2+} transport, between the extracellular space and the cytosol takes place. Furthermore, mitochondrial uniport participates

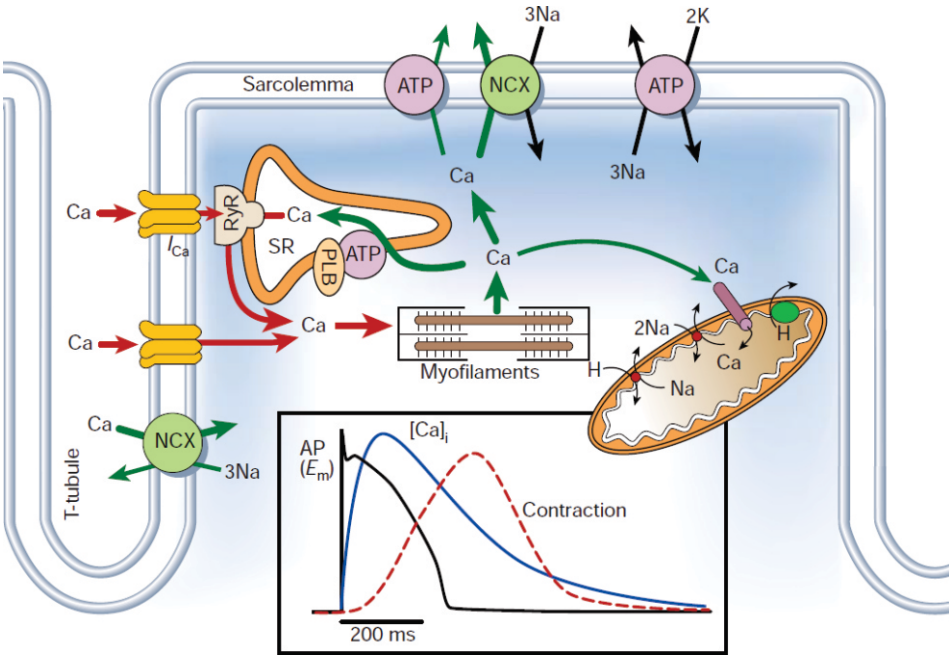

FIGURE 2.8: Ca^{2+} cycling in mammalian cardiymyocytes (reprinted with permission from [107]). An influx of extracellular Ca^{2+} via voltage dependent Ca^{2+} channels (shown in yellow on the middle left) leads to an opening of ryanodine receptors in the membrane of the sarcoplasmic reticulum. The open ryanodine receptors transport Ca^{2+} from the sarcoplasmic reticulum into the cytosolic space. This calcium-induced calcium release leads to a contraction of the myofilaments and thus the whole myocyte (center). After the excitation, ATP dependent Na^+/Ca^{2+} exchange and Ca^{2+} uniport towards the extracellular space (top), as well as mitochondrial Ca^{2+} uniport (middle right) restore the intracellular Ca^{2+} concentration. **Inlay:** Schematic plot of the temporal relations of the cardiac AP, Ca^{2+} influx, and the contraction.

in the restoration of the intracellular Ca^{2+} level as the third pathway. A temporal comparison of the time scales between the AP, the Ca^{2+} peak, and the actual contraction is shown in the bottom graph in Figure 2.8.

The above described mechanisms explain the process of contraction in an individual cardiomyocyte. In the standard experimental setting, however, these cells are grown as a confluent layer. Under these conditions cardiomyocytes form gap junctions (i.e. electrical synapses) between neighboring cells. Consequently, a sufficiently strong depolarization by an AP, for instance, can spread throughout the cell layer. Additionally, a certain percentage of cells is capable of spontaneously generating APs. In combination, this usually leads to the following behavior of cultured cardiomyocytes. When cultured at a sufficient density, the cell layer is comparable to a conducting sheet of cells. In combination with this conductivity, the spontaneous activity in some of the cells leads to the formation of a so-called pacemaker. This pacemaker is a spontaneously active cell that, via the gap junction coupling periodically excites the whole sheet of cells. Any AP generated in the pacemaker will be followed by according activity in the neighboring cells that spreads throughout the sheet. Due to the periodic nature of the spontaneous activity and the isotropic spreading through the layer, this is commonly referred to as Ca^{2+} waves.

The above given mechanisms describe cardiac excitation-contraction coupling in mammalian primary cardiomyocytes. Instead of primary cells, however, the HL-1 cell line was used in the present experiments. The HL-1 cell line was derived from a mouse atrial cardiomyocyte tumor and is known to show essential characteristics of adult cardiomyocytes [109]. They are known to have expression patterns close

to those of adult cardiomyocytes, although missing their defined ultrastructure [109]. Despite this reduced intracellular organization, they show spontaneous electric activity, Ca^{2+} cycling, and mechanical contraction.

2.5.2 Ca^{2+} IMAGING

As described in the previous section, oscillations in the intracellular Ca^{2+} concentration are crucial to the natural function of cardiomyocytes. As a result, monitoring the intracellular Ca^{2+} concentration allows to draw direct conclusions on the functional state of the cell. In order to quantify the function of cardiomyocytes during or after thermal treatment, Ca^{2+} imaging, a remote fluorescence-based Ca^{2+} detection technique, was used.

The measurement of Ca^{2+} has been a long on-going challenge in physiology [110]. Since the development of a reliable class of Ca^{2+} binding fluorophores in the 1980s [111], however, flourescent Ca^{2+} imaging has become one of the most common methods [110]. The basic principle behind Ca^{2+} imaging is the following. A fluorescent dye is loaded into a cell. Upon binding to Ca^{2+}, this dye changes its fluorescent properties (i.e. intensity or wavelength). This change is then monitored via an optical microscope and allows conclusions about the intracellular concentration of free (or accessible) Ca^{2+}.

The key difference of the fluorophores introduced by Tsien and coworkers [111] is that, upon Ca^{2+} binding, these dyes undergo a change in fluorescence wavelength rather than intensity. Additionally, their overall fluorescence is 30fold brighter than that of the dyes reported before [111].

In order to load the dyes into the cell, several strategies can be pursued [110]. As they commonly exhibit larger aromatic groups, most dyes are impermeable to the cell membrane. For comparably small dye molecules (such as the fluo-4 dye used in this thesis), the so-called esther loading is a common method [112]. In this context, the fluorescent dye is functionalized with acetoxymethyl groups. These groups can be used to temporarily mask charges in the dye molecule in order to render it membrane permeable [112]. After diffusing through the cell membrane, intracellular esterases cleave off the acetoxymethyl groups. This ensures a high intracellular dye concentration even after removal of the staining solution.

In order to determine the actual concentration of Ca^{2+}, two approaches are usually employed. On the one hand, the change in fluorescence at a single wavelength may be measured. On the other hand, the intensity ratio between two wavelengths (usually the emission wavelength of the Ca^{2+} bound and the free dye) may be used. From these measurements, the Ca^{2+} concentration $[Ca^{2+}]$ the following relations can be used

$$[Ca^{2+}] \propto K_D \frac{F - F_{min}}{F_{max} - F} \qquad \text{single-wavelength} \tag{2.44a}$$

$$[Ca^{2+}] \propto K_D \, \beta \frac{R - R_{min}}{R_{max} - R} \qquad \text{ratiometric,} \tag{2.44b}$$

where F and R is the measured fluorescence intensity or ratio, respectively, F_{min} and R_{min} refer to the minimum fluorescence or ratio (i.e. in the absence of Ca^{2+}), respectively, F_{min} and R_{max} to the maximum flourescence intensity or ratio at saturating Ca^{2+} concentrations, re-

specitvely, β is the ratio of the fluorescence intensities at the wavelength in the denominator of R, and K_D the dye's dissociation constant.

As the exact concentration of the dye in the cell is not accessible, the concentration deduced from Eqs. 2.44a or b have to be calibrated. To this end, an *in vitro* calibration with Ca^{2+} solutions of known concentrations may be performed. However, due to K_D's dependence on the pH, the ion strength, or the temperature of the environment, this may result in inaccuracies. A possible alternative is given by *in vivo* calibration methods. These include mild membrane perforation by ionophores or tensides combined with extracellular Ca^{2+} buffers, or micropipette-based intracellular dialysis. Both of these approaches intend to control the intracellular Ca^{2+} level in order to obtain intracellular calibration curves. It has to be noted that these methods can have a substantial influence on the intracellular concentrations of other compounds besides Ca^{2+} and may thus alter cell behavior.

In order to obtain a qualitative signal that corresponds to the intracellular Ca^{2+} concentration (as is the case in the experiments presented here), however, calibration is not necessary. In this case, the so-called pseudoratio

$$\frac{\Delta F}{F} = \frac{F - F_{\text{base}}}{F_{\text{base}} - B}, \tag{2.45}$$

where F_{base} represents the fluorescence before the Ca^{2+} peak and B represents the background fluorescence from areas adjacent to the cell. While not allowing for a quantitative measurement, this pseudoratio can be used as an approximate measure of the intracellular Ca^{2+} concentration.

The Ca^{2+} measurements in this thesis were recorded using a hardware-based sequential subtraction in order to achieve an increased grey-scale

resolution. Consequently, an absolute normalization as the one given in Eq. 2.45 was not possible. This normalization was performed according to

$$F_{norm} = \frac{F - \langle F \rangle}{\langle F \rangle}, \tag{2.46}$$

where F_{norm} and F represent the normalized and current fluorescence, respectively, and $\langle F \rangle$ the temporal average of the fluorescence (for further details, see Section 3.3.2).

CHAPTER 3

MATERIAL & METHODS

3.1 DEVELOPMENT OF A SETUP FOR ON-CHIP ELECTROMAGNETIC ACTUATION AND THERMAL STIMULATION

In the experiments presented in this thesis, microwire crossbar arrays were used in the context of chemical, mechanical, and thermal stimulation of cells. In order to efficiently use these microwire array chips in the experiments, a flexible solution to supply the individual wires with current was needed. To this end, a voltage source capable of supplying each of the 34 wires with a computer controlled voltage was designed in collaboration with the electronic workshop.

To actuate the magnetic particles at the chip's surface, currents of up to 0.1–1 A can be necessary ot induce sufficiently strong mangetic fields. The voltage that is needed to supply a wire with a desired current is determined by its resistivity via Ohm's law, $U = RI$. Due to fabrication reasons, the resistivities of the wires in the initial batches varied between 100 and 400 Ω. Thus, in principle, voltages in the range of 10–400 V would be necessary. However, in order to avoid the use of high power electronics, the maximum voltage applicable to a single wire was limited to 25 V. Using this maximum voltage, a first 8 channel test system was designed and built by the electronic workshop.

As described in Section 2.2.3, the necessary frequency range for repulsive dielectrophoresis depends on the medium and the particle. As discussed, a quantitative prediction about the crossover from positive to negative dielectrophoresis can be difficult. For a qualitative assessment, however, a wide range of frequencies was necessary (depending on the system, the crossover frequencies for dielectrophoresis can vary

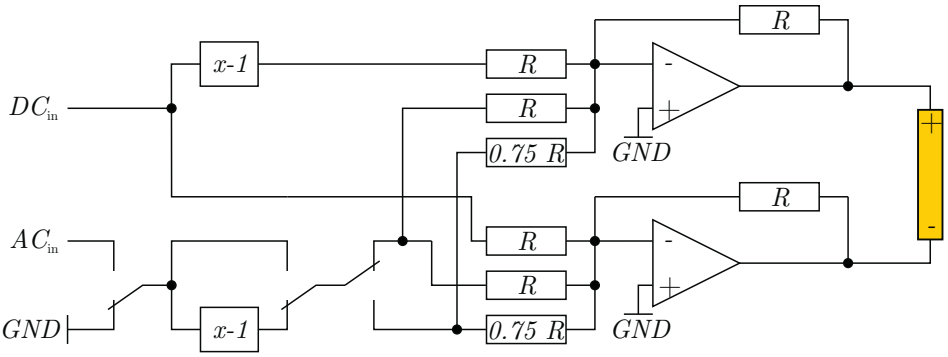

FIGURE 3.1: Schematic of the circuit of an individual channel of the driving circuit. The DC voltage used to generate the currents for magnetic actuation is shown as DC_{in}. This signal is split, one part of it is inverted, and both parts are then directed to the contacts of a single wire (shown in yellow). The AC signal generated by an external function generator, AC_{in}, is passed on to both ends of the wire. It can be modified by inversion or multiplication with a factor of 0.75 to give $-AC_{\text{in}}$, $-0.75AC_{\text{in}}$, $0.75AC_{\text{in}}$, and AC_{in} as possible AC amplitudes at both ends of the wire.

from the kHz to the MHz regime). At the same time, the amplitudes necessary to exert significant dielectrophoretic forces on the particles are at least in the range of tens of volts. Thus, an external function generator was used to generate the AC signal.

Figure 3.1 shows a simplified schematic of a single channel's circuit. A microcontroller (not shown) is used to define the DC voltage for the channel. This value is then converted to an analog voltage (DC_{in} in the upper left of Fig. 3.1) by a digital-to-analog converter. The signal is then divided into two parts. After inverting one of the parts, both are directed to the ends of a given wire (depicted in yellow) via operational amplifiers. The effective potential difference along the wire thus amounts to $2DC_{\text{in}}$.

As mentioned above, the AC signals necessary for the dielectrophoretic actuation of particles were supplied by a function generator. The input signal of this function generator is shown as AC_{in} in the lower left of Figure 3.1. It is passed through to both contacts of the wire as the potential difference for the dielectrophoretic actuation is applied between two different wires. To this end, one of the wires' AC signal can be inverted. To supply different wires with varying amplitudes, the function generator's input can also be modified by a factor of $amp = 0.75$. The AC amplitudes that can thus be applied to the wires comprise $-AC_{\text{in}}$, $-0.75AC_{\text{in}}$, $0.75AC_{\text{in}}$, and AC_{in}.

After initial testing, this concept was expanded to a 34 channel version (Fig. 3.2A, top middle). The remaining connections to the chip were designed to fit in a standard electrophysiological setup (see Figs. 3.2B and C). Figure 3.2A shows a schematic of the overall connections. A LabView® software was used to communicate via USB with the power supply's internal microcontroller. The output signals of the power supply are then transferred to the actual chip socket (right side of Fig. 3.2A) via cables and custom printed circuit boards (PCBs).

Figures 3.2B and C show photographs of the final system. As can be seen in Figure 3.2B the chip socket is mounted to a combination of x-, y-, and z-micromanipulators to allow precise positioning of the chip under the microscope. In order to minimize mechanical drift during the experiments, the chip socket can be screwed to the microscope table. Figure 3.2C shows a close-up photograph of the white square in Figure 3.2B. The top connections of the chip were designed in order to minimize the use of space above the chip. As can be seen in Figure 3.2C, this allows for easy access of the microwire array with microcapillaries for single particle deployment.

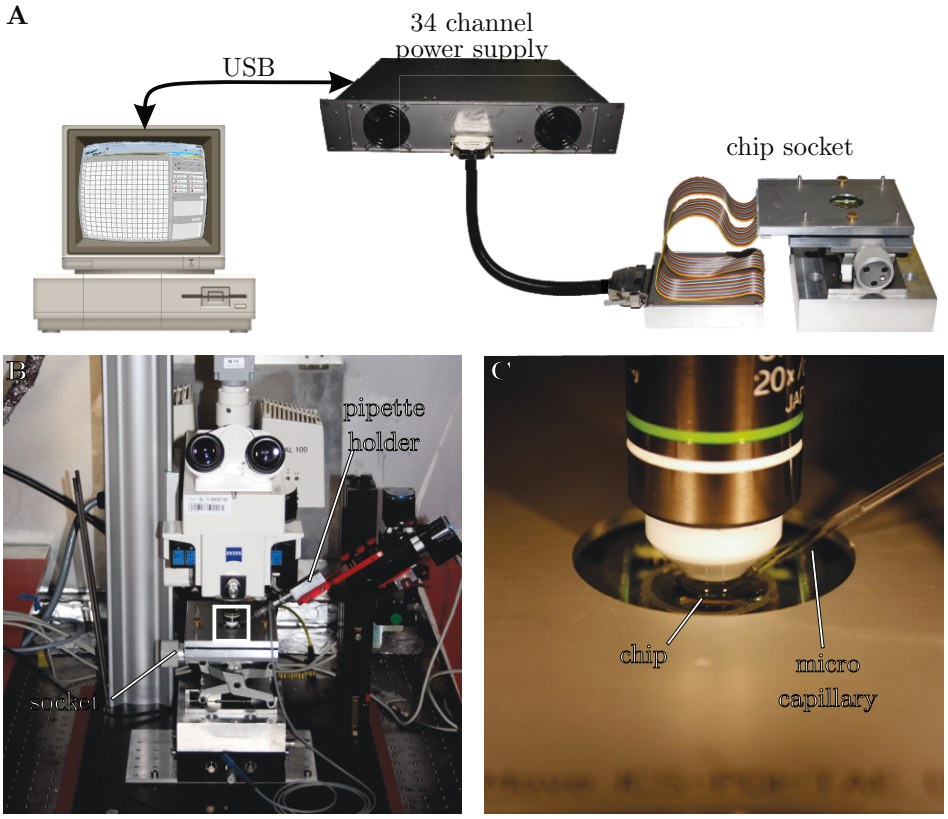

FIGURE 3.2: Schematic and photographs of the electronics and connections used in the final setup. **A:** Schematic of the individual connections. The power supply is controlled via a custom LabView® program connected via USB. The output of the power supply is directed to the contact pads via cables and custom PCBs. **B** and **C:** The chip socket is mounted to a combination of x-, y-, and z-manipulators and screwed to the optical table of the setup. The top side of the connections is designed to maximize the chip's accessibility for single particle deployment via microcapillaries.

As mentioned above, the microcontroller in the power supply was adressed via USB using custom LabView® software. For the initial test version of the power supply, this software was programmed by the electronic workshop and offered the following basic functions. As the bandwidth of the USB connection did not allow for live communication, prewritten voltage protocols were used. These protocols comprised a table with a voltage and an AC parameter for each of the eight channels. Due to memory limitations of the microcontroller, the protocols were restricted to a maximum length of 1000 rows. However, in order to be able to perform longer or more complex protocols, individual lines of the protocol could be tagged as part of a loop and repeated for a given number of times. In addition, this test software was capable of reading the resistivities of the individual wires.

In devising the final version of the software (see Figs. 3.3-3.5), my aim was to allow comfortable and flexible control over the particles. Instead of prewritten protocols with calculated voltages, a schematic of the chip was used as the central control element. Nevertheless, I kept the concept of a table with voltage values for each wire. This table, however, was processed internally. The main mode of the software is depicted in Figure 3.3. As can be seen, this mode shows a schematic of all 16×16 possible trap positions on the chip. Each of the 16×16 positions was programmed as a button that can be clicked by the user. When clicking a certain position, a "hold" or "move" action could be chosen. Figure 3.4A shows an exemplary image of a position marked with the hold option (indicated in red). After marking a desired position in this way, the "write" button could be used to add the voltage values necessary for a trap at this position to an internal table.

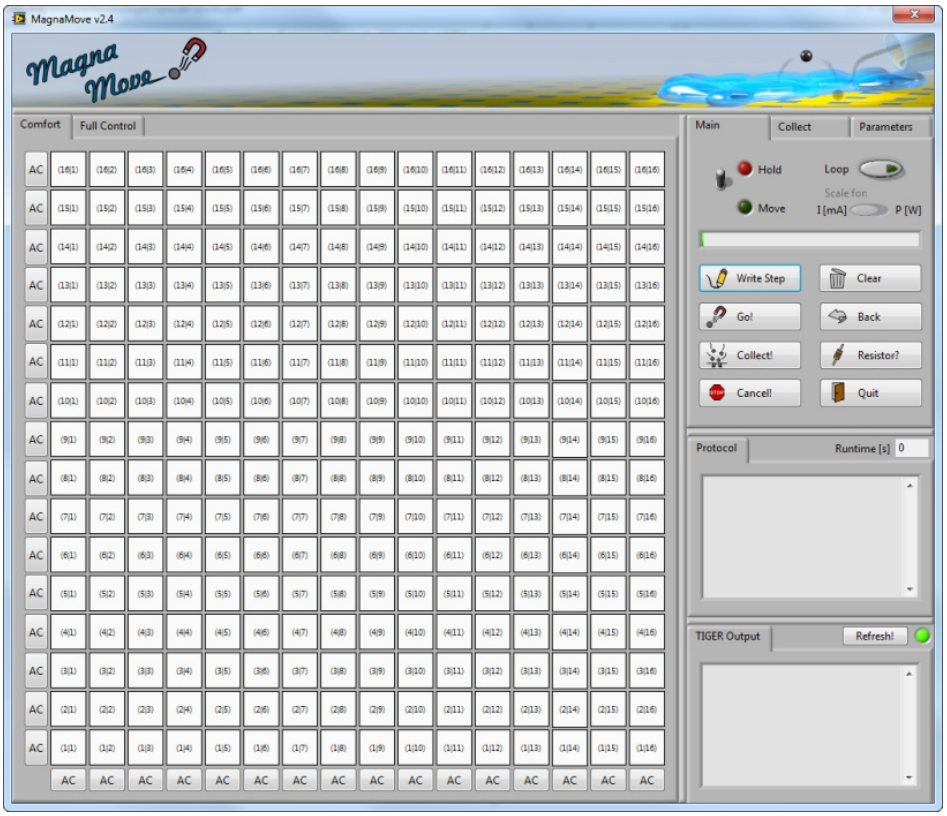

FIGURE 3.3: Screenshot of the first operation mode of the software developed to apply currents to the microwire arrays. This "comfort" mode allows the user to select one of the 16×16 possible positions in the array. The software can automatically generate the current protocols necessary to create a trap at this position. This trap can then be moved by clicking a desired target location's button. In this case, the software automatically generates a sequence of switching procedures (according to the "intermediate switching" protocol described in Section 4.1.1).

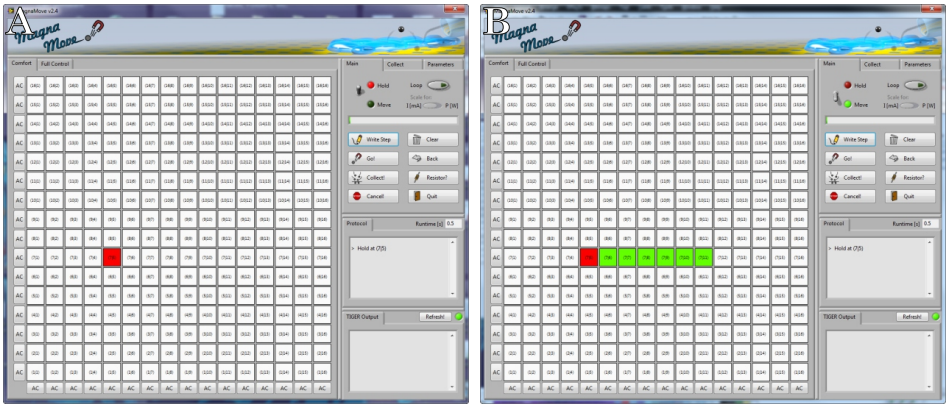

FIGURE 3.4: Screenshots illustrating the use of the "comfort" mode. **A:** A desired position is marked in the "hold" mode (indicated in red). Clicking the "write" button at this point will generate voltages that correspond to a magnetic trap at this point on the chip. **B:** In order to relocate a trap, the "move" mode can be activated. Clicking a desired target position will then mark the path from the current location to that target cell in green. At this point, the "write" button will generate a corresponding sequence of switching steps from source to target location according to the "intermediate switching" protocol.

In order to move the particle between different traps, a position can be determined as a target location. This can be done by simply clicking at the desired target position with the "move" option active. As shown in Figure 3.4B, the path from the current trap to the desired target position will then be marked in green. In this case, clicking the "write" button will automatically append a sequence of switching steps to the internal array. The switching procedure used in this case is further described as "intermediate switching" in Section 4.1.1. Finally, the complete sequence can be sent to the microcontroller and executed using the "go" button.

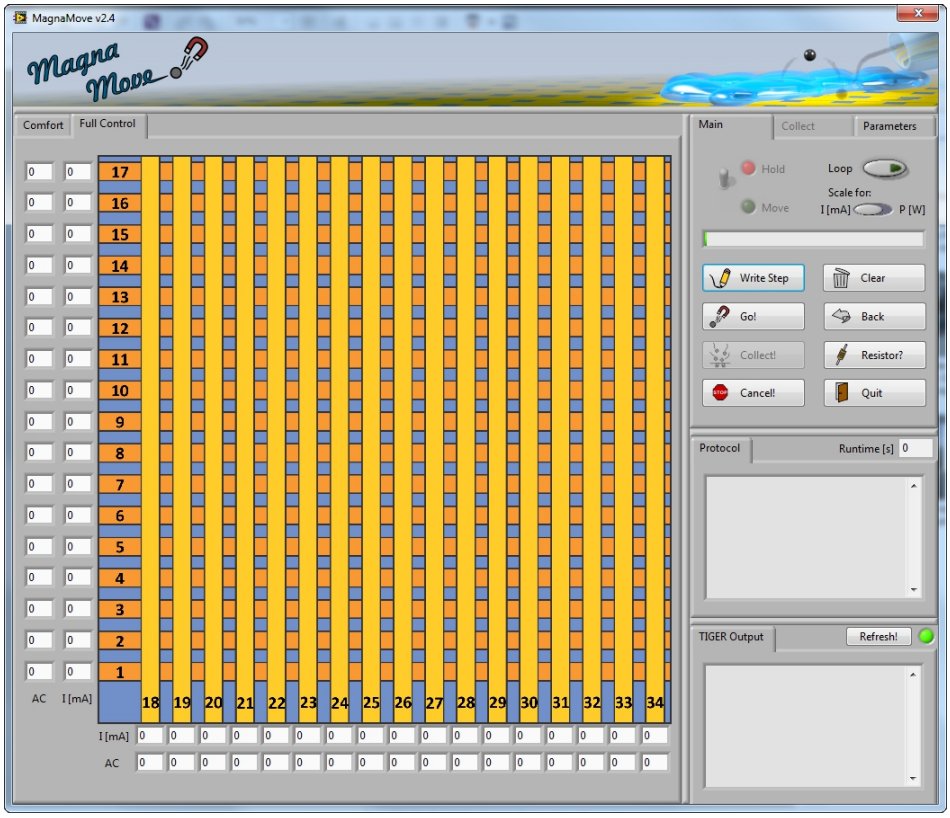

FIGURE 3.5: Screenshot of the second operation mode of the software. In this "full control" mode, the user is enabled to control the currents in all of the wires individually. To this end, a schematic showing all 34 wires is displayed. The current for each wire can be entered in the corresponding input field and the sequence can be sent to the power supply. In addition to the definition of currents, AC factors of 1, 0.75, -0.75, and -1 can be given for each channel. For the application of thermal stimuli, the software can be set to use the input of the user as a desired electrical power.

In order to allow for further development of the switching protocols and for switching sequences not covered by the software's main mode, a second "full control" mode was developed (see Fig. 3.5). This mode features a schematic view of the individual wires of the array. Using the corresponding input fields, the user can define an arbitrary current for each wire. The complete current state can then be attached to the internal protocol and executed as described above. Additionally, both modes allow for the application of AC signals to given sets of wires. In the first mode, the two wires next to a given row or column of positions can be set to AC values of plus or minus AC_{in}. In the second mode, arbitrary patterns of the four possible AC values given above can be applied to individual wires. Both modes also allow for the use of loop structures to facilitate the creation of long or repetitive protocols.

In order to allow for the controlled application of thermal stimuli to cells cultured on the chips, the "full control" mode can also be used. In the operation modes described above, the current values entered by the user are converted to voltages using Ohm's law. However, when using the microwire arrays for the application of thermal stimuli, the electrical power applied to a wire is a more appropriate measure than the electric current. The software can thus be set to apply voltages that correspond to a given electrical power. Together with the measured resistivity of the corresponding wire, the value entered by the user is registered as electrical power and the corresponding voltage is calculated using $U = \sqrt{PR}$.

3.2 EXPERIMENTAL PROCEDURES

3.2.1 CHIP FABRICATION

Microwire array chips for particle actuation and on-chip thermal stimulation were fabricated in our clean-room as follows: Briefly, silicon wafers (Si-Mat Silicon Materials, Kaufering, Germany) were oxidized under wet conditions to grow 1 µm of silicon oxide for substrate insulation. The first layer of the actual microwire array was then patterned via photolithography using a double layer resist (LOR3B and NLOF2020, microresist technology, Berlin, Germany). After optical exposure and development (AZ 726 MIF, AZ Electronic Materials GmbH, Wiesbaden, Germany), a given metal stack was deposited (see Table 3.1). Subsequent to a lift-off in acetone, the resulting layer of microwires was insulated from the following layer by plasma enhanced chemical vapor deposition (PECVD; Sentech Instruments GmbH, Berlin, Germany) of a silicon oxide/silicon nitride/silicon oxide stack (ONO; 100 nm/50 nm/100 nm in thickness, respectively). The second set of wires was then structured identical to the first but with orthogonal orientation. Finally, a second passivation layer was deposited and the contact pads were opened. This layer either consisted of another

TABLE 3.1: Different metal stacks used for the microwire arrays.

metal stack (respective layer thicknesses in nm**)**	**evaporation method**
Ti/Au/Ti (10/150/7.5)	electron beam
Ti/Au/Cr (10/300/15)	electron beam
Ti/Al/Ti (10/300/15)	sputtered

stack system of silicon oxide and silicon nitride (ONONONONONONO; 150 nm/75 nm in thickness, respectively; total layer thickness: 1.5 µm) or a layer of spun cast polyimide (PI-2545, HD microsystems GmbH, Neu-Isenburg, Germany). In the former case, a photoresist (AZ 5214 E, AZ Electronic Materials GmbH, Wiesbaden, Germany) was lithographically patterned (AZ 726 MIF) and the contact pads were opened via reactive ion etching (RIE). In the latter case, the polyimide was processed to achieve a layer thickness of 1.4 µm. To this end, the wafer dehydrated and the VM-652 adhesion promoter (HD microsystems GmbH, Neu-Isenburg, Germany) was applied for 45–60 s. The wafer was spun dry at 3000 rpm for 30 s and heated to 100 °C for 60 s. Afterwards, the polyimide was spin coated at 6000 rpm for 30 s and a soft bake was performed at 120 °C for 4 min. The contact pads were opened via photolithography (AZ 5214 E) and chemical wet etch of the polyimide (AZ 726 MIF) and a hard bake was performed at 350 °C for 30 min. After dicing of the individual chips, a glass ring was glued to the chip using polydimethylsiloxane (PDMS; Sylgard 184, Dow Corning Corporation, Midland, MI, USA). The PDMS was mixed at a ratio of 1:10 (base/curing agent; w/w) and cured at 110 °C for 30 min (unless otherwise noted PDMS was processed in this way). A schematic of a chip as well as a photograph of an encapsulated chip is shown in Figure 3.6.

3.2.2 MAGNETIC PARTICLE ACTUATION

ACTUATION AND COLLECTION OF CLOUDS OF MAGNETIC PARTICLES

For the collection of particle clouds from a suspension, superparamagnetic screenMAG particles (see Table 3.2) were suspended in distilled

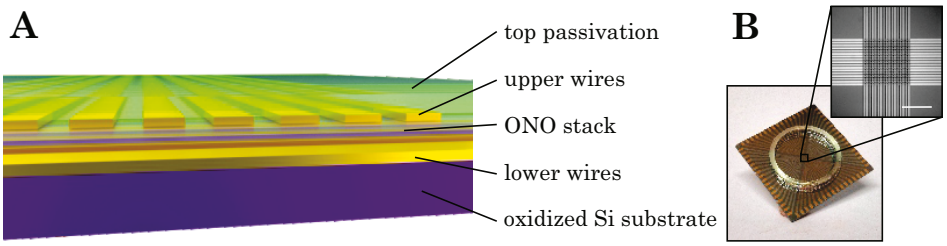

FIGURE 3.6: Schematic and photograph of the microwire array chips. **A** 3-dimensional schematic of the individual parts of the microwire array chip. An oxidized Si wafer (blue) was used as a substrate to deposit and structure the first set of wires (gold). This set of wires is then passivated by an ONO stack (blue transparent) followed by the deposition and structuring of the second set of wires (gold). Finally, the chip is passivated with either an ONO stack or a polyimide layer (green transparent). **B** Photograph of a microwire array chip with a glass ring glued to it. **Inlay:** Photomicrograph of the actual microwire array consisting of two times 17 wires (scale bar: 150 µm).

water. 400–500 µL of the resulting suspension were then pipetted into the glass ring in the center of the chip. In order to collect a defined cloud of particles from the suspension, two approaches were tested. The first approach was the activation of a magnetic trap as shown in Figure 3.7A. The second approach comprised the alternating application of current to the two horizontal and the two vertical wires surrounding the desired target position (see Figure 3.7B). In both cases, activated wires (indicated by the white arrows in 3.7) were supplied with 50 mA per wire. Unless otherwise noted, "active wires" in all experiments were supplied with 50 mA. In order to evaluate the collection efficiency, particle concentrations of approximately 10^6 particles mL^{-1} were used. After applying one of the collection patterns for 10–15 min, the particle distribution was examined. To this end a CCD camera (PL-B782U, PixeLINK, Ottawa, Canada) coupled to an optical mi-

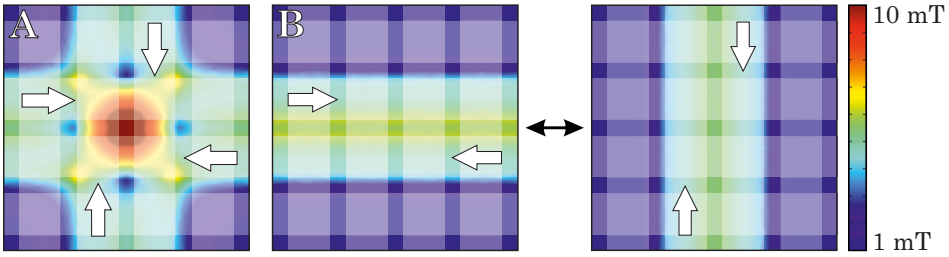

FIGURE 3.7: Simulated magnetic fields at the chip's surface for the two collection approaches. **A** shows the magnetic field and the current pattern for an active magnetic trap (wire positions indicated by the shaded areas; active wires and current directions indicated by white arrows; FEM simulation with 100 mA per active wire). **B** shows the magnetic fields for the horizontal and vertical current pulses. **Color scale:** 1–10 mT as indicated in **B**. Reprinted and modified with permission from [113].

croscope (Zeiss Axiotech Vario with W Plan-Apochromat 63x/1.0 or UMPlanFl 20xW/0.5 objectives; further purchased from Carl Zeiss Microscopy GmbH, Gttingen, Germany, latter purchased from Olympus Deutschland GmbH, Hamburg, Germany) was used.

In order to determine a simple and reliable protocol for the actuation and transport of the particle clouds on the chip, three current patterns were tested. At first, a direct transition between the initial and the target current state was applied. This current profile resulted in an almost intermediate relocation of the magnetic field peak (Figure 3.8, middle path). In the second approach, a smooth transition between initial and target state was tested by ramping the currents from the initial state's pattern to that of the target cell (Figure 3.8, upper path). The third protocol evaluated in the experiments included two intermediate steps with only three wires carrying current during these intermediate steps (Figure 3.8, lower path). For all three protocols the switching efficiency was evaluated. To this end, defined particle

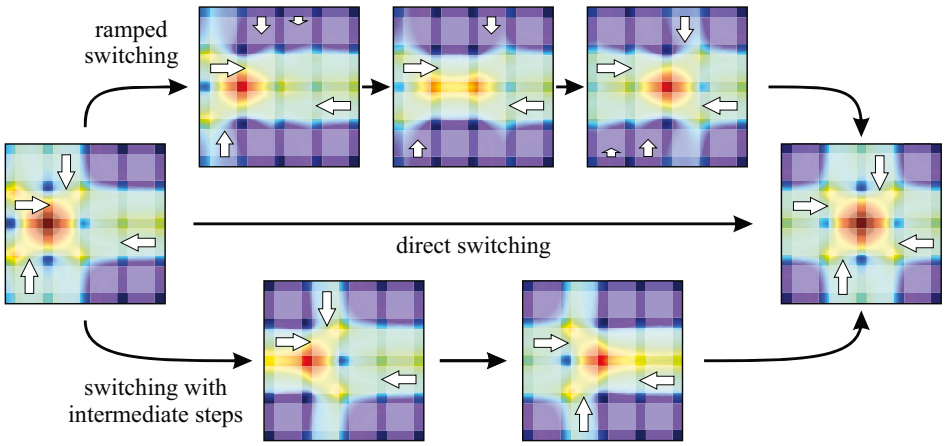

FIGURE 3.8: Simulated magnetic fields at the chip's surface for the different switching protocols (FEM simulation with 100 mA maximum current per wire; wire positions indicated by the shaded areas, current directions indicated by the white arrows; color scale as in Figure 3.7). The middle path shows the direct switching protocol. The top path shows the magnetic fields of the linear switching protocol at 25, 50, and 75% completion of the switching process. The lower path shows the intermediate switching protocol. Reprinted and modified with permission from [113].

clouds of 15-20 particles were collected from a low concentrated particle suspension (10^3 particles mL^{-1}) by applying the above described collection protocol for 10–15 min. The switching efficiency was then determined by counting the average percentage of particles transferred during a single jump.

ACTUATION AND TRACKING OF SINGLE PARTICLES AT THE CHIP SURFACE The actuation of single particles was carried out as follows: A micropipette with a tip opening of approximately 5–6 µm was pulled from a glass capillary (BF150-86-10, Sutter Instrument, Novato, CA, USA) using a laser-based pipette puller (P-2000, Sutter

Instrument, Novato, CA, USA). The capillary was then loaded from the back with particle suspension at an aproximate concentration of 10^3 particles mL^{-1}. Subsequently, a small volume of paraffin oil was loaded into the capillary to reduce the effect of pressure fluctuations in the capillary. 400–500 µL of a given actuation medium were then pipetted onto the chip and the capillary was brought into the proximity of an active magnetic trap (compare Figure 3.7) on the chip. The application of a gentle overpressure to the capillary could then be used to deploy and trap individual particles. Table 3.2 shows a summary of the different particles used in the experiments.

The tracking of an individual particle was performed using the screenMAG particles (see Table 3.2). In order to analyze particle trajectories, a single particle was deployed in an active magnetic trap as described above. For the actuation of the particle, the "intermediate switching" protocol (see 3.2.2) was then applied and the particle motion was recorded. Using a custom MatLab® script (see Section 3.3.1), the particle's trajectory was then extracted and compared with an analytical simulation of the system (see Section 3.3.3).

3-DIMENSIONAL ACTUATION OF INDIVIDUAL PARTICLES The 3-dimensional actuation of particles was carried out using the M-270 carboxyl particles (see Table 3.2). At first, the levitation height in dependence of the current per wire and the amplitude of the AC signal were tested. To this end, a magnetic trap was activated at 5, 10, and 15 mA per wire. A particle was then deployed into the trap according to the above described protocol and the microscope was focused at the particle. Subsequently, an AC signal of 2 MHz was applied to wire configurations surrounding this trap at different amplitudes. The

TABLE 3.2: Different magnetic particles used in the experiments.

Commercial name (Supplier)				
Hydrodynamic radius, R_{hydr}	Core material	Bead material	Surface functionality	Dispersity
screenMag silanol (chemicell GmbH, Berlin, Germany)				
0.5 µm	Maghemite (γ-Fe_2O_3)	Silica	Silanol (-Si-OH)	polydisperse
MyOne Carboxyl (Life Technologies GmbH, Darmstadt, Germany)				
0.5 µm	Maghemite (γ-Fe_2O_3)	Polystyrene	Carboxyl (-COOH)	monodisperse
M-270 Carboxyl (Life Technologies GmbH, Darmstadt, Germany)				
1.35 µm	Maghemite (γ-Fe_2O_3)	Polystyrene	Carboxyl (-COOH)	monodisperse
M-270 Amine (Life Technologies GmbH, Darmstadt, Germany)				
1.35 µm	Maghemite (γ-Fe_2O_3)	Polystyrene	Amine (-NH)	monodisperse

microscope was then focused at the particle's new position during which the change in z-position was detected using the microscope's z-stage. Furthermore, relocating the particle to different positions in a given plane was tested in order to grant full 3-dimensional control over the particle's position.

3.2.3 CULTURE OF HL-1 CELLS ON THE MICROWIRE ARRAY CHIPS

For the culture of cardiomyocyte-like HL-1 cells, the chips were cleaned and coated as follows: The chips were cleaned in 70% EtOH and dried with pressurized nitrogen in a standard sterile work bench. To promote cell adhesion to the chips, 400 µL of a protein solution containing 5 µg mL^{-1} fibronectin (Sigma, St. Louis, MO, USA) and 0.02 µg mL^{-1} gelatin (Fisher Scientific, Hampton, NH, USA) were pipetted into the glass ring in the center of the chip and incubated for approximately 60 min. The chips were then rinsed once with distilled water and immediately used for cell culture experiments. Subsequent to the experiments, the medium was exchanged for 400 µL of protease solution (containing trypsin and ethylenediaminetetraacetic acid; 0.05% Trypsin-EDTA(1x), Life Technologies) and the chips the chips were incubated at 37 °C over night. The chips were then rinsed with deionized water, immersed in bidestilled water and treated with ultrasound for 15 min. After shortly rinsing with 70% EtOH and drying with pressurized air, the chips were ready to be reused for further experiments.

To minimize medium evaporation and ensure maintaining sample sterility during experiments under ambient conditions, sterile lids were

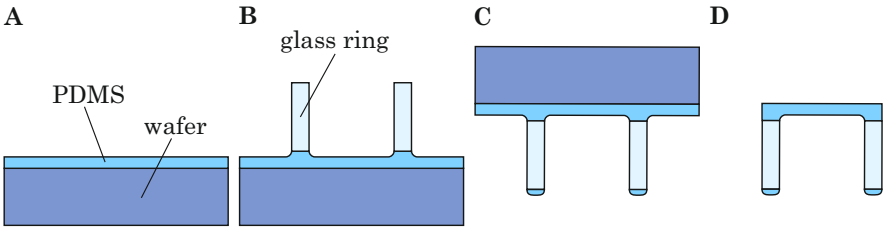

FIGURE 3.9: Schematic of the sterile lid fabrication. **A-D:** A thin layer of PDMS is spun cast to a fluorosilanized wafer and cured (**A**). Subsequently, a glass ring is glued to the wafer using PDMS (**B**). The top side of the ring is then dipped into a thin layer of PDMS and cured upside down to yield a sealing lip (**C**). Finally, the lid is detached from the wafer and excess PDMS is removed (**D**).

used in all cell culture experiments not involving immersion objectives. The sterile lids were produced as follows: An oxidized silicon wafer was fluorosilanized under protective gas atmosphere. To this end, the wafer was hydroxylized in O_2 plasma (80 W, 1 mbar, 5 min; plasma oven: Pico, Diener electronic GmbH + Co. KG, Ebhausen, Germany) and transferred into an Ar protective gas atmosphere. Subsequently, the wafer was transferred into a desiccator containing a small beaker with 100 µL trichloro(1*H*,1*H*,2*H*,2*H*-perfluorooctyl)silane. Silanization was performed at 5 mbar for approximately 1 h. The wafer was then spin-coated with PDMS at 200 rpm for 90 s and cured. Subsequent to curing, glass rings were glued to the top layer using PDMS. The top side of the rings was dipped into a small amount of PDMS and the system was cured again to yield a sealing lip. Finally, the individual lids were detached from the wafer and excess PDMS was removed using a scalpel. Figure 3.9 shows a schematic of the indicidual steps of the lid fabrication.

The cardiomyocyte-like cell line "HL-1" was cultured as follows: A maintenance culture was kept at 37 °C and 5% CO_2 in a T-25 tissue-culture plastic flask. The standard culture medium consisted of Claycomb medium (SAFC Biosciences, Lenexa, KS, USA) supplemented with 10% fetal bovine serum, 100 U mL^{-1} Penicillin, 100 µg mL^{-1} Streptomycin, 2 mM L-glutamine (all purchased from Life Technologies GmbH, Darmstadt, Germany), and 0.1 mM norepinephrine (Sigma). When confluency and mechanical contraction of the cells were reached, the culture was split as follows: The culture medium was aspirated and the flask was rinsed with 1 mL of trypsin/EDTA solution. After short rinsing, the solution was exchanged for 1 mL of fresh trypsin/EDTA solution and the flask was placed in the incubator for approximately 5 min. Subsequently, the bottom of the flask was rinsed with 5 mL of fresh medium and the resulting 6 mL were centrifuged at 1700 rpm for 5 min. After centrifuging the supernatant was aspirated and the cell pellet was rersuspended in 1 mL of fresh medium. Appropriate fractions to achieve confluency on the chips or in the flask on a given day were then taken and plated onto the substrates in a total volume of 5 mL in the case of a T-25 flask and 400 µL in the case of a chip. The medium was exchanged daily and the chips were additionally covered with a sterile lid (see above) to minimize medium evaporation and osmolarity changes during incubation.

3.2.4 THERMAL LESION

Apart from applications in the actuation of magnetic beads, the microwire crossbar chips were also used to introduce localized thermal stress on cells cultured at the chip's surface. In order to characterize the

cell layer's response to thermal stimuli of varying strength, stimuli of increasing electrical power (1, 1.5, and 2 W per wire) were successively applied to two neighboring wires. Unless otherwise noted, all stimuli were applied for 1 min with breaks of 1 min between individual stimuli. Ca^{2+} imaging sequences of 1 min were recorded before the first stimulus, during and in between the individual stimuli, as well as 5 min after the last stimuli. To this end, Fluo-4 AM dissolved in dimethylsulfoxide (0.5 mM; purchased from Life technologies and Sigma, respectively) was added to the culture medium at a dilution of 1:200 (v/v) and the samples were incubated for approximately 30 min. After incubation, the medium was aspirated and exchanged for 400 µL of fresh medium. The samples were then transferred into the setup where the application of the thermal stimuli as well as Ca^{2+} imaging was performed.

To inflict lesions along certain wires, sets of two neighboring wires were used in all experiments. In these experiments, the samples were transferred from the incubator without opening the lid and two thermal stimuli of 2 W were applied to each desired lesion site in the afternoon of the second day *in vitro* (DIV). Subsequently, the medium on the chips was exchanged for 400 µL and the samples were transferred back into the incubator. Ca^{2+} imaging or live/dead staining was then performed in the morning of DIV 3. Analysis of the Ca^{2+} imaging data was performed using a custom MatLab® script (see Section 3.3.2).

For the assessment of lesion success, live/dead staining was performed. Here, calcein AM and ethidium homodimer (EtHD, both purchased from Sigma) were dissolved in phosphate buffered saline (PBS) at a concentration of 4 µM each. The medium on a given sample was then aspirated, 400 µL of the stain PBS were pipetted to the chip, and the sample was incubated for 10–15 min. Subsequent to incuba-

tion, the stain solution was aspirated and 400 µL of bare PBS were pipetted to the chip. Photomicrographs of the sample's green and red fluorescence, as well as differential interference contrast (DIC) images, were then obtained using a Zeiss AxioImager Z1 with a W N-Achroplan 20x/0.5 objective (both purchased from Carl Zeiss GmbH).

In order to record thermographs of the active chips, fluorescence lifetime imaging microscopy (FLIM) was used. To this end, approximately 20 µL of Rhodamine B (0.3 mg mL^{-1} in distilled water; purchased from Sigma) were encapsulated on the chip using silicon grease and a glass cover slip. The sample was then mounted in a laser scanning microscope (Olympus IX-71 with FV3-294 confocal unit and PicoQuant FLIM system) and the fluorescent decay data was recorded. The data was preliminarily processed with the SymPho Time software (PicoQuant) to produce lifetime images. Subsequently, the temperature images were calculated from the lifetime images by means of custom Python scripts using a calibration curve from [105].

3.3 DATA ANALYSIS AND SIMULATION

3.3.1 TRACKING OF INDIVIDUAL MAGNETIC BEADS

As mentioned in 3.2.2, a custom MatLab® script was used to extract the trajectory of a single particle that was actuated at the chip's surface. Briefly, this script performed the following processing steps for each frame: In order to enhance the particle's visibility in the image, the background (either the first frame of the video or the average of all frames) was subtracted and the result was multiplied by a varying amplification factor. Depending on the quality (i.e. magnification,

brightness, contrast) of the individual videos, this amplification factor was tuned to reduce noise and maximize tracking precision. The image was then converted from an RGB image to a monochromatic intensity image. Using a MatLab® implementation of Otsu's method (the `video.Autothresholder` class), the frame was thresholded to a binary image [114]. Similar to the above mentioned amplification factor, the threshold computed via Otsu's method was also modified to achieve better tracking quality. Subsequently, an analysis for connected regions in the binary image was performed. To this end, the binary image is scanned for pairs of "connected" pixels, where a pixel was considered as "connected" to another pixel if the latter was among its eight neighbors. Groups of mutually connected pixels were counted as regions and the size and centroid of each region was evaluated. In the following, only regions within a certain size range (depending on the particle size and the magnification) were analyzed. This evaluaion was performed using the `video.BlobAnalysis` class implemented in MatLab®). The aforementioned amplification and threshold factors, as well as this size criterion, were adjusted manually in order to detect one region at most (i.e. the particle's position or noise). The centroid of this region was then evaluated for its distance to the last detected position. Depending on the exposure time and possible particle velocity, a maximum step distance between two successive frames was defined and the centroid was only noted if it followed this limit. The resulting sequence of $x/y/t$-values was then converted from pixels to µm by manually measuring the scale factor from one of the video frames. Similary, the time scale was converted from frame number to s by multiplication with the exposure time for each frame. Finally, the

origin of the trajectory was manually aligned with that of the analytical simulation and the resulting x/t- or y/t-traces were plotted.

3.3.2 Ca^{2+} PROPAGATION ANALYSIS

The analysis of the Ca^{2+} imaging data described in Section 3.2.4 was performed via a custom MatLab® script. Briefly, this script comprised the following steps: At first, the video was down-sampled to a frame size of 32×32 pixels for performance reasons. The resulting 32×32 intensity traces were then normalized by calculating $I_{norm} = \frac{I-\langle I \rangle}{\langle I \rangle}$, where I is the intensity of the individual pixel in the corresponding frame and $\langle I \rangle$ its average intensity over time. Subsequently, each intensity trace was smoothed using a Gaussian filter with a window width of 300 ms.

In order to discriminate active from inactive pixels, $\langle I_{norm}^4 \rangle^{\frac{1}{4}}$ was evaluated. The resulting matrix was converted to a binary activity mask using its minimum value plus two times its standard deviation as a threshold. Similar to the tracking of individual magnetic beads, this mask was then searched for "connected" regions. In this case, however, only a lower limit for the size of the regions was used to limit the detection to regions that comprised multiple cells. This analysis was performed using the `regionprops` function. As a reference trace for the following correlation analysis, the average intensity trace of each of the regions was then calculated. By cross-correlating each pixel of a region with the region's reference trace, the relative signal delay inside of the region was detected.

In order to analyze the connectivity of the individual regions, as well as the signal delay in between connected regions, the reference

traces of all regions were cross-correlated. All regions with a correlation exceeding a threshold of 70% were then sorted in a distinct group of regions. Subsequently, the interregional delay in each of the groups was corrected for by cross-correlating the individual reference traces and shifting the whole group to a minimum delay of 0. For visualization of the data, all inactive pixels were then marked as gray and each group of connected regions was assigned a color. The delay values were then mapped to a scale starting from a mixture of the corresponding color with 50% black for the minimum delay up to a mixture of the corresponding color and 50% white for the maximum delay. In this way, the connectivity could be displayed as color while the signal propagation is displayed in the "brightness" of a given color.

3.3.3 ANALYTICAL SIMULATION OF THE MAGNETIC FIELDS

In order to simulate the particle's motion at the chip's surface, an analytical simulation was used. To this end, the particle's velocity at a given moment in time was calculated as follows. Referring to Eq. 2.19, the force on a magnetic can be expressed as

$$\boldsymbol{F}_{mag} = \frac{V\,\chi_{\text{particle}}}{\mu_0}\,\nabla \boldsymbol{B}^2. \tag{3.1}$$

When actuated in a fluid medium, the particle also experiences a drag force. This drag force is given by Stokes' law as

$$\boldsymbol{F}_{drag} = -6\,\pi\,\eta\,R_{hydr}\,\boldsymbol{v}. \tag{3.2}$$

Here, η is the dynamic viscosity of the medium, R_{hydr} is the particle's hydrodynamic radius, and $\boldsymbol{v}$ its velocity. Neglecting any particle-surface interactions these two forces can be equated and the result can be solved for the particle's velocity:

$$\begin{aligned} \boldsymbol{F}_{mag} &= -\boldsymbol{F}_{drag} \\ \frac{V\,\chi_{\text{particle}}}{\mu_0}\,\nabla \boldsymbol{B}^2 &= 6\,\pi\,\eta\,R_{hydr}\,\boldsymbol{v} \\ \boldsymbol{v} &= \frac{V\,\chi_{\text{particle}}}{6\,\pi\,\eta\,R_{hydr}\,\mu_0}\,\nabla \boldsymbol{B}^2 \end{aligned} \tag{3.3}$$

Using a linear approximation of the particle's velocity for sufficiently small time steps Δt and separating the individual components, this can be modified to:

$$\Delta x = \frac{V\,\chi_{\text{particle}}}{6\,\pi\,\eta\,R_{hydr}\,\mu_0}\,\frac{\partial}{\partial x}\left(B_x^2 + B_y^2 + B_z^2\right)\,\Delta t \tag{3.4a}$$

$$\Delta y = \frac{V\,\chi_{\text{particle}}}{6\,\pi\,\eta\,R_{hydr}\,\mu_0}\,\frac{\partial}{\partial y}\left(B_x^2 + B_y^2 + B_z^2\right)\,\Delta t \tag{3.4b}$$

$$\Delta z = \frac{V\,\chi_{\text{particle}}}{6\,\pi\,\eta\,R_{hydr}\,\mu_0}\,\frac{\partial}{\partial z}\left(B_x^2 + B_y^2 + B_z^2\right)\,\Delta t, \tag{3.4c}$$

where Δx and Δy are incremental changes in the particle's position, Δt is an incremental change in time, and B_x, B_y, and B_z refer to the x-, y-, or z- components of the magnetic flux density, respectively. However, as the particle's motion is resitricted to the chip's surface, changes in z-position can be neglected. To simulate the particle's motion at the chip's surface, Eq. 3.4 and the expressions for the magnetic flux density given in Section 2.1.2 were implemented in a custom LabView® program.

3.3.4 NUMERICAL SIMULATION OF THE MAGNETIC AND ELECTRIC FIELDS

SIMULATION GEOMETRY Apart from the above described analytical simulation of the magnetic fields, a numerical simulation was prepared. Here, the magnetic and electric fields used for the 3-dimensional actuation of the particles were simulated. To this end, a small section of the array's geometry was modeled. Figure 3.10 shows a schematic of this section. The overall size of the section in x- and y-direction was referred to as W. The height of the section was referred to as H. The microwire array comprised four wires in x- and four wires in y-direction. The width of the individual wires was referred to as w_{wire} and their height as h_{wire}. The interwire distance was referred to as w_{inter}.

Similar to the actual microwire arrays, the substrate used for the simulation was an oxidized silicon wafer. The height of this thermal oxide layer was referred to as h_{ThOx}. The layout of the passivation layers, however, was changed compared to the real chips. In particular, the ONO passivation in between both wire layers was neglected. Instead, both layers were embedded in a single polyimide layer with a thickness of h_{PI} as shown in Figure 3.10.

For the simulation of magnetic fields, a given set of wires was supplied with a current of I_0. In the case of the electric fields, the desired wires were set to a potential of V_0. Table 3.3 shows the default values ofr all parameters. Unless otherwise noted these values were used in the simulation.

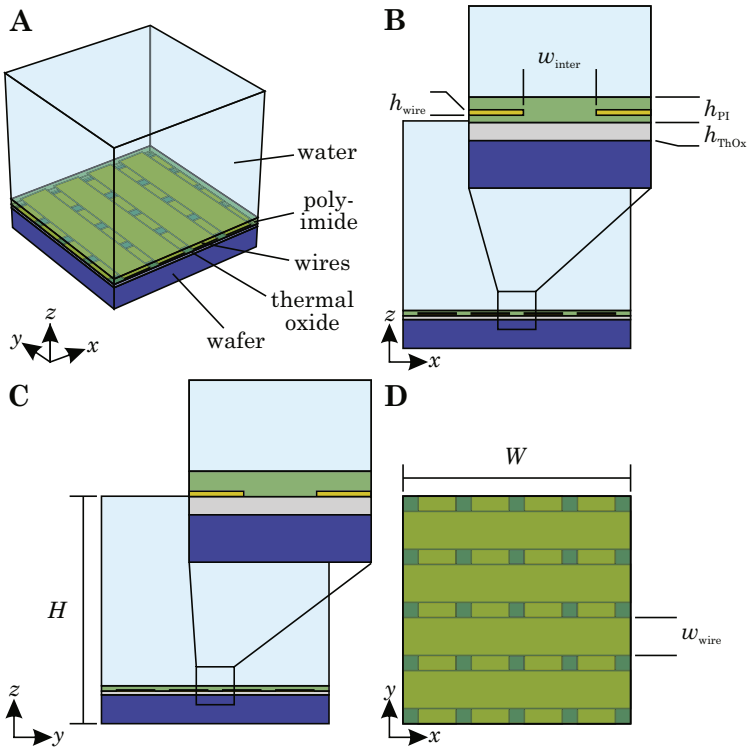

FIGURE 3.10: Schematic of the geometry used in the numerical simulations. **A:** Overview of the complete geometry. An array of 4×4 wires is modeled on top of an oxidized silicon wafer. Both layers are embedded in a polyimide layer. **B:** Cross-sectional view in the x-z-plane. The height of the thermal oxide, the wires, and the polyimide, as well as the interwire distance, are indicated (h_{ThOx}, h_{wire}, h_{PI}, and w_{inter}, respectively. **C:** Cross-sectional view in the y-z-plane indicating the overall height of the model H. **D:** View in the x-y-plane displaying the overall width of the model and the individual wires (W and w_{wire}, respectively).

MAGNETIC FIELDS Apart from the above described analytical simulation of the magnetic fields, a numerical simulation of the magnetic and electric fields used for the 3-dimensional actuation of the particles was used. This simulation was carried out using Comsol®, a commercial finite element method (FEM) software. Here, the magnetic fields were calculated using the "magnetic fields" module. This module uses Ampere's law and the definition of the magnetic vector potential to describe a static magnetic field.

$$\nabla \times \boldsymbol{H} = \boldsymbol{J} \tag{3.5a}$$

$$\boldsymbol{B} = \nabla \times \boldsymbol{A} \tag{3.5b}$$

Here, $\boldsymbol{H}$ is the magnetic field, $\boldsymbol{J}$ is the current density in the system, and $\boldsymbol{A}$ is the magnetic vector potential. Combining Eq. 3.5b with the constitutive relationship for the magnetic flux density, $\boldsymbol{B} =$

TABLE 3.3: Default values for the parameters used in the simulation.

Parameter	Description	Value
H	height of the model	60 µm
W	width/depth of the model	60 µm
w_{wire}	width of a single wire	10 µm
w_{inter}	width of the interwire spacing	4 µm
h_{wire}	height of a single wire	0.3 µm
h_{ThOx}	height of the thermal oxide	1 µm
h_{PI}	height of the polyimide	1.4 µm
V_0	amplitude of the AC input signal	10 V
I_0	current per wire	50 mA

$\mu_0 (\boldsymbol{H} + \boldsymbol{M})$, Eq. 3.5a can be rewritten as:

$$\boldsymbol{J} = \mu_0^{-1} \nabla \times (\nabla \times \boldsymbol{A}) - \nabla \times \boldsymbol{M}. \tag{3.6}$$

Using this equation, Comsol® calculates the magnetic vector potential and the magnetic fields for a given current density defined by the user. For each wire, this current density was obtained by dividing the current I_0 by the cross-sectional area of the wire.

As described above, the evaluation of the force on a magnetic particle involves spatial derivatives of the magnetic flux density. However, the x-, y-, and z- components of the magnetic flux density calculated by the "magnetic fields" module are given as scalars. In order to allow for the calculation of the force on a magnetic particle, an additional module for custom partial differential equations (PDE) was thus used. This module makes use of the general coefficient form of a PDE:

$$e_a \frac{\partial^2 u}{\partial t^2} + d_a \frac{\partial u}{\partial t} + \nabla \cdot (-c \nabla u - \alpha u + \gamma) + \beta \cdot \nabla u + a u = f, \tag{3.7}$$

where u is an independent variable, e_a is the mass coefficient, d_a is a damping coefficient, c is the diffusion coefficient, α is the conservative flux convection coefficient, γ is the conservative flux source term, β is the convection coefficient, a is the absorption coefficient, and f is the source term. In order to use this module to calculate a magnetic flux density that can be differentiated, a was set to 1, $\boldsymbol{f}$ was set equal to $\boldsymbol{B}$, and all other coefficients were set to 0. In this way the magnetic flux density calculated by the "magnetic fields" module was effectively copied to the PDE module. The resulting vector field $\boldsymbol{u}$ is thus equivalent to the magnetic flux density in the system. In contrast

to the magnetic flux density calculated by the "magnetic fields" module, however, it can be differentiated as it is not given in the form of a scalar quantity.

ELECTRIC FIELDS In order to calculate the electric fields, the "electrostatics" module was used. Similar to the "magnetic fields" module used in the previous section, this module uses Gauss' law and the definition of the electric potential,

$$\nabla \cdot \boldsymbol{D} = \boldsymbol{\rho} \tag{3.8a}$$

$$\boldsymbol{E} = -\nabla V, \tag{3.8b}$$

to describe the electric field in the static case. Here, $\boldsymbol{D}$ is the electric displacement, ρ is the charge density of the system, $\boldsymbol{E}$ is the electric field, and V represents the electric potential. Combining Eq. 3.8b with the constitutive relationship for the electric displacement, $\boldsymbol{D} = \epsilon \boldsymbol{E} + \boldsymbol{P}$, Eq. 3.8a can be rewritten as:

$$\rho = -\nabla \cdot (\epsilon \nabla V - \boldsymbol{P}), \tag{3.9}$$

where ϵ is the permittivity of the surrounding medium. In contrast to the magnetic field calculated by the "magnetic fields" module, the electric field calculated for a given potential distribution can be differentiated and could thus be directly used for the force calculations.

3.3.5 NUMERICAL SIMULATION OF THE TEMPERATURE DISTRIBUTION AT THE CHIP'S SURFACE

Using the geometry described above, the temperature distribution in the system was simulated. In order to simulate this temperature distribution at the chip's surface during the application of thermal stimuli, the "heat transfer" module of Comsol® was used. To calculate the temperature distribution and the heat flux in a system, this module uses the heat equation

$$\rho C_p \left(\frac{\partial T}{\partial t} + (\boldsymbol{u} \cdot \nabla) T \right) = - (\nabla \cdot \boldsymbol{q}) + \boldsymbol{\tau} : \boldsymbol{S} - \frac{T}{\rho} \frac{\partial \rho}{\partial T}\bigg|_p \left(\frac{\partial p}{\partial t} + (\boldsymbol{u} \cdot \nabla) p \right) + Q. \quad (3.10)$$

Here, ρ is the density, C_p the specific heat capacity at constant pressure, T is the absolute temperature, $\boldsymbol{u}$ is the velocity vector, $\boldsymbol{q}$ is the heat flux by conduction, p is the pressure, $\boldsymbol{\tau}$ is the viscous stress tensor, $\boldsymbol{S}$ is the strain-rate tensor, Q contains heat sources other than viscous heating, and ":" refers to the contraction operator. Furthermore, Fourier's law of heat conduction,

$$\boldsymbol{q} = -\boldsymbol{k} \nabla T, \quad (3.11)$$

where k is the thermal conductivity, is used. Assuming a static case with $\frac{\partial T}{\partial t} = 0$, ignoring viscous heating and pressure work, and inserting Eq. 3.11 in Eq. 3.10 yields

$$\rho C_p \boldsymbol{u} \cdot \nabla T = \nabla \cdot (k \nabla T) + Q. \quad (3.12)$$

Using this equation, Comsol® calculates the temperature distribution for a system of given heat sources.

CHAPTER 4

RESULTS & DISCUSSION

4.1 Electromagnetic actuation of magnetic microparticles

4.1.1 Collection and actuation of clouds of magnetic microparticles

Particle collection The first part of the present thesis is concerned with the application of magnetic microparticles in the chemical or mechanical stimulation of cells. To this end, a reliable and precise control of the particles is of crucial. In order to examine the controlled and precise actuation of magnetic particles using microwire crossbar arrays, an efficient and simple protocol to collect these particles from a suspension was developed. The most direct approach to collect particles from a solution is the activation of a magnetic trap as shown in Figure 4.1A. The figure shows the result of an FEM simulation of the magnetic field at the chip's surface. The current direction used in the simulation is indicated by the white arrows ($I_0 = 100\,\mathrm{mA}$). Applying current to the four wires surrounding a given position in the array can be compared with a current-driven loop. As such, the magnetic field (depicted as false color plot in Fig. 4.1A) is strongest in the center of the four wires. As described in Section 2.1.4, this leads to a magnetic force attracting particles in the vicinity towards this maximum in the magnetic field.

Figure 4.1C shows the particle distribution after applying this protocol for 15 min to a particle suspension of approximately 10^6 particles mL^{-1}. The particles used in this experiment were monodisperse particles with a diameter of 2.7 µm (see Table 3.2; M-270 carboxyl). A group of

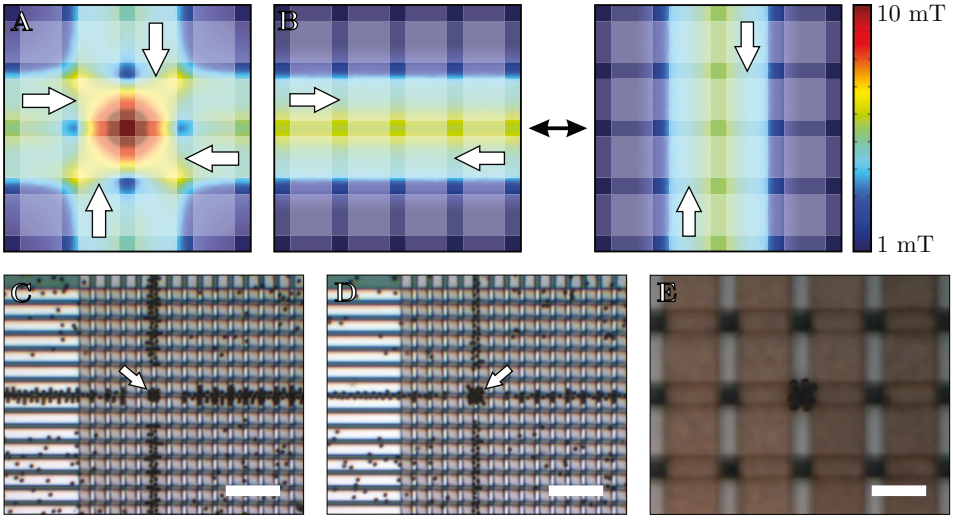

FIGURE 4.1: Magnetic field and particle distributions for the collection of particle clouds from a suspension. **A and B:** False color plots of the magnetic field at the chip's surface for a permanent trap and the alternating collection protocol, respectively. The positions of the wires are indicated by the shaded areas. Active wires are marked with white arrows ($I_0 = 100\,\text{mA}$; modified and reprinted with permission from [113]). The color scale in **B** applies to **A** as well. **C** and **D:** Particle densities at the chip's surface after applying the protocols shown in **A** and **B** (respectively) for 15 min. Almost all particles within a range of 20–30 µm around the active wires are trapped and a defined group of particles is collected at the desired target location (marked with an arrow). In the case of **D** the ratio of particles trapped at the target position to those trapped along the wires is significantly increased. Scale bar: 50 µm **E:** A defined cloud of 1 µm particles. Scale bar: 10 µm.

particles was collected at the desired target location in the center of the frame. However, a significant amount of particles was also trapped along the active wires. Furthermore, it can be seen that the trapping of the particles appears very effective within a range of 20–30 µm around the active wires. As a result, the particle density in this region is notably decreased.

In order to increase the ratio of particles trapped at the target location to those trapped along the feedlines, a second collection protocol was examined. In this protocol an alternating sequence of currents applied to two horizontal or two vertical wires was used. Figure 4.1B shows the magnetic fields at the chip's surface for these current patterns ($I_0 = 100\,\mathrm{mA}$). During the application of the horizontal pulses, the force only attracts particles in the vertical direction and vice versa. Both of these pulses were applied in successively for 5 s each for a total duration 15 min. Figure 4.1D shows the particle distribution after applying this protocol to a suspension of $10^6\,\mathrm{particles\,mL^{-1}}$. Similar to the results above, a defined group of particles is trapped at the desired target location in the center of the frame. However, the ratio of particles trapped in this location to those trapped along the wires is strongly increased.

In conclusion, these results can be explained as follows. The permanent activation of a trap at a given position of the array creates a localized maximum in field strength, that attracts particles in the vicinity. However, the gradient towards this maximum decreases with distance. Hence, the field distribution at a certain distance from the center is mainly given by the two horizontal or vertical wires. Particles that are trapped along these wires are not transported to the center location for two reasons. On the one hand, the gradient towards the

center at this location is comparably small. On the other hand, the particles' mobility is strongly decreased due to the normal component of the magnetic force. To circumvent this, the second collection protocol does not activate a given set of wires permanently. Instead, the protocol alternatingly concentrates the particles in x- and y-direction. This strongly increases the probability of particles reaching the center position. Using this protocol, lower particle concentrations (approx. $10^3\,\text{particles}\,\text{mL}^{-1}$), and longer collection times (20–30 min), it was possible to collect defined clouds of 10–20 particles without notable amounts of particles in the surrounding. Figure 4.1E shows a defined cloud of monodisperse 1 µm particles (see Table 3.2; MyOne carboxyl) collected with this method.

CLOUD ACTUATION The actuation of particle clouds at the chip's surface can be performed with various switching protocols. These protocols, however, can significantly differ in their transfer efficiencies (i.e. the percentage of particles transferred during each transportation step), as well as the maximum transfer rates. In this context, three protocols were used to relocate particle clouds at the chip's surface. These protocols were then examined in terms of their switching efficiency, as well as the maximum switching rate.

Figure 4.2A shows the simulated magnetic fields for all three protocols. The first protocol, referred to as "direct switching", is shown in the middle path. In this protocol, the trap at the source location is switched off and a trap at the target location is activated in the same instance. The result is an immediate relocation of the peak in the magnetic field as shown in Figure 4.2A. Figures 4.2B-E show an image sequence of a group of approximately 30 particles subjected to this

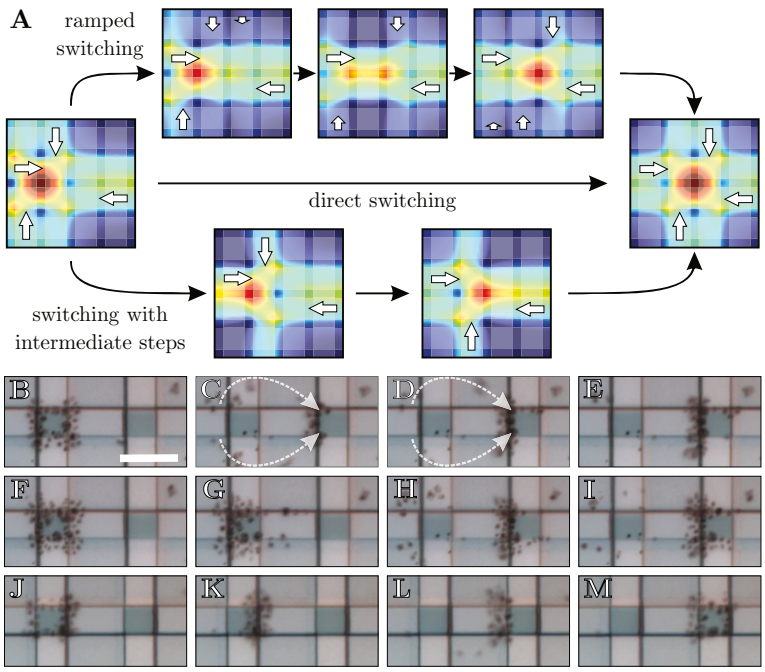

Figure 4.2: Simulated magnetic fields and particle distributions during the different switching protocols. **A:** FEM simulation of the magnetic field at the chip's surface. The wires' location is indicated by the shaded regions. Active wires are marked with white arrows ($I_0 = 100\,\mathrm{mA}$). The upper path shows the field at 25, 50, and 75% switching completion for the linear switching protocol. The arrows are shortened proportionally to indicate currents of 0.25, 0.5, and 0.75 I_0. The color scale for all images is identical with that in Figure 4.1B. **B-E, F-I, and J-M:** Image sequences illustrating the particle distribution during a jump using the direct, linear, and intermediate switching protocol, respectively. The frames are extracted from video sequences at 0, 33, 66, and 100% of the overall jump duration. The scale bar in **B** corresponds to 10 µm and applies to all 12 images.

protocol. The images are frames from a video extracted at 0, 33, 67, and 100% of the total duration of the jump (4 s). In this context, the duration of a jump refers to the time the particles were given before the next jump was executed. As shown in Figure 4.2B, the group of particle is distributed according to the maximum in the magnetic field visible in the left side of Figure 4.2A. At 33% completion, most of the particles are already transferred to the target cell, while some particles at the left of the source cell lag behind (Fig. 4.2C). Their trajectory can be estimated from the plot of the magnetic field in the right of Figure 4.2A. The nearest regions of high field strength for these particles were the 'protrusions' of approximately 7 mT in the corners of the maximum. After reaching these points, the particles followed the gradient in field strength to the actual maximum in the target cell. This trajectory is indicated by the dashed arrows in the upper and lower parts of Figures 4.2C and D. Some particles following the trajectory can be seen in both images. At 100% completion, most of the particles were transferred to the target location.

The second protocol, referred to as "ramped switching", consisted of a linear transition from the source cell's current state to that of the target cell. The top path in Figure 4.2A shows the magnetic fields calculated at 25, 50, and 75% completion of the switching process. Figures 4.2F-I show frames of a video at 0, 33, 66, and 100% (respectively) of the corresponding jump's duration. In agreement with the simulation, the sequence first shows a relocation of the particle distribution to the left of the source cell. Towards the end of the transfer, the particles then follow the curved trajectories described above. As visible in Figure 4.2I, the final distribution of particles is mainly located at the left of the target cell.

The third actuation protocol, referred to as "switching with intermediate steps", made use of two intermediate steps with only three of the wires being active. The corresponding magnetic fields at the chip's surface are displayed in the lower path of Figure 4.2A. The image sequence in Figures 4.2J-M shows frames of a corresponding video at 0, 33, 66, and 100% of the total duration of the jump. In agreement with the simulated fields, switching off the left wire of the source cell results in a relocation of the particles to the right of this cell. In the next step, inverting the current in the wire in between the source and the target cell shifts the maximum in the field to the left side of the target cell. In contrast to the protocols described above, the gradient acting on the particles in this instance directly leads to the target location. Finally, the last step activates the current in the fourth wire of the target cell thus completing the transfer procedure. Figure 4.2M shows the particle distribution at this point.

In order to compare the efficiency of all three protocols, sequences of several jumps of the corresponding protocol were applied. The duration of a complete jump (i.e. the time from the start of one jump to the start of the next) was varied to evaluate the corresponding maximum switching rate. Furthermore, the transfer efficiencies (i.e. the percentage of particles that was successfully transferred to the target cell) were evaluated by counting the number of particles before and after each jump. The transfer efficiencies measured for the direct and linear switching protocols were in the range of 70% at a jump duration of 4 s. Using the intermediate switching protocol, however, transfer rates of more than 97% were possible at faster switching rates of 2 s per jump.

In summary, neither the transfer efficiency nor the maximum switching rate differed notably between the direct and the linear protocol. An explanation for this can be found in the corresponding image sequences in Figures 4.2B-E and F-I. In both cases mainly the particles on the right side of the source location were transferred during the beginning of the jump. The remaining particles followed a curved trajectory the beginning of which exhibits only weak gradients (compare Fig. 4.2A top and middle path). In addition, the majority of particles was located at the left of the target location after the completion of the jump. In a series of consecutive jumps, more and more particles will thus lag behind or get lost. In combination, these effects lead to a significant decrease of the transfer efficiency, and ultimately failure of the transfer, at elevated switching rates. In contrast to this, the intermediate switching protocol transferred the complete group of particles. After completing the jump, the particles were also distributed notably more homogeneous through the target cell (compare Fig. 4.2M). Both of these points ensure the high transfer efficiencies and switching rates possible with this protocol.

In order to further test the intermediate switching protocol, as well as other typical operations in particle handling, denser particle clouds were collected. Figures 4.3A-D show an image sequence of a particle cloud of an estimated 80 particles being transported via the intermediate switching protocol (switching rate: 0.5 Hz). Even for this denser particle cloud, all of the particles are successfully transferred to the target location. Apart from the relocation of particle clouds, other "unit operations" of particle handling were also investigated. Figures 4.3E and F show the particle cloud from Figures 4.3A-D being separated into two smaller clouds. As illustrated by the current

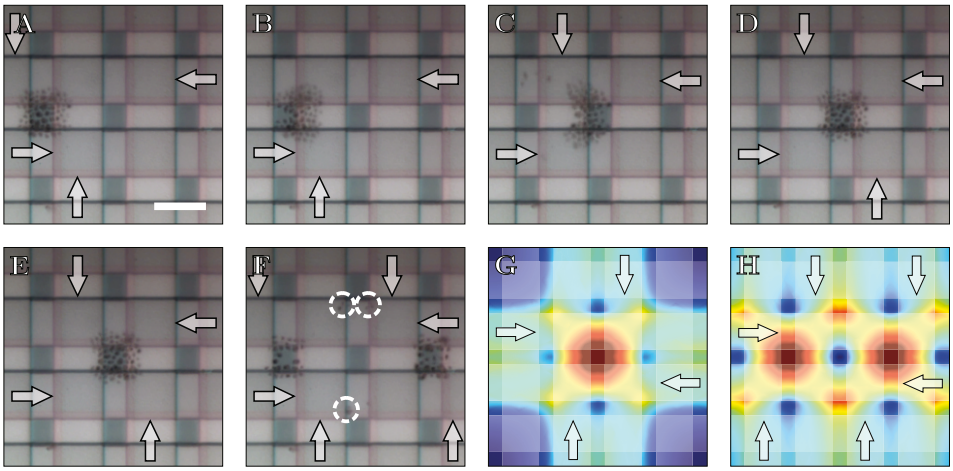

FIGURE 4.3: Image sequence of the transfer and splitting of denser particle clouds. **A-D:** A denser particle cloud is transferred from one position in the array to another using the intermediate switching protocol. **E** and **F:** A particle cloud is separated by activating two traps adjacent to the initial location. **G** and **H:** Simulated magnetic field at the chip's surface for **E** and **F**. The scale bar in **A** corresponds to 10 µm and applies to **A-F**. The color scale for **G** and **H** is identical with that in Figure 4.1B.

patterns and the magnetic fields shown in Figures 4.3G and H, this could be achieved by applying the direct switching protocol. Here, two target cells adjacent to the source cell were activated when deactivating the source cell. As can be seen, this effectively splits the cloud into two. However, it has to be noted that some particles are trapped at locations in between the two target cells (see white circles in Fig. 4.3F). Accordingly, the corresponding regions in Figure 4.3H exhibit side maxima in the magnetic field. This can be explained as follows. In contrast to the direct and linear switching protocol, the side maxima of two target locations overlap at this point. As a result, particles can be trapped at these positions without completing their transfer to the

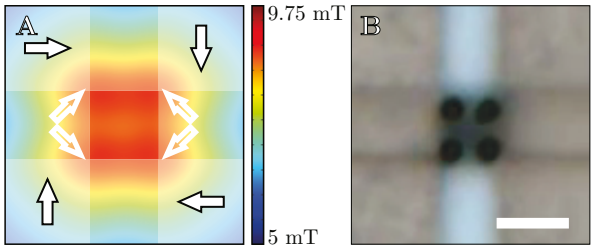

FIGURE 4.4: Simulated magnetic field and particle distribution illustrating the splitting of the peak in the magnetic field. **A:** Enlarged simulation of the central area of an active trap. The shaded regions indicate the edges of the surrounding wires and the filled arrows indicate the current direction ($I_0 = 100\,\text{mA}$). As marked by the empty arrows, the peak is composed of four side maxima. **B:** Particle distribution for a group of four particles. As can be seen, all four particles occupy a different side maxima to minimize the magnetic potential energy. Scale bar: 10 µm.

desired target locations. Reversing this splitting procedure in order to join separate particle clouds can also be performed but is not shown.

During the development of the switching protocols, it could be noted that while otherwise agreeing well with the simulation, the particles mainly collected at the edges of the active trap. In particular, this can be seen in Figure 4.2M. Here, the particles seem to be attracted to the corners of the active trap rather than its center. To further examine this effect, simulations of the center area at a higher resolution, as well as experiments with very small particle numbers, were performed. Figures 4.4A and B show the results of these simulations and experiments, respectively. The enlarged view of an active trap displayed in Figure 4.4A revealed a splitting of the peak in the magnetic field. Instead of a single maximum, the trap was found to actually consist of four side maxima. However, as the difference in magnetic field between these side maxima and the central area of the trap is comparably

small (approx. 0.5 mT), this effect can mainly be seen at low particle numbers. In particular, it can be seen when working with groups of $\leq$4 particles. To illustrate this, Figure 4.4B shows four particles trapped on the array. The location of the particles in this frame clearly coincides with that of the side maxima in Figure 4.4A.

SUMMARY The results presented in this section illustrate the applicability of microwire crossbar arrays to various aspects of on-chip particle handling. The application of chips using similar geometries to the actuation of particle clouds has been introduced by Lee *et al.* [75]. While their approach includes current patterns that were optimized to maintain a Gaussian peak in the magnetic field [76], the methods presented above can be implemented using a simple *on/off* scheme.

In this context, an efficient and simple protocol to collect defined clouds of particles from low concentrated particle suspensions was described. In order to move these clouds from one location in the array to another, different protocols were evaluated in terms of efficiency and switching rate. A switching protocol allowing for a transfer of the particle cloud at efficiencies above 97% and switching rates of 2 s per jump was presented. In addition, splitting and recombination of particle clouds as further "unit operations" of particle handling were demonstrated. In contrast to previous works [75, 76], these operations could be performed without the necessity of differing current magnitudes. From an application point-of-view, this significantly reduces the complexity of the driving circuitry as only current sources of a fixed magnitude are required.

All of the results were in excellent agreement with the accompanying numerical simulations of the magnetic field at the chip's surface. Here,

even minor theoretical variations in field strength could be demonstrated experimentally when using very low ($\leq$4) particle numbers.

4.1.2 ACTUATION AND TRACKING OF INDIVIDUAL MAGNETIC PARTICLES AT THE CHIP'S SURFACE

Among the potential applications of the techniques described above are the mechanical or chemical stimulation of cellular networks. Here, being able to transmit information to individual cells is of great interest. In this context, the use of clouds of particles collected from a suspension bears several disadvantages. For instance, individual particles of the cloud might get lost during transport to the target. In addition, depending on the size of the applied particles, sedimentation might "deliver" particles to non-target cells. In order to circumvent these disadvantages, the actuation of individual particles was examined.

The deployment of individual particles is described in detail in Section 3.2.2. Briefly, a microcapillary was used to deploy a single particle into an active magnetic trap at the chip's surface. This particle was then actuated and, using digital image processing (see Section 3.3.1), its trajectory was extracted. Figures 4.5A-D show an exemplary image sequence from such a single particle experiment. In this experiment, the particle was moved around the crossing of two wires (in the center of the images) using the intermediate switching protocol described above. The circular markers indicate positions at which the particle was detected before, while the arrows indicate the particle's current position. In agreement with the experiments with low particle numbers, a single particle is attracted to the corners of the corresponding traps rather than the center. Figures 4.5E and F show

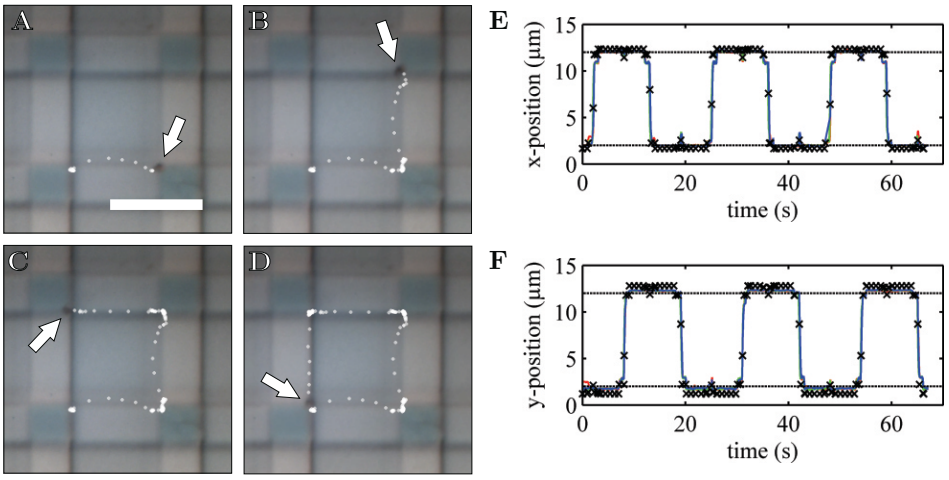

Figure 4.5: Actuation and tracking of an individual particle. **A-D:** Image sequence of a single micrometer-sized particle being actuated at the chip's surface. The particle is marked by white arrows. The circular markers indicate previous position as detected by the MatLab script described in Section 3.3.1. The scale bar in **A** corresponds to 10 µm and applies to **A-D**. **E** and **F:** Comparison of the experimental and the theoretical x-t- and y-t-plots. The red, green, and blue curves show three different measurements. The black crosses indicate positions extracted from an analytical simulation of the system. Figure reprinted with permission from [115]

plots of the x- and y-position of three particles versus time, respectively. In this case, the particles lap the corresponding crossing three times. The strong overlap between the three curves demonstrates the excellent reproducibility and precision of the tracking, as well as the actuation.

In addition to the digital tracking of the particle, an analytical simulation of the system was performed as described in Section 3.3.3. In order to compare this simulation to the experiments, an identical switching procedure was simulated. With a given start position, the motion of the particle could then be described as given in Section 3.3.3.

The black crosses in Figures 4.5E and F show the simulated x-t- and y-t-plots. As can be seen, the simulated data matches the experimental data very well.

In the framework of mechanical or chemical stimulation, these results demonstrate the excellent control over the particle. Using a functionalized particle or e.g. a magnetic microcapsule baring a biologically active cargo, it should be possible to guide a defined stimulus to a target cell. As only a single magnetic entity is used, the undesired stimulation of another than the target cell can be ruled out. This is in contrast to work performed in this field so far, where individual particles are captured from a suspension (e.g. [76, 116]). In this case, capturing a single particle relies on the statistical distribution of the particles through the medium. Furthermore, in the case of cargo being delivered to a target cell, unwanted "delivery" by sedimentation cannot be excluded.

In terms of resolution, using the side maxima described above in a controlled way, particle actuation with subcellular resolution should also be feasible. Furthermore, it has to be noted that the resolution that can be achieved only depends on the chip layout. Using smaller wires and a smaller pitch could thus be used to precisely actuate individual magnetic particles with submicrometer resolution.

4.1.3 3-DIMENSIONAL ACTUATION OF INDIVIDUAL MAGNETIC PARTICLES

The previous section demonstrated the 2-dimensional actuation and tracking of an individual microparticle. While agreeing well with the experiment at hand, the accompanying simulation neglected a sur-

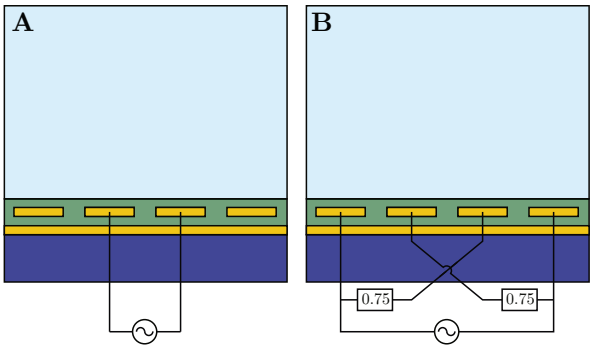

FIGURE 4.6: Cross-sectional schematic of the application of AC signals to the upper layer of wires. **A:** Supplying two wires with signals of AC_{in} and $-AC_{\text{in}}$ will generate an AC voltage between the wires. **B:** Supplying four wires with amplitudes of AC_{in}, $-0.75AC_{\text{in}}$, $0.75AC_{\text{in}}$, and $-AC_{\text{in}}$, respectively, will generate an electric field gradient pointing towards the center of the wires.

face/particle interaction. However, in the case of substrates or particles functionalized with biologically relevant molecules (e.g. proteins), this interaction can easily reach the pN or even nN regime. As these forces are large enough to immobilize the particle at the surface, means of exerting an out-of-plane force to assure the particle's mobility are of interest. In addition, the ability to control the particle/surface contact via 3-dimensional actuation opens many experimental possibilities. By examining the forces necessary to lift the particle off the surface, for instance, an investigation of potential particle/surface binding forces could be performed.

GENERATION OF AC ELECTRIC FIELDS FOR DIELECTROPHORESIS

As the magnetic force always attracts the particle towards the chip's surface, a different force has to be applied in this context. As described in Section 2.2.3, the dielectrophoretic force acts in a repulsive manner

for sufficiently high frequencies. In order to supply the wires with high-frequency AC signals, an external function generator was used (see Section 3.1). As described in Section 3.1, the power supply was able to modify this signal. Effectively, the signal could be multiplied with a factor of 1, 0.75, -0.75, or -1. Figures 4.6A and B show schematics of two possible ways of generating AC electric fields with the amplitude modifications given above. Both figures show cross-sectional views of the chip in a plane normal to the direction of the upper layer of wires. Supplying two neighboring wires with an inverted and a non-inverted signal will effectively lead to an AC voltage as shown in Figure 4.6A. This voltage will yield an electrical field that is strongest close to the chip's surface. Using sufficiently high frequencies (for polystyrene particles in distilled water $> 1\,\mathrm{MHz}$), this results in a force that repels the particle from the surface. However, the electric field generated by this setup also has a strong gradient in a given plane coplanar to the chip's surface. Here, the electric field is strongest at the central position (i.e. the center position between the two wires). The components of the dielectrophoretic force in this plane will thus point away from this location. When applying a combination of magnetic and dielectrophoretic forces, the normal and tangential components of both forces will add up. If the normal component of the dielectrophoretic force exceeds that of the magnetic force, the particle will be lifted off the chip's surface. However, if the tangential components of the dielectrophoretic force also exceed those of the magnetic force, the particle will not remain "trapped" with respect to this plane.

In order circumvent this, the AC signal was applied to four wires as shown in Figure 4.6B. The four wires were supplied with amplitudes corresponding to AC_{in}, $-0.75AC_{\mathrm{in}}$, $0.75AC_{\mathrm{in}}$, and $-AC_{\mathrm{in}}$, respectively.

Similar to the situation of Figure 4.6A, the electric field generated by this setup is strongest at the chip's surface. However, in contrast to the use of two wires, the electric field strength in a given plane coplanar to the chip's surface increases towards the outer wires. This should generate a force that further focuses the particle towards the normal axes in the center of the system.

SIMULATED MAGNETIC AND ELECTRIC FIELDS In order to examine the electric and magnetic fields generated by this setup, a simulation of the system was performed (see Section 3.3.4). Here, an array of 4×4 wires was simulated. The central two wires in both directions were supplied with a current of 10 mA to yield a trap in the center of the array (compare e.g. Fig. 4.3G). In addition, all four wires extending in y-direction (i.e. the upper wires) were supplied with voltages of 20, -15, 15, and -20 V (left to right, respectively). Figure 4.7 shows color plots of the resulting fields. As both, the magnetic and the dielectrophoretic force, scale with the gradient of the squared fields, the plots show the squared magnetic and electric fields. Figures 4.7A and B show x-z- and y-z-views of the squared magnetic field close to the chip's surface (located at $z = 0\,\mu$m. Due to the symmetry of the system, the plots do not differ significantly. However, the field in Figure 4.7B extends further into the solution as the wires in y-direction are closer to the surface. Apart from this, both plots show the highest field strengths in the center of the system close to the chip's surface.

Figures 4.7C and D show plots of the squared electric field. The four wires used in the simulation were supplied with the amplitudes given above. As described above, the squared electric field in the x-z-plane decreases in normal direction (see Fig. 4.7C). In a given plane coplanar

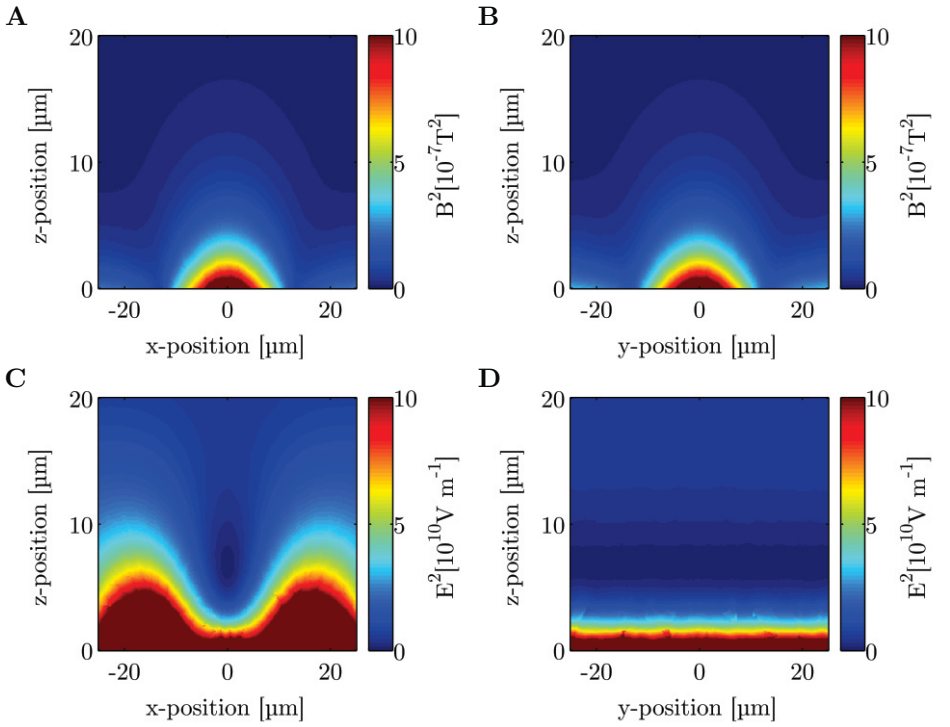

FIGURE 4.7: Color plots of the squared magnetic and electric fields. **A** and **B:** Squared magnetic field in the x-z- and y-z-plane close to the chip's surface (respectively). Apart from differences arising from the z-position of the wires in x- and y-direction, the field distributions are similar. **C** and **D:** The squared electric field is strongest at the chip's surface. In a given plane coplanar to the chip's surface, the field is stronger at the outer edges than in the middle. As the wires used to generate the electric field extend in y-direction, no significant variation of the field distribution with respect to this axis was found.

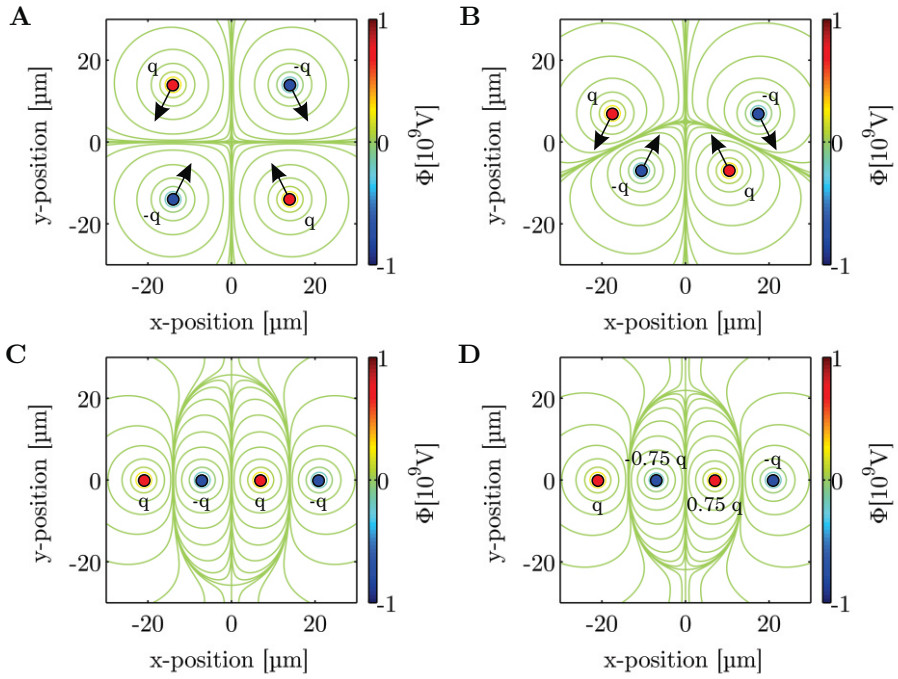

FIGURE 4.8: Equipotential lines for exemplary arrangements of point charges. **A:** In a regular quadrupole, the coordinate axes coincide with zero-potential lines. **B:** When moving the charges towards a linear arrangement (as indicated by the arrows) the horizontal zero-potential line is deformed. **C:** For a completely linear arrangement with equidistant charges of alternating sign but identical magnitude, this zero-potential line is deformed to a closed loop. **D:** Reducing the magnitude of the center charges results in a lower crossing point of the zero-potential lines.

to the chip's surface, however, the field is stronger towards the outer edges. In addition, a local minimum in field strength can be found along the z-axis at a height of approximately 5–6 µm.

In order to explain this effect, Figure 4.8 shows exemplary arrangements of point charges. Figure 4.8A shows the equipotential lines for four charges of $\pm q = \pm 1.602 \times 10^{-9}$ C. The four charges are arranged so that they form an electric quadrupole. Due to the symmetry of the system, the coordinate axes coincide with lines of a potential of zero. At the coordinate origin, these lines meet at a right angle. Consequently, the local gradient of the potential (and thus the electric field at this point) is zero. When distorting the symmetry of the system by moving the charges towards the horizontal axis (as indicated by the arrows in Figs. 4.8A and B), the horizontal zero-potential line is deformed (see Fig. 4.8B). This deformation becomes particularly visible in the case of Figure 4.8C, where the zero-potential line is deformed to a closed loop. In all three cases, however, both of the zero-potential lines meet under a right angle. As discussed above, this leads to a local minimum in the electric field as observable in Figure 4.7C.

Figure 4.8D shows the equipotential lines for a linear arrangement with reduced magnitudes for the center charges (equivalent to the reduced potential applied to the center wires). As can be seen, the minimum in the electric field is lowered by approximately 5 µm. Due to the rectangular cross-section of the wires, as well as the different materials in the system, the equipotential lines shown in Figure 4.8D can only give an approximation of the actual potential distribution. Both of the corresponding zero-potential lines, however, will still meet under a right angle, explaining the local minimum in field strength visible in Figure 4.7C. As the wires generating this field extend along

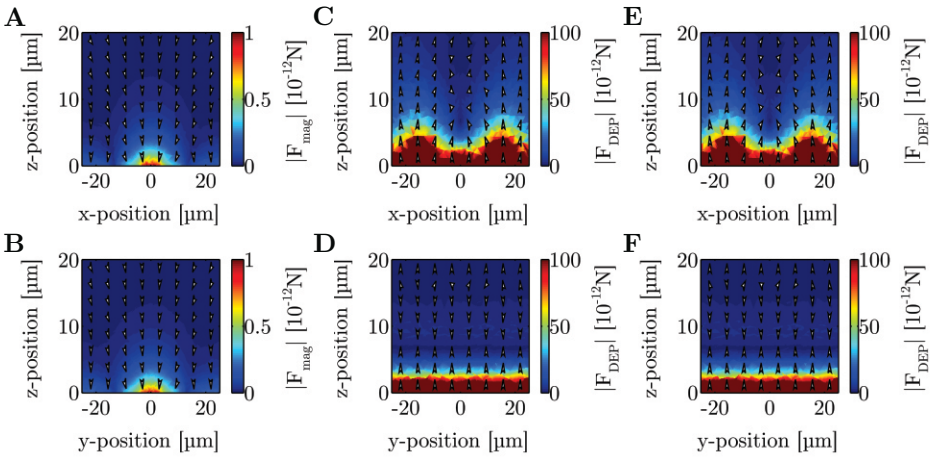

Figure 4.9: Simulated force fields for a 2.7 µm diameter particle. **A** and **B:** Due to the symmetry of the system, the magnetic force fields in the x-z- and y-z-planes are very similar. In both cases, an attraction towards the center of the corresponding plane at the chip's surface can be noted. **C:** The dielectrophoretic force field in the x-z-plane shows an attraction towards the local minimum approximately 5 µm above the surface. **D:** The dielectrophoretic force fields in the y-z-plane is homogeneous along the y-axes. **E** and **F:** For the parameters used in the simulation, $I_0 = 10\,\mathrm{mA}$ and $AC_{\mathrm{in}} = 20\,\mathrm{V}$, the combined force field is dominated by the dielectrophoretic force.

the y-axis, the field depicted in Figure 4.7D does not vary significantly with respect to this axis. The aforementioned local minimum, however, can be seen as a line in this plane.

Simulated magnetophoretic and dielectrophoretic force fields Using the expressions presented in Sections 2.1.4 and 2.2.3, these plots can directly be used to calculate the forces exerted on a particle with given properties. Figure 4.9 shows plots of the corresponding forces on a 2.7 µm particle as listed in Table 3.2. The color plots in

this figure indicate the magnitude of the force on the particle, while the arrows indicate its direction. As can be seen in Figures 4.9A and B, the magnetic force points towards the chip's surface and towards the center of the system in the x-z-, as well as in the y-z-plane.

In the vicinity of the chip's surface, the dielectrophoretic force depicted in Figure 4.9C and D acts repellent on the particle. Also, its x-component points towards the central axes as described above (see Fig. 4.9C). The local minimum in field strength, however, leads to an attraction towards this point in the center region up to a height of approximately 17.5 µm. For farther distances from the surface, the field decay results in a purely repellent force. Figures 4.9E and F show the total force on the particle. As can be seen, for the voltages and currents used in the simulation, the total force field is clearly dominated by the dielectrophoretic force.

In summary, the results of the simulation indicate the following. The activation of a magnetic trap by supplying four wires with current yields an attraction towards the center of the system. Additionally supplying the four upper wires of the system with AC signals results in repellent forces in the vicinity of the chip's surface. At a further distance of approximately 6.5 µm, the electric field distribution exhibits a local minimum. This minimum results in an attractive force towards its location for heights lower than approximately 17.5 µm. As the upper wires used to generate the electric field extend along the y-axis, the field distribution is roughly homogenous with respect to this direction. For the currents and voltages used in this particular simulation, the dielectrophoretic force dominates the combined force field. The overall magnitudes of the forces are in the lower pN regime. This agrees with the analytical simulation used to predict the trajectory of a

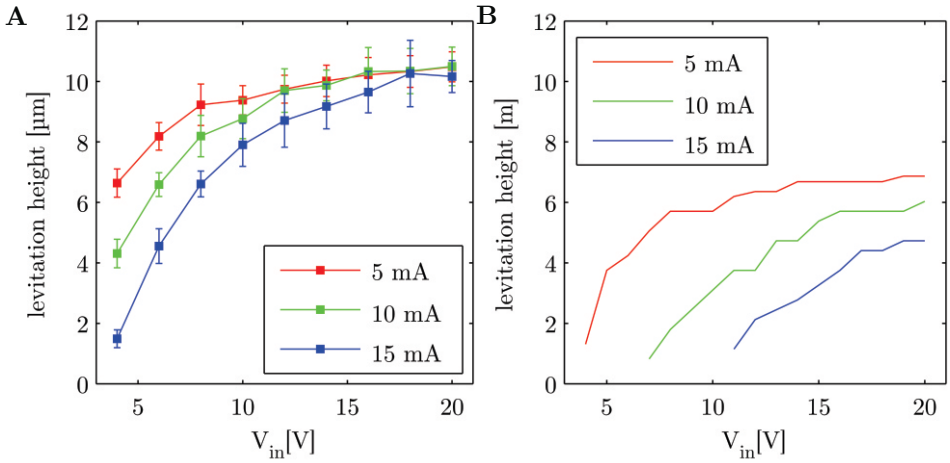

Figure 4.10: Levitation heights of a 2.7 µm particle. **A:** Measured levitation heights for currents of 5, 10, and 15 mA per wire and AC signals of 2–20 V. **B:** Corresponding simulation of the levitation height in dependence of the current per wire and the AC signal's amplitude.

single particle presented in Section 4.1.2. As demonstrated in this context, forces of this magnitude are sufficient to actuate beads of low micrometer dimensions.

Experimental validation In order to validate these results experimentally, measurements of a particle's levitation height in dependence of I_0 and AC_{in} were performed as described in Section 3.2.2. Briefly, the particle was deployed in an active magnetic trap operated at a given value of I_0. Subsequently, the AC signals of varying amplitude were applied and the particles z-position was measured with and without the AC signal using the microscope's z-controller. Figure 4.10A shows the resulting levitation heights for $I_0 = 5$, 10, and 15 mA and AC amplitudes of 2–20 V. All three curves show an increase in the levitation height with increasing amplitude of the AC signal. For a

fixed AC amplitude, however, the levitation height decreases with increasing I_0. This is due to the fact that an increase in the AC signal's amplitude results in higher electric field strengths. These higher field strengths, in turn, result in a stronger dielectrophoretic force. As the dielectrophoretic force repels the particle from the surface, this increase is expressed by a higher equilibrium position of the particle. Vice versa, an increased current per wire will cause higher magnetic field strengths. These will then cause an increase in the magnitude of the magnetic force, which decreases the equilibrium height. In addition, it can be noted that at very high amplitudes, the curves meet at a height of approximately 10 µm. This is due to the dielectrophoretic force dominating at higher AC signals. As described above, the electric field exhibits a local minimum in the x-z-plane which attracts the particle independent of the magnetic force. At higher voltages, the particle's deviation from this point caused by the magnetic attraction becomes negligible.

Using the model described above, this measurement was simulated as follows. The electric and magnetic fields for each value of I_0 and AC amplitudes of 2–20 V were simulated. Subsequently, the z-components of the magnetic and dielectrophoretic force were calculated and added. The z-coordinate corresponding to the minimum of the total force along a vertical line in the center of the system was then plotted versus the current per wire and the AC amplitude as shown in Figure 4.10B. While the plots in Figures 4.10A and B match qualitatively, strong discrepancies in the results have to be noted. With decreasing currents and increasing AC amplitudes, both plots tend towards a fixed height. However, the simulated value of approximately 6 µm differs significantly from the experimental value of 10 µm. Moreover,

the simulated magnetic force has a more pronounced influence on the curves as the levitation height at fixed AC amplitudes decreases much stronger than measured experimentally.

VARIATION OF THE SIMULATION PARAMETERS As described above, Figures 4.10A and B show clear deviations between theory and experiment. However, the theory underlying the corresponding simulations did not involve major simplifications of the physical system. Thus, it was considered most likely that this discrepancy was caused by either a flawed measurement or numerical errors in the parameters used for the simulation. Hence, the experiment and the simulation were tested as follows. To verify the experimental data, several structures of known height (determined by SEM and/or profilometric measurements) were measured using the microscope's z-controller. However, all heights were measured correctly (data not shown).

To verify the simulated data, a 2-dimensional version of the model was used for performance reasons. To this end a cross-section in the x-z-plane (at $y = 0$; compare Figure 3.10B) was modeled. As visible in Figure 4.7D, such a model should give a valid approximation for the electric field as there is no significant dependence of these fields on the y-position. Referring to Figure 3.10B, it can be seen that a cross-section at this position does not include the wires in x-direction. The contribution of these wires to the magnetic force, however, could not be neglected. As the magnetic field in the x-z- and the y-z-plane did not differ significantly (compare Figs. 4.7A and B), the force calculated from the wires in y-direction was doubled to compensate for this.

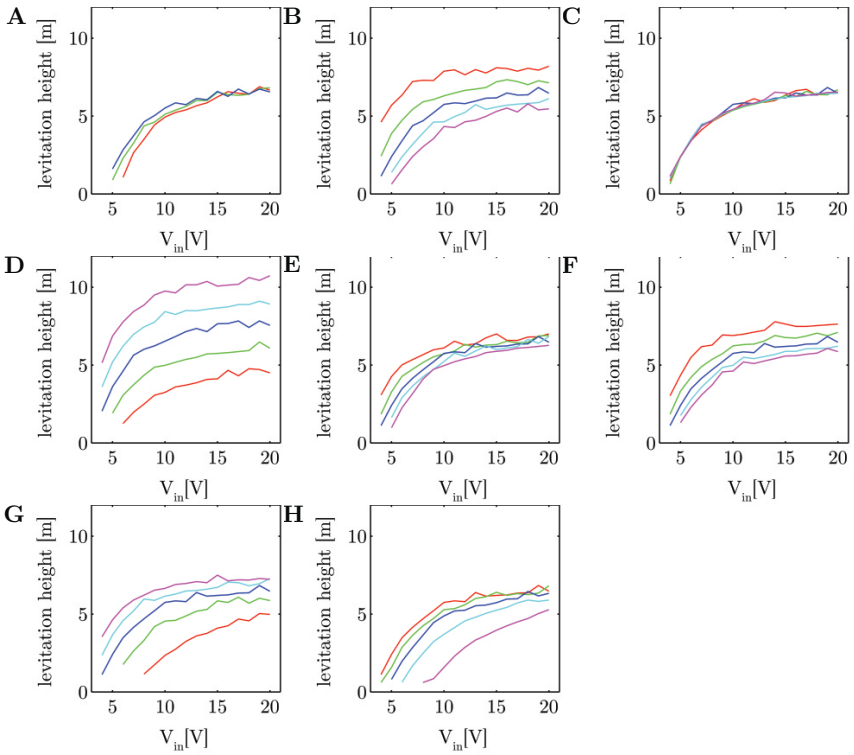

FIGURE 4.11: Simulated levitation height of a 2.7 µm particle plotted against the AC signal's amplitude. All curves are sorted in the order red, green, blue, cyan, and magenta for increasing parameter values. The corresponding values are: **A:** $w_{\text{wire}} = 9$, 9.5, 10, 10.5, and 11 µm; **B:** $h_{\text{PI}} = 0.7$, 1.05, 1.4, 1.75, and 2.1 µm; **C:** $h_{\text{ThOx}} = 0.5$, 0.75, 1, 1.25, and 1.5 µm; **D:** $amp = 0.5$, 0.625, 0.75, 0.875, and 1; **E:** $\chi_{\text{particle}} = 0.7$, 1.05, 1.4, 1.75, and 2.1; **F:** $\varepsilon_{H_2O} = 40$, 60, 80, 100, and 120; **G:** $\varepsilon_{\text{PI}} = 1.7$, 2.55, 3.4, 4.25, and 5.1; **H:** $\text{Re}[f_{\text{CM}}] = -0.5$, -0.4, -0.3, -0.2, and -0.1

In order to test which parameters influence the simulated plots, selected parameters were varied and their influence on the plots was examined. These parameters comprised variables that depended on the chip fabrication (e.g. w_{wire}, h_{PI}, etc.), as well as material constants (e.g. $\varepsilon_{\mathrm{PI}}$, $\varepsilon_{\mathrm{H_2O}}$) and electronic parameters (amp).

VARIATION OF w_{wire} During the experiments, a deviation of the width of the individual wires, w_{wire}, in between different wafers was noted. This deviation was mainly depending on the exact development time of the photoresist during the fabrication of the wires (see Section 3.2.1). Assuming that this deviation could have caused the discrepancy between simulation and experiment, simulations with varying wire widths were performed. Figure 4.11A shows a simulation for wire widths of 9, 9.5, 10, 10.5, and 11 µm (red, green, blue, cyan, and magenta, respectively). Except for the varied parameter, all of the other parameters were kept constant as described in Table 3.3. As can be seen in Figure 4.11A, the width of the wires does not have strong influence on the curves. The levitation height at high AC signals is not influenced by varying this parameter. In the regime of lower AC signals, however, a small effect can be seen. Here, the levitation height decreases with decreasing wire width. This is due to the fact that, in analogy to the experiment, the wires were supplied with a defined current. Decreasing the wires' width thus results in an increased current density in the wire, which increases the strength of the magnetic field. The resulting increase in the magnetic force lowers the equilibrium position as seen in the plot.

VARIATION OF h_{PI} The electrical fields shown in Figures 4.7C and D exhibit a clear dependency on the distance to the wires. The minimum

distance (i.e. $z = 0$, at the chip's surface) is given by the height of the passivation layer, h_{PI}. Furthermore, a step in the dielectric constant from that of polyimide to that of water takes place at this point. As explained in Section 2.2.2, the position of such a boundary has a strong influence on the electric field. Similar to w_{wire}, however, h_{PI} could also have been subject to fabrication-dependent deviations from its nominal value. In order to examine the effect of such variations, a parameter scan similar to the one given above was performed (see Fig. 4.11B). The height of the polyimide was varied from 50 to 150% of the nominal value (i.e. 0.7, 1.05, 1.4, 1.75, and 2.1 µm, shown in red, green, blue, cyan, and magenta, respectively). In contrast to w_{wire}, h_{PI} has a strong influence on the curves. As can be seen in Figure 4.11B, increasing h_{PI} decreases the effective levitation height. In particular, the levitation height at high AC amplitudes is decreased.

Similiar to Figure 4.8, Figure 4.12 shows an arrangement of point charges to explain this effect. The charges have a magnitude of q, $-0.75\,q$, $0.75\,q$, and q ($q = 1.602 \times 10^{-9}$ C; left to right, respectively). They are located at z-positions of -5 and -10 µm (A and B, respectively). Additionally, at $z = 0$ a step in the dielectric constant was implemented. For all points $z < 0$ the dielectric constant is that of polyimide and for $z > 0$ it is equal to that of water. A greater distance of the charges to this step in the dielectric constant corresponds to a greater value for h_{PI}. As can be seen, the crossing of the zero-potential lines effectively lowers for greater values of h_{PI}. However, this effect is rather due to a shift in the reference point. Comparing Figures 4.12A and B, it can also be seen that less equipotential lines penetrate into the region above $z = 0$. This is due to the fact that for a greater distance of the charges from $z = 0$, more field decays up to this point. The

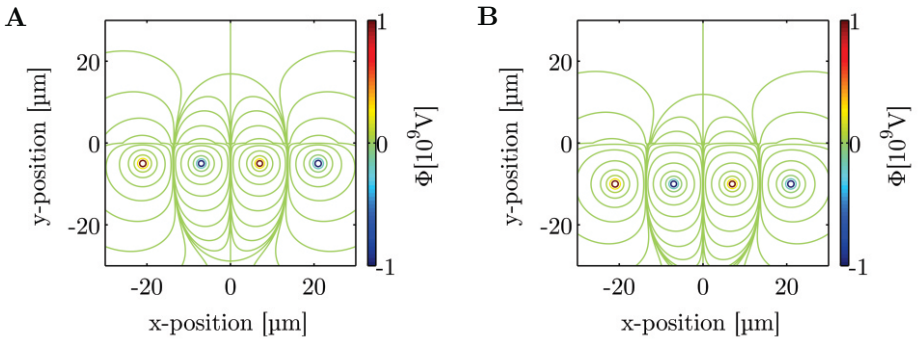

FIGURE 4.12: Equipotential lines for linear quadrupoles in the vicinity of a dielectric boundary. The four charges have a magnitude of q, $-0.75\,q$, $0.75\,q$, and q ($q = 1.602 \times 10^{-9}$ C; left to right, respectively) and are located at z-positions of -5 and -10 µm (**A** and **B**, respectively). A step in the dielectric constant at $z = 0$ from that of polyimide ($z < 0$) to that of water ($z > 0$) was implemented. Due to the shifted reference point in **B**, the equipotential lines are lowered by approximately 5 µm in z-direction. Additionally, less equipotential lines penetrate in the positive z-region indicating a lower field strength.

result of this is that the field strength in the region $z > 0$ is effectively lowered. Referring to Figure 4.11B, this results in lower levitation heights as the dielectrophoretic force is weakened. In particular, this is visible in the range of low AC inputs.

VARIATION OF h_{ThOx} The paragraphs given above demonstrate that the geometry of the dielectric materials surrounding the wires can strongly influence the overall field distribution. As the thickness of the oxide layer on the wafer could also have been subject to fabrication-dependent variations, the influence of this parameter was investigated. To this end, h_{ThOx} was varied from 50 to 150% of its nominal value (i.e. 0.5, 0.75, 1, 1.25, and 1.5 µm). The resulting plots are given in Figure

4.11C (plotted in red, green, blue, cyan, and magenta, respectively). However, as can be seen, this did not influence the curves significantly.

VARIATION OF *amp* Figures 4.8C and D revealed a strong influence of the factor *amp*, which is used to reduce the amplitude of the center wires, on the position of the local field minimum. The electronic design of the driving circuitry was chosen to result in a value of $amp = 0.75$. However, the individual components (i.e. resistors, capacitors, etc.) are subject to variations. Hence, the influence of this parameter on the curves was examined. The plot in Figure 4.11D shows a simulation performed at values of $amp = 0.5$, 0.625, 0.75, 0.875, and 1 (red, green, blue, cyan, and magenta, respectively). As can be seen, this factor has a strong influence on the simulated curves. For increasing values of this factor, the curves are shifted to higher equilibrium heights. Referring to the schematics shown in Figure 4.8, this can be explained as follows. A lower factor than 1 corresponds to lower magnitudes for the center two charges. This would lead to a deformation of the zero-potential line (and correspondingly all other equipotential lines) towards less prolonged shapes as seen in Figures 4.8C and D. As a result, the equilibrium positions are shifted to lower values if the factor is decreased.

VARIATION OF $\chi_{\mathbf{particle}}$ The previous parameter screens were mainly concerned with the electric fields. The discrepancies between theory and experiment, however, could have also been caused by deviations in the magnetic parameters. Here, in particular the magnetic susceptibility, χ_{particle}, used for the simulations could deviate from the actual value. This is due to the fact that the literature values used in the simulation were obtained from measurements in homogeneous fields

[117]. However, the magnetic fields in the present experiments show significant inhomogeneities in the range of the particle's size (see Fig. 4.7). Thus, to investigate the influence of the particle's susceptibility, simulations with varying values for this parameter were performed.

The plot in Figure 4.11E shows a variation of the particle's susceptibility from 50 to 150% of its nominal value (0.7, 1.05, 1.4, 1.75, and 2.1, displayed in red, green, blue, cyan, and magenta, respectively). As can be seen, a variation of this parameter mainly influences the left side of the curves. At high input voltages, the equilibrium height remains unchanged as this region is dominated by the dielectrophoretic force. At low input voltages, the magnetic force has a stronger influence on the curves. Here, an increase in susceptibility corresponds to a higher magnetic moment of the particle. This results in an increased magnetic force and thus decreased equilibrium heights.

VARIATION OF ε_{H_2O} The dielectric constants of water and polyimide have a direct influence on the distribution of the electric field and thus on the dielectrophoretic force. As described in Section 2.2.2, they can influence the sign and the magnitude of the image charges necessary to derive the electric field near the chip's surface. A variation of the dielectric constant of water, ε_{H_2O}, is shown in Figure 4.11F (the curves correspond to values of 40, 60, 80, 100, and 120, red, green, blue, cyan, and magenta, respectively). As described in Section 2.2.2, a higher dielectric constant for water decreases the field strength in this domain and renders the angle between the tangents of the equipotential lines crossing the chip's surface larger. Both of these effects result in lower values for the levitation height at a given AC amplitude, as can be seen in Figure 4.11F.

VARIATION OF $\varepsilon_{\mathrm{PI}}$ Similar to the dielectric constant of water, a variation of the dielectric constant of polyimide, $\varepsilon_{\mathrm{PI}}$, also influences the plots (see Fig. 4.11G). The curves depicted in this plot were calculated for values of $\varepsilon_{\mathrm{PI}} = 1.7, 2.55, 3.4, 4.25, and 5.1$ (red, green, blue, cyan, and magenta, respectively). As discussed above, this parameter influences the field distribution on both sides of the chip's surface. However, in contrast to the variation of the dielectric constant of water, higher values for the dielectric constant of the polyimide yield higher levitation heights. This is due to the fact, that a higher dielectric constant leads to a higher field strength in the polyimide. As discussed in the case of the variation of the polyimide's thickness, this results in a higher field strength in the medium as well. The higher field strength in the medium, in turn, generates a stronger dielectrophoretic force, which gives larger levitation heights.

VARIATION OF $\mathrm{Re}\,[f_{\mathrm{CM}}]$ The last parameter that was varied is the real part of the Clausius-Mosotti function, $\mathrm{Re}\,[f_{\mathrm{CM}}]$. Figure 4.11H shows the corresponding plots for values of $\mathrm{Re}\,[f_{\mathrm{CM}}]$ of -0.5, -0.4, -0.3, -0.2, and -0.1 (displayed in red, green, blue, cyan, and magenta, respectively). As described in Section 2.2.3, $\mathrm{Re}\,[f_{\mathrm{CM}}]$ influences the dielectrophoretic force linearly. As such, lower values of $\mathrm{Re}\,[f_{\mathrm{CM}}]$ yield generally lower levitation heights. For very small values of $\mathrm{Re}\,[f_{\mathrm{CM}}]$, the final levitation height is not reached even for high AC amplitudes.

SUMMARY OF THE PARAMETER STUDY In summary, the study described above revealed the following parameters to significantly influence the levitation heights of the particle. Firstly, the height of the polyimide passivation is of great importance. This parameter is among those that directly influence the electric field distribution and

thus influences the curves strongly. Secondly, the factor applied to decrease the central wires' amplitude has a strong influence on the curves. As with the height of the polyimide layer, this parameter has a direct influence on the electric field distribution and can thus influence the levitation height at low and high AC input amplitudes. Similarly, the dielectric constants of water and polyimide, as well as $\mathrm{Re}\,[f_{\mathrm{CM}}]$, influence the complete range of the curves. The width of the wire, the thickness of the thermal oxide on the wafer, and the susceptibility of the particle were found to be of small or no influence on the described measurement.

After identifying the main parameters influencing the plots in Figure 4.11, their nominal values were checked by either performing a direct measurement or examining possible reasons for variations. Figure 4.13 shows scanning electron microscopy (SEM) images of a chip that was cut using a focussed ion beam (FIB). Figures 4.13A and B show cuts in the x-z-plane, while Figures 4.13C and D display cuts in the y-z-plane. In particular in Figures 4.13A and C, the height of the polyimide layer can be measured. The value extracted from these images amounts to approximately 1.4 µm, which is in good agreement with its nominal value according to the fabrication details. In addition, the plot in Figure 4.11B indicates that values of $\leq$0.7 µm would be necessary to explain the levitation height of 10 µm measured at high AC input voltages.

As mentioned above, the factor applied to decrease the center wires' amplitude can vary due to variations in the exact values of the electronic components. In order to validate this value, an oscilloscope was used to measure the AC amplitudes at the wires' contacts. In this measurement, two effects were found. On the one hand, the amplitudes measured

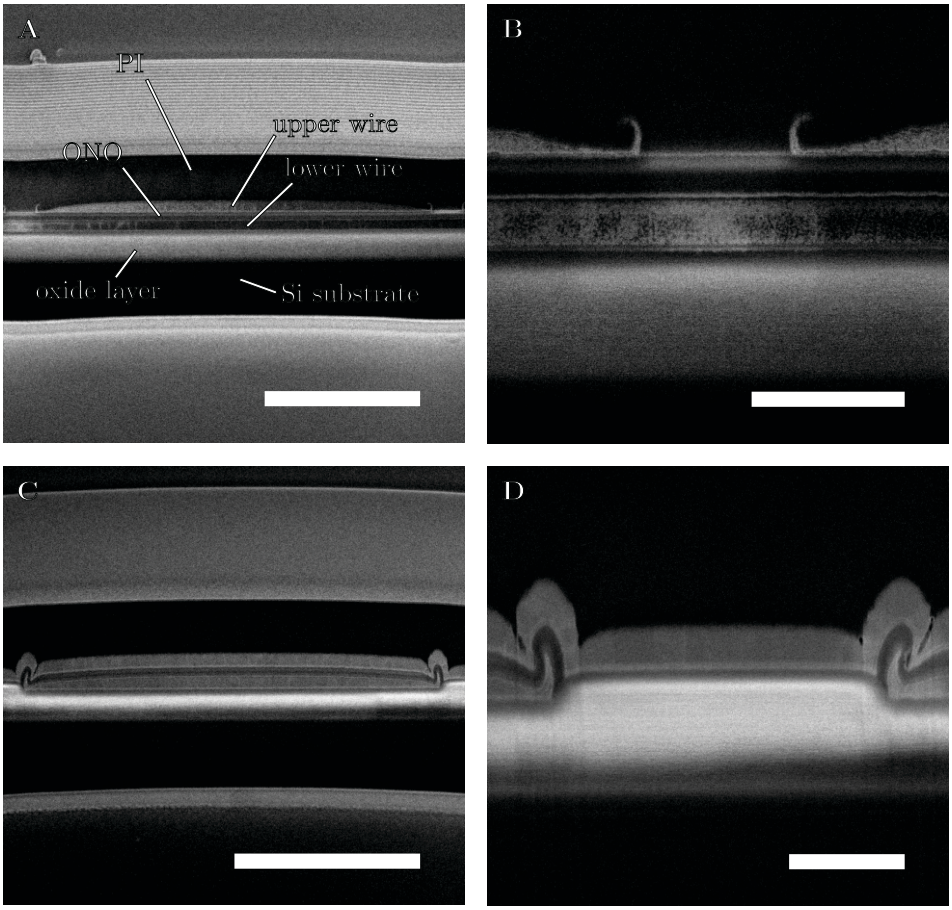

FIGURE 4.13: Angle-corrected SEM images of a chip cut via FIB. **A** and **C:** Images of the complete cross-section of a wire in the upper and lower layer of wires, respectively. The individual parts of the chip are labeled in **A**. Scale bars: 5 µm. **B** and **D:** Close-up images of the interwire region in the upper and lower wire layer, respectively. Scale bars: 1 µm.

at the contacts were approximately 5% higher than the input voltage. This was due to an internal amplification in the power supply necessary to compensate losses of the input signal when being passed through the power supply. When comparing the center wires' amplitude to that of the outer wires, a ratio of 0.66 instead of 0.75 was found. As shown in Figure 4.11D, this should have a strong influence on the simulated heights. This measurement, however, neglects the potential drop between the wires' contacts and the center due to the impedance of the wires. Thus, the measurement was repeated with only one end of each wire contacted to the power supply. Probing the amplitudes at the other end of the wires yielded similar results to those given above. The decreased value for *amp* of 0.66 was used in all following simulations.

The dielectric constants of both, the polyimide and water, are dependent on different experimental parameters. In the case of water, the dielectric constant is influenced by the ion concentration and depends on the frequency of the electric field. For the former, however, concentrations higher than 0.5 M are necessary to change the value of the dielectric constant by 10% [118]. As distilled water was used in the experiments, possible ion contamination sources can be reduced to the chip itself, the microscope, or gaseous contaminations from the ambient atmosphere. However, none of these could cause contaminations in the molar range. Similarly, the frequencies at which significant changes in the dieletric constant of water can be noted lie in the GHz regime. As the frequency used in the experiments was 2 MHz, contributions from this effect are also highly unlikely.

For the polyimide, varying moisture content in the layer as well as surface roughness could be factors influencing the effective dielectric

constant of the layer. Being an important material class in the electronic industry, the dielectric properties of various polyimides have been examined thoroughly. Mercer and Goodman [119], for instance, have measured the dielectric properties of several polyimides under various conditions. Their findings indicate that, while depending on the exact polyimide and the experimental conditions, most polyimides have a dielectric constant in the range of 2.5–3.5 [119]. The plot in Figure 4.11G, however, indicates that values much higher than 5 would be necessary to explain the maximum levitation heights shown in Figure 4.10A.

Another parameter that influences the curves in Figure 4.11 is the real part of the Clausius-Mosotti function, $\mathrm{Re}\,[f_{\mathrm{CM}}]$. This parameter depends on various properties of the particle and the surrounding medium and was not accessible. However, for increasing frequencies and $\varepsilon_{\mathrm{m}} \gg \varepsilon_{\mathrm{p}}$, it converges towards -0.5. As can be seen from Figure 4.11H, decreasing the value of $\mathrm{Re}\,[f_{\mathrm{CM}}]$ would only increase the discrepancy between the simulated and experimental curves.

Apart from these parameters, the FIB cuts displayed in Figure 4.13 revealed another potential reason for the deviations. As described in Section 3.3.4, the wires were modeled using a rectangular cross-section. In particular Figures 4.11A and C, however, revealed relatively strong deviations from this geometry. As can be seen in these plots, the edges of the wires were subject to a fabrication artifact. Both edges shows protrusions in the normal direction of the chip plane. These artifacts result from edge deposition during the sputter process. Originally, the metal deposition was performed using an electron beam evaporation. This evaporation method offers higher anisotropy and is thus less prone to such artifacts. Due to quality issues in this deposition

process, however, the resistivity of the resulting metal layers increased significantly. The fabrication of the remaining wafers was performed using sputter deposited metal layers. Remodelling the geometry of the chip with a wire cross-section more similar to that visible in Figure 4.13, however, did not have a significant influence on the levitation heights.

The above described results showed that all parameters that significantly influence the curves in Figure 4.11, are parameters that influence the electric field distribution around the wires. The lower layer of wires, however, that was not used in the experiment was not assigned a defined potential in the simulation. In the case of the 2-dimensional simulations that yielded the plots in Figure 4.11, these wires were not included at all since the results in the case of the 3-dimensional situation did not indicate a significant change in the electric field with regard to the y-axis. Since all of the above given parameters could not explain the deviations described above, a potential contribution of the lower set of wires was examined. For performance and comparability reasons, this set was included in the 2-dimensional model as follows. A metal layer of rectangular cross-section above the oxide layer was included in the model. Furthermore, since the power supply kept all inactive wires at a relative potential of 0, this layer was assigned a corresponding potential in the simulation as well.

Figure 4.14 shows a plot corresponding to those in Figure 4.10 with the parameters changed as described in the previous paragraphs. As can be seen, the levitation height at higher AC input voltages is increased to approximately 7–8 µm by including the lower set of wires. It has to be noted that this simulation was also performed with a corrected *amp* factor of 0.66. Which, compared to the previous value of 0.75,

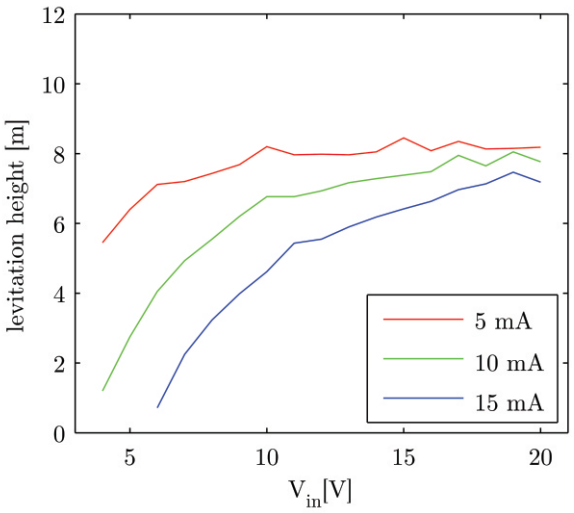

FIGURE 4.14: Simulated levitation heights in dependence of the AC input amplitude and the current per wire. The implementation of a lower wire yields elevated levitation heights even despite a reduced *amp* factor of 0.66.

should cause a significant decrease of this height. However, while the general shape of the curves matches their experimental equivalents in Figure 4.10A quite well, the absolute values over the complete range of input voltages remain too low.

In conclusion, it can be stated that the simulation described the behavior of the particle well on a semi-quantative level. While the general tendencies of each of the parameters' influence could be predicted well, the numerical values extracted from the simulation did not match the experiment. This could be due to several factors. The force on the particle, for instance, was only evaluated along a line in the center of the system. This would only be a correct approximation if the particle can be assumed to be point-shaped. However, the particle's

size is not negligible in comparison to the dimensions of the relevant field gradients. Integrating the force on the particle over the particle's volume could thus give a closer approximation of the overall force.

PARTICLE ACTUATION DURING LEVITATION While not delivering quantitatively correct results, the simulation described the qualitative behavior of the particle well. As such, it could be used to develop a switching protocol to move the particle at a given distance from the surface. Contrary to the 2-dimensional actuation of particles at the chip's surface, the protocols for horizontal and vertical movement during levitation are different. This is due to the fact that, unlike the corresponding magnetic fields, the electrical fields in the x-z- and y-z-plane differ significantly (compare Fig. 4.7). Consequently, the movement in both of these planes has to be treated separately.

Moving the particle along the y-axis (i.e. along the upper wires) does not require a change in the electrical field as it can be considered constant with respect to the corresponding axes. Thus, the intermediate switching protocol in combination with a constant application of the AC configuration described above was tested. Switching off one of the horizontal wires in the first step of the intermediate switching protocol shifted the particle to the opposite direction. However, the decreased magnetic force on the particle also influenced its levitation height. In order to compensate for this effect, the currents in the remaining wires had to be increased by approximately 17%. In this way, it was possible to shift the particle along the y-axis without notably influencing its z-position. Concluding the protocol with increased currents during all states using only 3 wires allowed for a successful transfer of the particle between two positions along the y-axis.

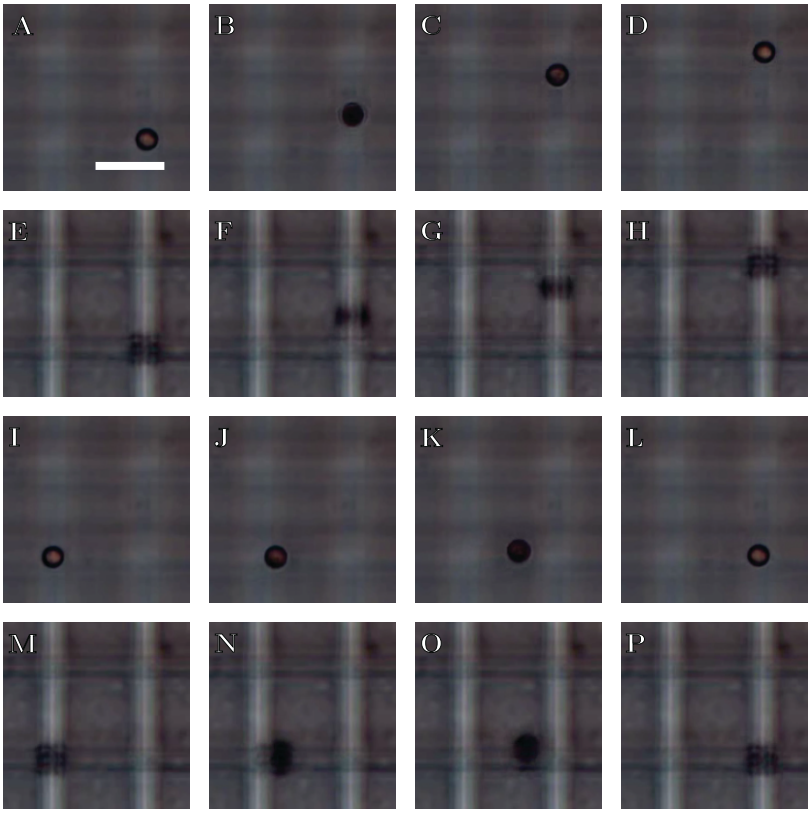

FIGURE 4.15: 3-dimensional actuation of a 2.7 µm particle. **A-D:** Image sequence of a particle being moved in the vertical direction. The video was recorded at the particle's levitation height. **E-H:** Equivalent frames taken from a video recorded at the chip's surface. **I-L:** Image sequence of a particle being moved in the horizontal direction. The video was recorded at the particle's levitation height. **M-P:** Equivalent frames taken from a video recorded at the chip's surface. Scale bar in **A** corresponds to 10 µm and applies to all images.

Figures 4.15A-H depict frames from video sequences of a 2.7 µm particle being moved in this way. Figures 4.15A-D were taken from a video recorded at the particle's initial z-position. Figures 4.15E-H were taken from a video recorded at the chip's surface (i.e. the particle's position before activating the AC signal) at equivalent time points. As can be seen in Figures 4.15A-D, the particle can be moved without notably influencing its z-position. Figures 4.15E-H further demonstrate this as the particle can not be seen clearly at the chip's surface.

In the case of switching along the x-axis, however, the AC configuration had to be changed for the following reason. In between the second and the third step of the intermediate switching protocol, the wires used to generate the dielectrophoretic force field had to be shifted about one wire in the direction of the switching. At this point, however, it was not possible to maintain control over the particle. Simulating the appropriate field configurations revealed the reason for this problem. Similar to the loss of particles during the development of efficient switching protocols in two dimensions, the gradient did not attract the particle towards the desired location. Instead, its trajectory was directed out of the focal plane. Simulating the corresponding fields, configurations that yielded a stable trap over the wire in between the source and target location were developed. It could be shown that applying amplitudes of AC_{in}, $-0.75AC_{\mathrm{in}}$, $0.75AC_{\mathrm{in}}$, $-0.75AC_{\mathrm{in}}$, and AC_{in} to five parallel wires could be used to generate a dielectrophoretic trap over the center wire. Using this AC configuration during the second and third step of the intermediate switching protocol, the particle could successfully be transferred between two positions along the x-axis. As with the vertical transfer, the currents were increased during all steps using only three wires for the magnetic component of the

force. However, due to the increased electric field strengths caused by the additional wire, an increase of approximately 30% was necessary to keep the particle in the focal plane during the switching process.

Figures 4.15I-L show frames of a particle being moved in the x-direction. Similar to the movement of the particle along the y-axis, Figures 4.15M-P show equivalent frames of a video recorded at the chip's surface. As in the case of Figures 4.15A-H, the variations in the particle's z-position are negligible and the particle cannot be seen clearly at the chip's surface.

SUMMARY The results presented above show the following. Using microwire crossbar arrays and a combination of magnetic and dielectrophoretic force fields allows for the 3-dimensional actuation of magnetic microparticles. While examples of combined magnetophoresis and dielectrophoresis have been reported before [120], this is, to the best of my knowledge, the first presentation of full 3-dimensional control over a particle. Additionally, the presented system does not require external magnets to enhance the particle's magnetic moment. Compared to the widely used approaches of meandering wires or coils (e.g. [120, 121]), the fabrication of the microwire arrays is less complex as no vias are needed.

Although using only in plane actuators, the particles can be levitated several micrometers off the chip's surface and can be moved along both, the horizontal and the vertical, directions of the array. Accompanying FEM simulations can be used to describe or predict the particles movement. Despite quantitative deviations, the simulations agreed qualitatively well with the particle movement observed in the experiments. As such, they could be used to develop new actuation

protocols allowing for more than the presented actuation operations (e.g. diagonal movement).

4.2 THERMAL INTRODUCTION OF MICROSCOPIC LESIONS INTO CELL NETWORKS

4.2.1 TEMPERATURE DEPENDENCE OF Ca^{2+} WAVES AND SINGLE-SITE LESION IN CARDIOMYOCYTE CULTURES

The results given above demonstrate that, using microwire crossbar arrays, magnetic particles can be actuated with sufficient precision to deliver chemical or mechanical stimuli with subcellular resolution. Apart from the use of these chips in the delivery of chemical and mechanical cues, the present thesis is also concerned with a third type of cellular stimulation. As described in Section 2.3.1, a current-driven conductor generates heat. In the case of micrometer-sized conductors, this can give rise to strongly localized temperature distributions. In this context, the application of microwire crossbar arrays to the precise thermal stimulation of cells cultured on the chips was examined. In particular, the application of stimuli of high thermal energy and the resulting introduction of lesions in the cell layer were investigated. To this end, HL-1 cells were cultured on the chips and subjected to thermal stimuli. In order to analyze the cell layer's response, Ca^{2+} imaging combined with subsequent frequency and propagation analysis was performed.

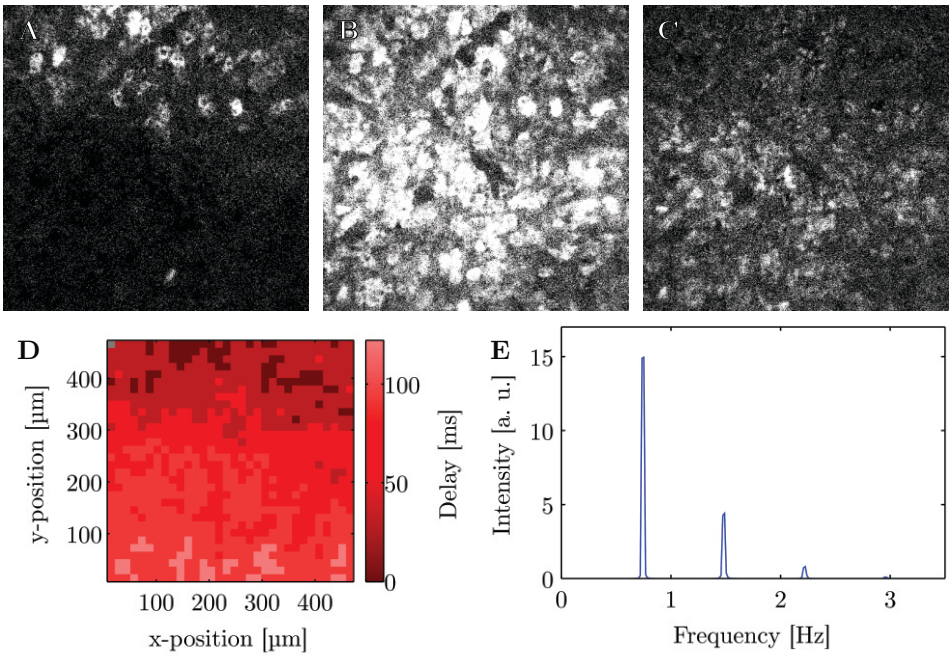

FIGURE 4.16: Ca^{2+} propagation in a layer of HL-1 cells cultured on the microwire crossbar array. **A-C:** Image sequence at relative time points of approximately 0, 150, and 350 ms, respectively. **D:** Correlogram obtained by a cross-correlation analysis of the data. A gradient in the delay visualizing the propagation can be seen. **E:** The sample's PSD can be used to analyse the frequency of the activity, as well as the temporal width of an average Ca^{2+} peak.

TEMPERATURE DEPENDENCE OF Ca^{2+} ACTIVITY The first experiment performed in this context was the application of stimuli of varying electrical power in order to examine the cell layer's response (see Section 3.2.4). Figure 4.16 shows typical Ca^{2+} data obtained from a sample before introducing any thermal stimulus. As described in Section 2.5.1, HL-1 cells generate periodic action potentials and accompanying Ca^{2+} waves when grown to confluence. Figures 4.16A-C show frames from a Ca^{2+} imaging sequence that demonstrate the propagation of these Ca^{2+} waves. The images correspond to relative time points of 0, 150, and 350 ms (A-C, respectively; the microwire array occupies approximately one third of the frame along the x- and y-axes and is located in the center of the frame). The increased intensity visible in the top right corner of Figure 4.16A indicates an increased Ca^{2+} concentration in the cells in this area (compare Section 3.3.2). This peak in the intensity then propagates through the frame (Figs. 4.16A-C). Using a cross-correlation analysis (see Section 3.3.2), this propagation can be displayed in a correlogram as shown in Figure 4.16D. Comparing Figures 4.16A-C and D, a propagation of the signal from top to bottom under a small angle can be seen.

As mentioned above, frequency analyses were performed in addition to the propagation analysis. Here, the power spectral density (PSD) of the Ca^{2+} intensity traces was calculated and analyzed. Furthermore, the interspike interval (i.e. the time between two adjacent peaks in the intensity) and its standard deviation were examined. Figure 4.16E shows the PSD of the average intensity trace of all pixels of the video shown in Figure 4.16A-C. The general characteristics of this spectrum can be explained as follows. As a first approximation, the Ca^{2+} signal in the cell layer is assumed to be periodic. The shape of

each peak is determined by various factors, such as, for instance, Ca^{2+} release kinetics in the cell or the binding kinetics of the Ca^{2+} ions to the dye. As most of these processes do not change significantly in between individual peaks, the shape of each peak can be assumed to be identical. The overall signal can thus mathematically be described as a convolution of a comb function with the shape of a single standard peak. Using fundamental principles of Fourier mathematics, the PSD of such a signal can be predicted. The frequency spectrum of a signal comprised of two convoluted functions is given by the product of their Fourier transforms. As the Fourier transform of a comb function is a comb function, the spectrum exhibits multiple peaks at regular distances. The distance of these peaks is given by $\frac{1}{\Delta t}$, where Δt is the time difference between two peaks. Hence, the distance between two peaks corresponds to the frequency of the original signal. However, the individual peaks in the PSD exhibit a decreasing intensity. This is due to the aforementioned multiplication with the Fourier transform of the peak's shape. As a simple approximation, this shape can be assumed to be Gaussian. The Fourier transform of a Gaussian, however, is a Gaussian. The width of this Gaussian scales with $\frac{1}{T}$, where T is the temporal width of the original peak. This effect explains why only some of the peaks of the expected comb function are visible in the spectrum in Figure 4.16E. Furthermore, the width of an individual peak can be estimated to be $\approx$400 ms, which is in good agreement with the image sequence shown in Figures 4.16A-C.

Using the analyses described above, the response of the cell layer to stimuli of increasing electrical power was examined as described in Section 3.2.4. Briefly, the samples were subjected to thermal stimuli of 1, 1.5, and 2 W applied to two neighboring horizontal or vertical wires

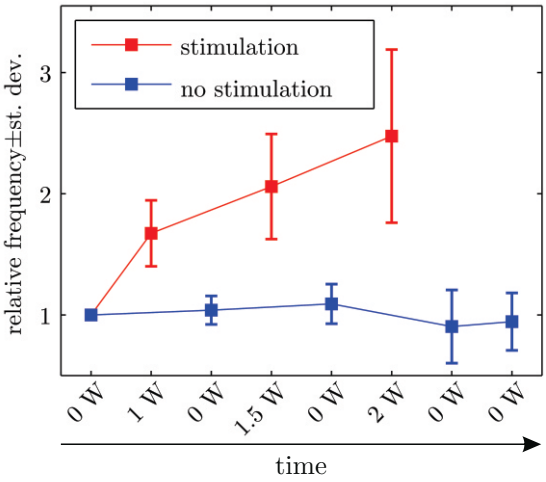

Figure 4.17: Frequency of the Ca^{2+} activity in dependence of the electrical power applied to each of the two wires ($n = 14$). The frequency increases with increasing power. In between the stimuli, however, the frequency returns to its original value.

for 1 min with breaks of 1 min in between the stimuli. Ca^{2+} imaging sequences of 1 min were recorded during all parts of the protocol. In addition, a sequence was recorded after a recovery time of 5 min.

Figure 4.17 shows a plot of the frequency of the cell layer's Ca^{2+} activity versus the electrical power per wire applied to the chip. The plot shows data points taken during stimulation in red, while the remaining data points are displayed in blue. Since the frequency of the individual samples varies depending on the batch of the cell line, as well as other parameters, all measured frequencies are normalized to the sample's frequency in the first video. As can be seen, the frequency of the cell layer's activity depends on the applied electrical power. Moreover, Figure 4.17 shows that the frequency of the cell layer's activity returns to its resting value in between the stimuli.

The results given above demonstrate that microwire arrays can be used to reversibly influence the activity of HL-1 cells cultured on the chips. This effect can be explained by resistive heating of the microwires. This heating results in a temperature increase at the location of the cells. The influence of a temperature increase on cellular processes can be described using an Arrhenius based model [122]. In particular for the HL-1 cells used in these experiments, a temperature dependency of the beating frequency was reported before [123].

THERMALLY INDUCED LESIONS The majority of the samples displayed a change in the Ca^{2+} propagation after the stimuli of higher electrical power. Figure 4.18 displays this change for an exemplary sample. As visible in Figures 4.18A-D, the cells directly above the wires used for the stimulation ceased activity (frames taken at relative time points of 0, 150, 300, and 450 ms, respectively). In combination with the correlogram shown in Figure 4.18E, the following conclusions can be made. In both, the sequence shown in Figures 4.18A-D and the correlogram in Figure 4.18E, the propagation on both sides seems independent. A cross-correlation between the average intensities, however, revealed a correlation of more than 70%. Although the images in Figures 4.18A-D suggest a clear separation between both sides of the wire, the cell layer remained connected due to the layout of the chip. As can be seen in Figure 3.6B, the wires' cross-section expands towards the edges of the chip. As a result, the local electrical resistivity decreases, which lowers the electrical power dissipated at these sites. Consequently, the thermal stress inflicted on the cells at these positions is not as high as in the center of the chip. A schematic of the propagation pattern shown in Figures 4.18A-E is shown in Figure

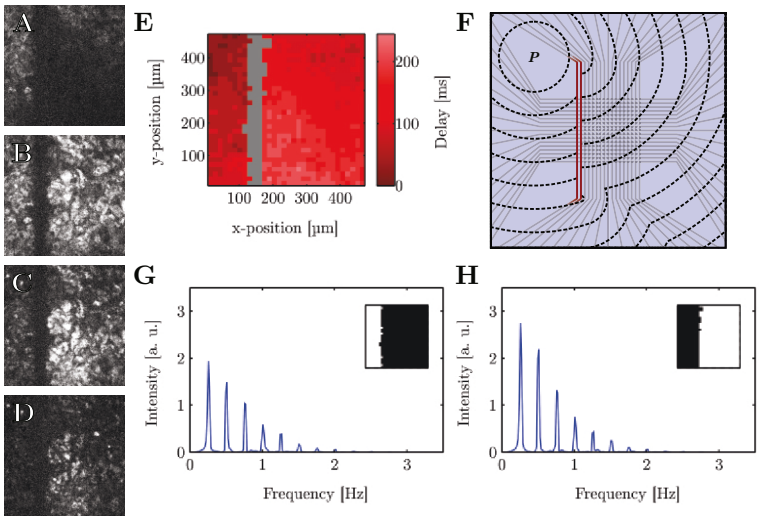

Figure 4.18: Ca^{2+} imaging data of an exemplary sample after high electrical power input. **A-D:** Image sequence taken from the video at relative time points of 0, 150, 300, and 450 ms, respectively. As can be seen, the cells above the wires appear inactive. Furthermore, a phase shift in the activity is visible. **E:** The corresponding correlogram displays a propagation from top to bottom on both sides of the active wires. The activity retains a correlation of $\geq$70% as indicated by the same color. **F:** Schematic of the complete chip explaining the propagation in **A-E**. As the wires widen in the periphery of the actual array, the thermal input at these locations is decreased and a connection is maintained. The signal can thus propagate around the active wires. **G** and **H:** PSDs of the average signal on the left and right side of the active wires, respectively. Both sides exhibit similar frequencies, as well as distances between the peaks. The inlays show a logical mask of the area analyzed to obtain the spectrum.

4.18F. As the lowest delay values in Figure 4.18E were detected in the upper left corner the pacemaker (marked "P" in Fig. 4.18F) had to be located in this direction. Assuming cell death along two vertical wires (displayed as red lines) would effectively interrupt the propagation of the signal across this line. However, as the thermal input is decreased in the periphery of the wires, the signal can propagate around this line. Since in this case both sides are governed by the same pacemaker, their signals show a high correlation. In addition a phase shift (visible by the difference in delay left and right of the line) is introduced. This is supported by the good agreement between both regions' PSDs shown in Figure 4.18G and H. While exhibiting different intensities, the peaks lie at the same frequencies and show the same distances.

LIVE/DEAD STAINING In order to confirm the hypothesis of localized cell death over the heated wires, fluorescent live/dead staining was performed. To this end, the samples were subjected to two stimuli of 2 W per wire applied for 1 min with a break of 1 min in between. Figure 4.19 shows the resulting fluorescence image. The red fluorescence signal corresponds to ethidium homodimer. This dye is not able to permeate the cell membrane and its fluorescence is only visible after intercalation into the desoxyribonulceic acid (DNA) double helix. Cells stained by this dye exhibit a permeated membrane allowing the dye to reach the nucleus. These cells are thus most likely not viable. The green fluorescence signal corresponds to calcein-AM. This dye is functionalized with an acetomethoxy group that facilitates membrane permeation. After entering the cytosol, this acetomethoxy group is cleaved by intracellular esterases. This causes a shift of the flourescence into the displayed regime and renders the dye non-permeant with regard

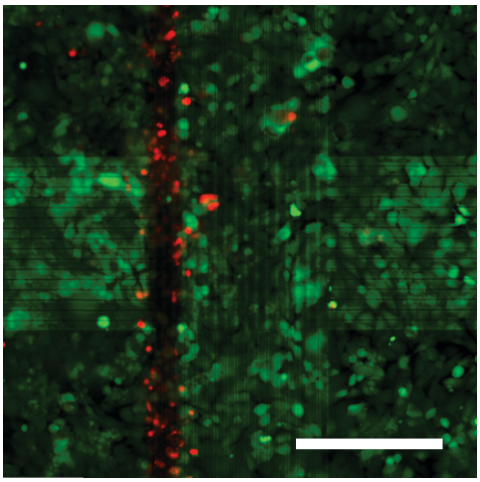

FIGURE 4.19: Live/dead staining of HL-1 cells after lesion along two neighboring vertical wires. The cells were stained with ethidium homodimer (dead, displayed in red) and calcein-AM (live, shown in green). As can be seen, a line of cells directly above the heated wires exhibits cell death. Furthermore it can be seen that the cells in the remaining frame are largely unaffected. Scale bar: 150 µm; frame similar to those shown in Figures 4.16A-D and 4.18A-E.

to the cell membrane. Cells stained by this dye thus exhibit an intact membrane and metabolism, which shows a high likelihood of the cells being viable.

The fluorescent staining shown in Figure 4.19 revealed the following. As indicated above, the cells directly over the heated wire appear dead. The cells in the vicinity, however, remain largely unaffected. These findings are in good agreement with the data analysis of the Ca^{2+} imaging given above. In this context, a line of dead, permeated cells as visible in Figure 4.19 would interrupt the Ca^{2+} signal's propagation as described before.

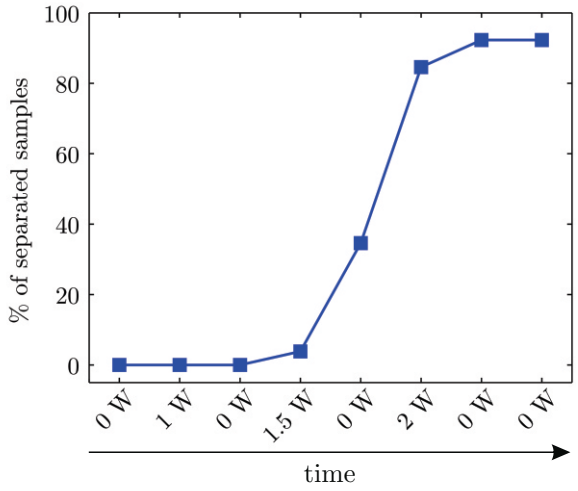

FIGURE 4.20: Cumulated percentage of samples separated at a given point in the experiment ($n = 26$). During or before the application of the 1.5 W stimulus, most samples remain connected. After the 2 W stimulus, more than 90% of the samples showed a clear separation between both sides of the active wires.

The samples were then examined for the thermal input necessary to ensure a successful lesion. Figure 4.20 shows the cumulated percentage of separated samples in dependence of the thermal input in terms of total electrical power applied to the chip. It can be seen, that before and during the application of the 1.5 W stimulus most of the samples do not show separation. After this stimulus, however, a clear increase in the percentage of separated samples can be noted. After applying the 2 W stimulus, more than 90% of the samples displayed clear signs of separation (i.e. a phase shift between both sides or differing propagation directions).

TEMPERATURE MEASUREMENTS In order to examine the temperature distribution that the cells were subjected to, fluorescence lifetime imaging microscopy (FLIM) in combination with FEM simulations was performed (see Sections 3.2.4 and 3.3.5, respectively). Briefly, the experiments were performed as follows. A rhodamine B solution was encapsulated on the chip and the latter was mounted in a confocal laser scanning microscope. The microscope was then focused at the wires and subsequently moved to a plane 5 µm away from this point. Two wires were supplied with an electrical power of 2 W per wire and the fluorescence dye was excited using a pulsed laser. For each pulse, the decay in the emitted fluorescence was measured. Using a calibration curve [105], this lifetime data was converted to temperature data.

Figures 4.21A-D show the temperature profiles at the chip's surface as determined via the experiment and the simulation. The plots exhibit a clearly localized high temperature region over the active wires. In both cases, the simulation and the experiment, the temperature in this region exceeds values of 60 °C. Concerning the remains of the frame, however, the plots differ. The experimental plots show temperatures of approximately 40 °C, while the simulation predicts values of 25 °C. In this context, it has to be noted that the frequency of the Ca^{2+} activity increased homogeneously over the recorded area. This indicates a general temperature increase as suggested by the experimental results. In the case of Figure 4.21B, the influence of the second layer of wires can be seen in the center. In this region, the temperatures are lower due to the good thermal conductivity of the underlying set of wires. The width of the high-temperature region, however, agrees in all plots and amounts to approximately 50 µm. This data is in good agreement with the live/dead staining and the separation of the Ca^{2+} propagation

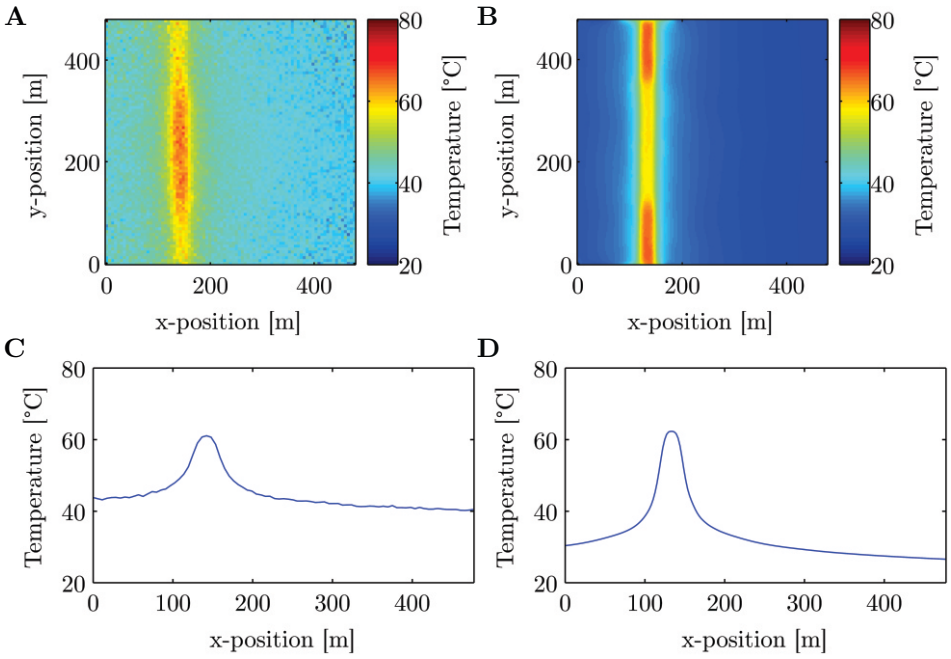

FIGURE 4.21: Thermographs and temperature profiles at the chip's surface as determined experimentally and via FEM simulation of the system. **A** and **C:** Thermograph and temperature profile obtained via FLIM. A localized high-temperature region of up to approximately 65 °C can be seen above the active wires. The remains of the frame show an elevated temperature of approximately 40 °C. **B** and **D:** Thermograph and temperature profile obtained via FEM simulation. The high temperature region of up to approximately 65 °C visible in the experimental plots is confirmed. However, the remains of the frame show temperatures of approximately 23 °C.

presented above. The localized high temperatures of up to 65 °C should be sufficient to induce cell death even if applied for short periods of time [124][1]. The elevated temperatures in the remaining frame in the case of the experimental data should not be sufficient to induce cell death if applied for limited periods of time [124].

In summary, the results described above demonstrate the following. Using resistive heating of selected wires in microwire crossbar arrays, it is possible to induce thermal lesions in cells cultured on the chips. For thermal inputs of low electrical power, an increase in the frequency of the layer's activity was noted as described in the literature [123]. Stimuli of 2 W per wire applied to two neighboring wires could be shown to induce microscopic lesions in the cell layer. As demonstrated by signal analyses of the Ca^{2+} data, these lesions interrupted the communication inside the layer. The reason for this could be shown via fluorescent live/dead staining, which revealed localized cell death for cells growing directly above the heated wires. Cells in the broader vicinity, however, were not affected. This localized cell death was supported by measurements and simulations of the temperature distribution at the chip's surface. The data obtained here revealed localized high temperature zones of up to 65 °C directly above the heated wires. However, concerning the periphery of these zones, the experiment and the simulation did not agree. Data obtained from the further indicated temperatures of approximately 40 °C, while the latter suggested temperatures in the range of 23 °C. As indicated above, however, the homogeneous increase in frequency over the recording area indicates a temperature increase in these regions. Despite this

[1] The data presented here refers to neuronal cells. It can be assumed that the temperature sensitivity of cardiomyocytes is similar.

discrepancy, an agreement with the remaining results was noted since neither of the temperatures should influence the viability of the cells when applied for short periods of time.

4.2.2 DISSECTION OF FUNCTIONAL SUBUNITS OF CELLULAR NETWORKS USING MULTI-SITE LESIONS

The ability to dissect small subunits from a larger cell network could allow the elucidation of several interesting questions. It could be used to, for instance, examine the minimum size of a given cellular network to still fulfill its macroscopic function. Furthermore, the activity in the subnetwork immediately after dissection, as well as during regeneration, could be monitored. Due to the small scale, and thus reduced complexity, basic insights into mechanisms governing, for instance, tissue healing or nerve regeneration might become more accessible.

The previous section introduced the use of microwire crossbar arrays as tools to induce thermal lesions in cellular networks cultured on the chips. As a potential tool for the dissection of functional subunits from a larger network, multi-site lesions were evaluated. In this context, the microwire arrays were used to introduce lesions on several sides of a small square in the network ultimately yielding its decoupling from the remaining cell layer.

LESION AT TWO SIDES The first step towards this goal was the application of lesions at two sites. To this end, two lines of wires were supplied with electrical power as described above. For each line, two

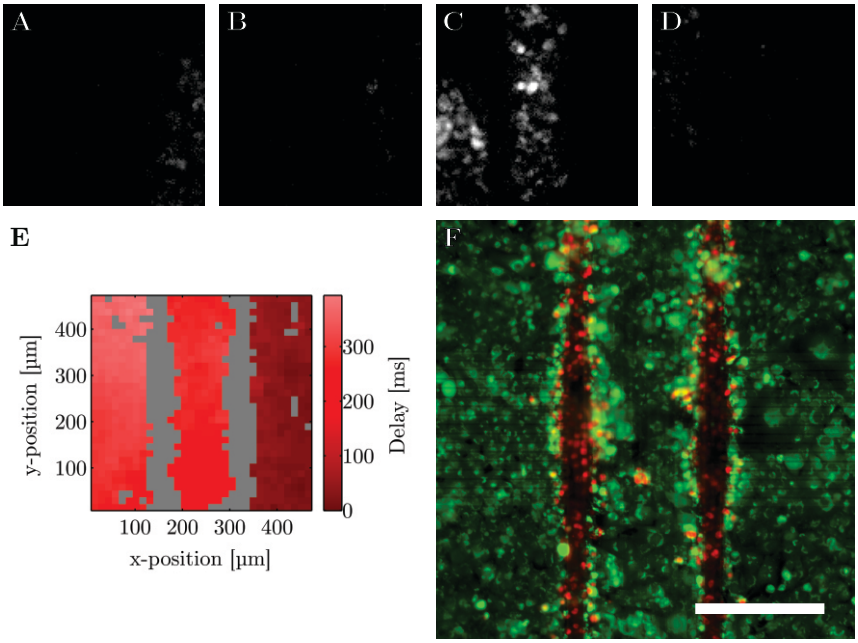

FIGURE 4.22: Ca^{2+} wave propagation in the case of lesion at two sites. **A-D:** Image sequence extracted from a sample subjected to lesion along two vertical lines. The images correspond to relative time points of 0, 165, 330, and 495 ms. The signal originates right of the frame and can thus be seen first in the right third of the frame. After propagating around this set of wires, it reaches the center and right third at similar times due to their proximity at the entrance region. **E:** The corresponding correlogram displays the lowest delay values in the right third. As described above, the center and right third third show similar delay values and a significantly lower phase difference. **F:** Live/dead staining of a sample after subjection to lesions along two vertical lines. As in the case of a single lesion (compare Fig. 4.19), the cell death is restricted to the area directly above the heated wires. Scale bar: 150 µm.

neighboring wires were supplied with 2 W each and activated for 1 min. After a break of 1 min, the second line's wires were activated for 1 min and the procedure was repeated once. Figure 4.22 shows exemplary results of a sample treated in this way. Figures 4.22A-D show an image sequence taken from the Ca^{2+} data. The images were extracted at relative time points of 0, 165, 330, and 495 ms. As can be seen, the Ca^{2+} wave in this sample propagates through the right third of the frame during the first 165 ms. Subsequently, as shown in Figures 4.22C and D, the wave propagates through the middle and the left third. This behavior is expressed in the correlogram in Figure 4.22E. The right third of the plot exhibits the lowest overall delay values. The middle and left third show overlapping delay values with a small phase shift. Referring to Figure 4.18F, this can be explained as follows. Judging from the overall distribution of delay values, the pacemakers has to be located to the right of the frame. The large difference in delay values can be explained by the relatively large distance the signal has to travel in order to reach the lower end of the wires' thin parts (The overall length of the thin part of the wires amounts to roughly 2 mm). The distance between the middle and left third of the frame, however, is comparably small (approximately 200 µm). The phase shift between these two regions is thus rather small.

Figure 4.22F shows a live/dead staining of a sample after subjection to lesion at two sites. The red fluorescence is limited to two vertical lines on top of the heated wires, while the remaining frame exhibits green fluorescence. This indicates that, as in the case of a single lesion (compare Fig. 4.19), the cell death is restricted to regions directly above the heated wires. The cells in the broader vicinity, however, remain viable.

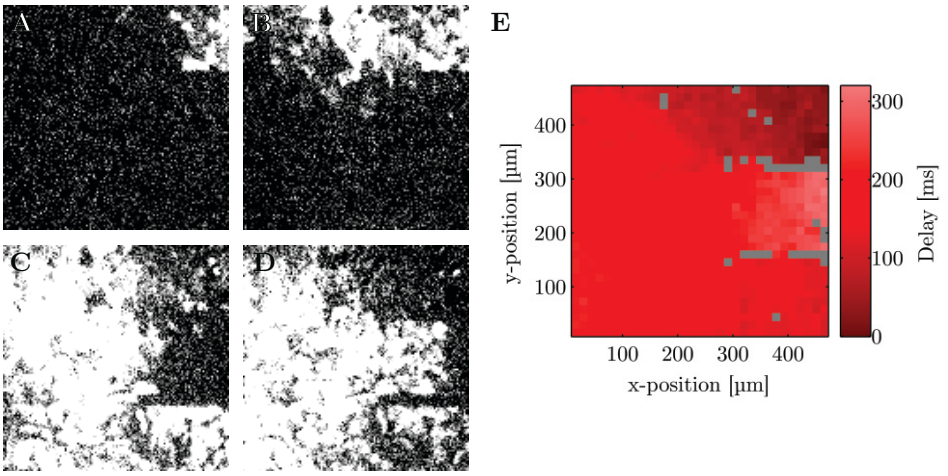

FIGURE 4.23: Ca^{2+} wave entering the region between two wires via the periphery. **A-D:** Corresponding image sequence taken at 0, 80, 160, and 240 ms. The signal reaches the frame from top and bottom right at a similar time point. The corresponding waves then collide and enter the region in between the two wires towards the end of the sequence. **E:** Correlogram of corresponding Ca^{2+} sequence.

Figure 4.23 shows data recorded in the periphery of the array. In this case, the sample was subjected to two horizontal lesions (as visible in Figs. 4.23A-E) and a vertical lesion (to the right of the frame). The image sequence in Figures 4.23A-D corresponds to relative time points of 0, 80, 160, and 240 ms. In this example, the pacemaker has to be located to the right of the vertical lesion and close the horizontal axis of the frame. This is due to the fact that the signal reaches the top and the bottom of the frame at similar time points (i.e. within a time frame of 160 ms). As shown in the correlogram in Figure 4.23E, the waves then collide. This collision can be seen from the region of shared delay values that both signal paths lead to. Subsequently, the signal enters

the area in between the two wires, where the highest delay values can thus be noted.

DISSECTION OF SUBNETWORKS In order to use the method demonstrated above for the dissection of functional subunits from cellular networks, lesions were induced on all four sides of the array. In this way, the resulting center square of viable cells should be isolated from the rest of the culture. The correlation and frequency analyses described above could then be used to examine the center square's activity. To this end, 2 W per wire were applied for 1 min to two neighboring wires at a given edge of the array. After a break of 1 min, the same stimulus was applied to the next edge of the array. After concluding all four edges of the array, the sequence was repeated once as described in the case of the lesion at two sites.

Figures 4.24A-D show an image sequence from a Ca^{2+} imaging video obtained from a sample treated in this way. The images were extracted at relative time points of 0, 220, 440, and 660 ms. As can be seen from the images, the signal originates at a location to the top right of the frame. The signal then propagates through the outer squares via the peripheral coupling described above. The center square, however, does not exhibit activity during this process. Figure 4.24E shows the corresponding correlogram. The signal propagation in the outer squares is visible as described above. The center square, however, is displayed in a different color indicating that the correlation analysis revealed less than 70% correlation with the other squares. This finding is further supported by the plots given in Figures 4.24F-H. Figure 4.24F shows a bar diagram of the interspike intervals of the individual regions. As can be seen, eight of nine regions exhibit identical interspike interval values

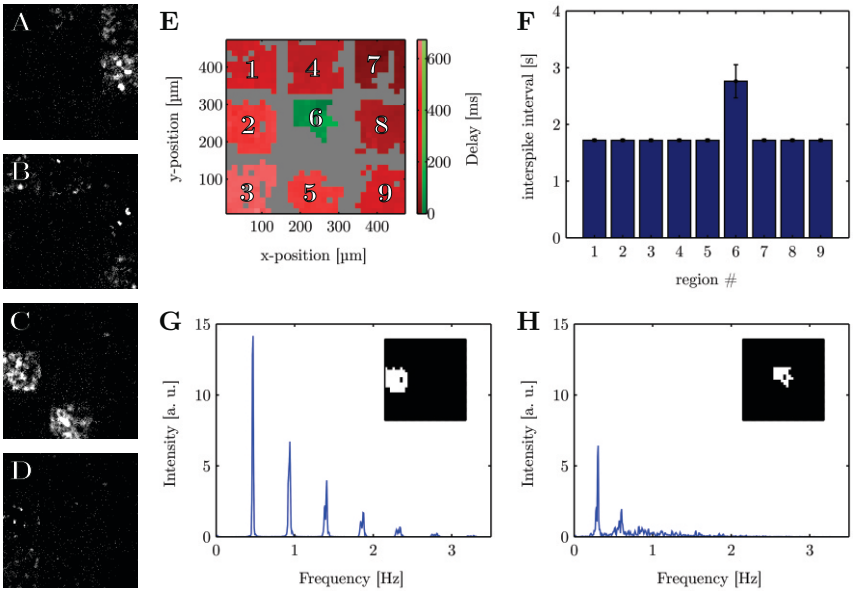

FIGURE 4.24: Ca^{2+} imaging data from an exemplary sample subjected to lesion on four sides of the array. **A-D:** Image sequence from the Ca^{2+} imaging video. The images correspond to relative time points of 0, 220, 440, and 660 ms. The signal propagates from the top right square to the bottom left. The center square, however, is not included in this propagation. **E:** Corresponding correlogram. The signal propagation described for **A-D** is visible in the red group. The green color for the center square indicates that a cross-correlation of less than 70% was detected. **F:** Bar plot of the interspike intervals of the individual regions. Region 6 (the center region) shows a clear deviation, while all other region exhibit identical values. **G** and **H:** PSDs of the left middle and the center square, respectively. As for the interspike intervals, a clear difference in frequency is visible. In addition, the stronger noise in **H** agrees with the higher standard deviation for this region in **F**.

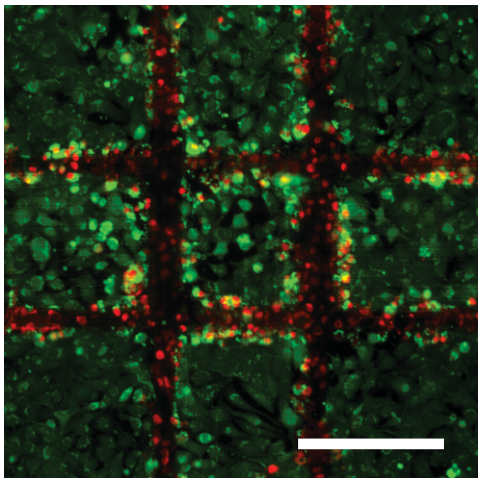

FIGURE 4.25: Live/dead staining of a sample subjected to lesion on all four sides of the array. The red fluorescence (indicating cell death) is limited to the regions directly above the heated wires. The remaining part of the frame indicates viable cells. The center square is clearly isolated and consists of approximately 60 cells. Scale bar: 150 µm.

of approximately 1.8 s (corresponding to a frequency of approximately 0.55 Hz). Region 6 (the center region of the frame), however, clearly deviates from this value by exhibiting an interspike interval of 2.8 s (i.e. 0.35 Hz). This can also be seen in the exemplary PSDs in Figures 4.24G and H. The spectrum in Figure 4.24G corresponds to the left center square of the frame. It shows the characteristics described above and a frequency of approximately 0.5 Hz. The spectrum in Figure 4.24H corresponds to the center square of the frame. In agreement with the interspike analysis, it shows a frequency of approximately 0.3 Hz. In addition, it exhibits more noise, which agrees with the larger standard deviation for this region shown in the bar plot in Figure 4.24F.

As for the lesion at one and two sides, live/dead staining was performed for samples subjected to lesion at four sides, as well. Figure 4.25 shows an exemplary result. As in the case of the single and double lesion, the red fluorescence is limited to the area above the heated wires. This indicates that all but the cell from this region remained viable after the lesion. In addition the figure can give an approximate estimate of the size of the isolated subunit. Depending on the image, cell numbers of 50-80 were counted for these networks.

SUMMARY The present section demonstrated the use of microwire arrays for thermally inducing microscopic lesions at multiple sites inside a cell network cultured on the chip. The signal propagation in the samples after lesion was analyzed using cross-correlation and frequency analyses. In addition, live/dead staining was used to evaluate localized cell death. Using these methods, it was demonstrated that small subunits of <100 cells can be separated from the overall cell layer. The analysis of the data for these samples clearly indicated that the subnetworks remain functionally intact and exhibit activity independent from that of their surrounding.

The lesion precision presented in these experiments is close to the level of individual cells. In principle, the resolution is given by the dimensions of the wire and the thermal properties of the passivation. Using thinner wires that are closer to the surface should yield even steeper temperature gradients. Furthermore, locally varying the cross-sectional dimensions of the wire could be used to restrict the lesions to shorter lines.

Overall, it can be said that the presented methods allow the introduction of lesions with a precision similar to that of conventional

laser-based methods [60–64, 67, 68]. In contrast to microfluidic approaches [15, 65, 66, 69], the samples remain accessible for downstream experiments such as immunohistochemical imaging. At the same time, however, the wires can be integrated into analysis platforms such a multielectrode arrays. This would allow for an integrated platform enabling the study of lesion and successive regeneration in a chip-based and thus easily parallelizable way.

CHAPTER 5

OUTLOOK

5.1 MECHANICAL & CHEMICAL STIMULATION OF CELLS

The previous chapters presented several key aspects of precise on-chip particle handling using microwire arrays. As described in Chapter 1, one of the possible applications of this technique is the chemical and mechanical stimulation of biological cells. The following section is intended to present preliminary results obtained towards this concept.

The techniques presented above allow the defined delivery of stimuli to individual cells via two main pathways. On the one hand, an extracellular signaling molecule (i.e. hormones, neurotransmitters, cytokines, etc.) may be coupled to the particle and delivered to the target cell. Per se, these molecules only require to reach the outer membrane of the cell, where they bind to the corresponding receptors. Here, G protein-coupled receptors (also referred to as seven-transmembrane domain receptors) are of particular interest [125, 126]. These receptors account for the targets of more than 40% of the drugs currently available on the market [127, 128]. Although this demonstrates a wide range of applications to this method, several aspects have to be mentioned. On the one hand, it is not certain whether a particular signaling molecule activates the corresponding receptor when coupled to a magnetic bead. On the other hand, as the beads surface chemistry is used to transduce the stimulus, functionalization to ensure bead mobility at the surface might be limited. Despite these drawbacks, this technique should be applicable to a wide range of biomedical or pharmacological questions.

The second pathway, that can be followed to transmit a chemical stimulus to a given target cell, is cytosolic delivery. This pathway

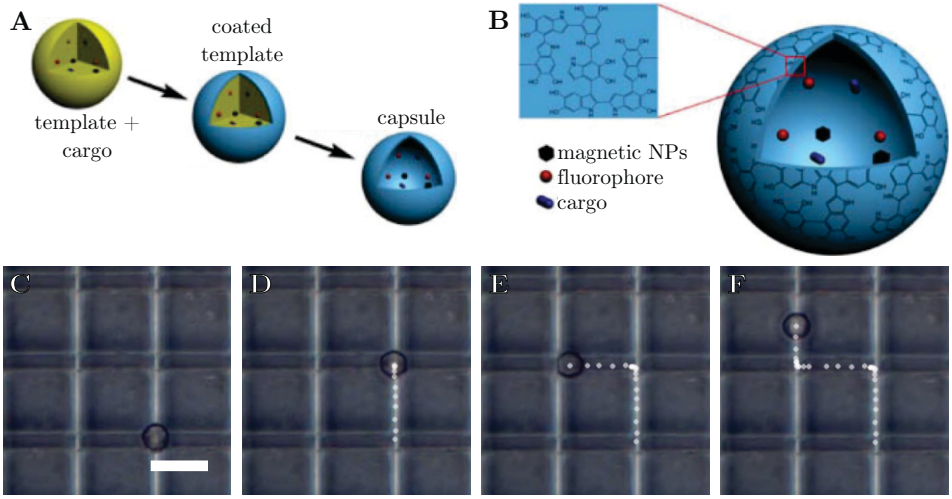

FIGURE 5.1: Polymeric microcapsules as carriers in magnetic delivery with microwire crossbar arrays. **A:** Schematic synthesis of polymer capsules. A template particle carrying the cargo is coated via surface assisted polymerization or layer-by-layer deposition. Subsequent removal of the template material yields the final capsule (Modified an reprinted with permission from [129]). **B:** The capsule cargo can be multi-functional. The capsule can be filled with fluorophores, magnetic particles, and an actual cargo. Apart from the capsule's inside, the shell can also be functionalized by nanoparticle incorporation (Modified an reprinted with permission from [129]). **C-F:** Image series of a polymeric microcapsule being actuated on a microwire crossbar array. The capsule has a diameter of ≈4 µm (Scale bar: 10 µm; Images taken at relative times of 0, 3, 6, and 9 s).

makes use of a magnetically functionalized carrier, that can be used to deliver a molecule into the cytosol of the cell. In this context, possible carriers were tested in preliminary experiments together with the Parak group at the University of Marburg. The carriers tested in these experiments were polymeric capsules. Figures 5.1A and B show schematic of the synthesis and structure of these capsules. Briefly, a template particle is generated by co-precipitating the cargo with e.g. $CaCO_3$. This template particle is then coated via layer-by-layer deposition or surface assisted polymerization. Finally, removal of the template material generates the final capsule carrying the cargo (Fig. 5.1B). These capsules can be equipped with a variety of functionalities. Their shell, for instance, can be rendered bio-degradable or sensitive to light [130–132]. These features render them a particularly versatile tool for intracellular delivery. Several applications, such as intracellular ion-sensing, mRNA delivery, or protein delivery, have already been shown using these capsules [132, 133]. Additionally, the surface chemistry of the capsules can be varied to ensure mobility during magnetic actuation independent of the substrate chemistry necessary to grow a given tape of target cell. Figures 5.1C-F show such a capsule being actuated with a microwire array. Using the methods described above, an individual capsule was deployed into an active magnetic trap. As can be seen from the images, the capsule can be actuated and tracked similar to an individual microparticle. The ability to control individual capsules with subcellular resolution opens up several possibilities. The controlled delivery of a given cargo to a single target cell, for instance, allows more detailed studies of the effects of a given cargo on the target cell and its neighbors. Additionally, the ability to deliver a defined amount of capsules to a target cell with precise control over the timing of the

delivery facilitates the study of uptake kinetics when compared with traditional ensemble experiments.

5.2 ON-CHIP PARTICLE ACTUATION AND TRACKING FOR BIOASSAYS

Apart from the applications described in the previous section, the defined actuation of individual microparticles on a chip opens further experimental possibilities. For instance, the combined actuation and tracking of individual particles could be applied in bioassays as follows.

The simulation of the particle's trajectory as described in Section 3.3.3 approximates the particles velocity by assuming the magnetic force and the viscous drag to be the only notable forces on the particle. Consequently, any particle/surface interaction is neglected. While the results in Section 4.1.2 demonstrate the validity of this assumption, it is most likely not extendable to functionalized beads and surfaces. Any deviation from this model, however, could then be attributed to said interaction. Figures 5.2A and B show a potential application of this concept to measure antibody/antigen interactions.

The measurement of antibody/antigen interactions using could be performed as follows. The overall assay could be performed as a sandwich assay. These assays make use of the fact that different antibodies can bind to different sites on an antigen (referred to as epitopes). Two antibodies against different epitopes of the same antigens can now be coupled to the chip and the bead, respectively. Using the methods described above, a single bead can be deployed, actuated and tracked. From this measurement, the velocity of the particle $\boldsymbol{v}_{\text{particle}}$ can then

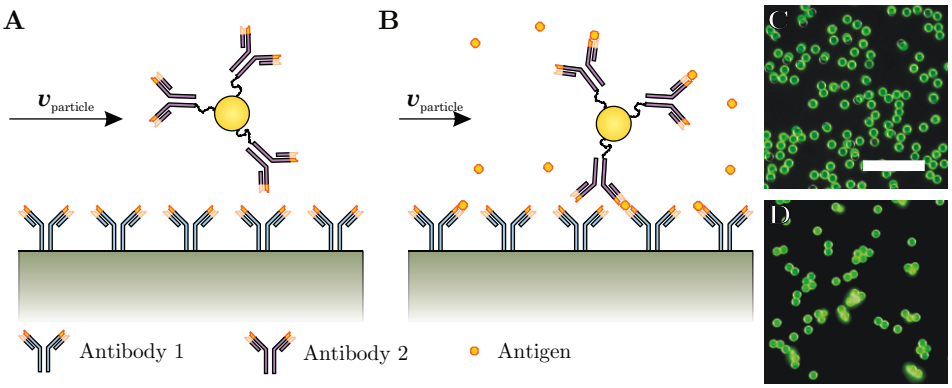

FIGURE 5.2: Immunoassay using single particle actuation and tracking. **A:** A particle functionalized with Antibody 1 is actuated on a chip functionalized with Antibody 2. Based on the tracking procedure described above, its velocity can be measured. **B:** In the presence of a matching antigen, the particle/surface interaction is increased due to a sandwich-type binding. This increased interaction should have an effect on the particle's velocity. **C:** 2.7 µm beads functionalized with fluorescently labeled antibodies. The green fluorescence indicates successful coupling of the antibodies (Scale bar: 25 µm, also corresponds to **D**). **D:** 2.7 µm beads functionalized with non-labeled antibody after incubation with fluorescently labeled antigen. The green fluorescence indicates the antibodies' functionality after coupling.

be obtained. In the presence of the corresponding antigen, this velocity should change due to the enhanced particle/surface interaction (as indicated in Fig. 5.2B).

Figures 5.2C and D show preliminary results for the functionalization of the beads with antibodies. Figure 5.2C shows 2.7 µm beads functionalized with fluorescently labeled antibodies. As can be seen, all beads show a clear and homogeneous signal indicating that the functionalization was successful. In order to test whether the functionality of the antibodies is maintained during functionalization, non-labeled antibodies were coupled to the beads and incubated with fluorescently labeled antigen. The result of such an experiment is shown in Figure 5.2D. As in Figure 5.2C, a clear signal from all beads can be noted. This indicates that the antibodies remain functional after immobilization on the beads. Analogous experiments were performed regarding the functionalization of the chips' surface (data not shown). These experiments also demonstrated the feasibility of the coupling, as well as functionality of the antibodies after immobilization.

Due to the chip-based nature of these experiments, parallelization of such measurements should be straight forward. Using a general antibody for the chip, for instance, and several particles functionalized with different antibodies, multiple parameters could be measured at once. As a result of the precise control over individual beads a decrease in the beads velocity could directly be correlated with a certain antibody. In order to eliminate the necessity to deploy multiple beads through several capillaries (which would have to happen in succession), an opposite approach could also be taken. To this end, the particle would have to be functionalized with a general antibody and multiple antibodies would be coupled to the chip at defined sites. The latter

could be performed using a spotter or microcontact printing in multiple steps. When actuating the particle on the chip, a velocity decrease at a certain position could then be correlated to a specific antibody/antigen reaction.

In summary, this technique could provide an easy-to-fabricate, multiplexed tool to assess the presence of antigens in a given sample. In principle, the sensitivity of this method should mainly depend on the interaction area and the lateral forces applied through the chip. Both of these parameters, however, can be varied in order to achieve a stronger velocity decrease per antibody/antigen interaction.

5.3 ON-CHIP THERMAL LESION FOR STUDIES OF AXOTOMY AND REGENERATION

The results presented in Section 4.2 demonstrate the general applicability of microwire crossbar arrays to induce precise lesions in cell networks cultured on chips. Furthermore, it was demonstrated that these lesions do not heavily affect the functionality of cells in the surrounding. Besides models of cardiac tissue, like the HL-1 cells used in this thesis, the study of other biological networks could benefit from this work.

In particular in the study of neuronal networks, the study of defined lesions is of interest in the context of nerve injury or neurodegenerative diseases [57, 59]. Here, the study of the regeneration of axonal connections after injury (referred to as axotomy in this context) promises wide applicability [59]. Efficient tools that allow lesions restricted to the axon of a neuronal cell are thus of great interest in this field.

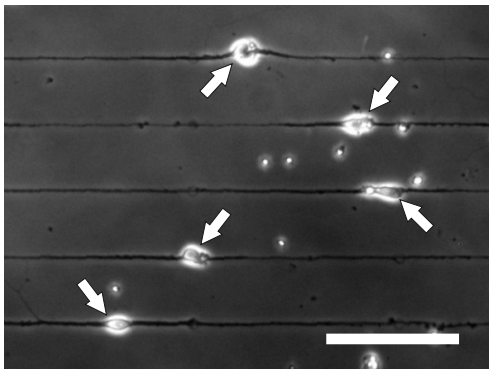

FIGURE 5.3: Rat cortical neurons on microcontact printed protein gradients. As an effect of the underlying protein pattern, the neurites extend along straight lines from the cell bodies (marked with white arrows). Scale bar: 100 µm.

Recently, microfluidic channels that enable axon guiding and severance have been introduced [65, 70, 74]. Due to their microfluidic nature, however, each change in the lesion geometry requires the design and fabrication of new lithography masks and masters. Using an array based approach like the one presented here, could minimize time and labor consumption in these studies.

In order to maintain the defined geometry of the network itself, microcontact printing could be applied. Figure 5.3 shows an exemplary image of rat cortical neurons patterned with this method. It can be seen that the neurites of the cells are well aligned with the protein pattern. Using gradient patterns, it was shown that the position of the cell bodies, as well as the polarity of the neurons can be influenced [134, 135]. When printed onto the microwire arrays in an aligned manner, this system would thus allow to study the effects of thermal lesion with direct control over the lesion site. In contrast to microfluidic

approaches, the relative position of the lesion to the cell body can be controlled.

Overall, this method could provide a flexible tool in the study of lesions in neuronal networks. Reducing the size of the wires could yield a resolution even below that of lasers. At the same time, the approach is directly compatible with chip-based analysis systems, such as multielectrode systems.

References

[1] Coffey, D. Self-organization, complexity and chaos: the new biology for medicine. *Nature Medicine* **4**, 882–885 (1998). URL http://www.nature.com/nm/journal/v4/n8/abs/nm0898-882.html.

[2] Glanz, J. Mastering the nonlinear brain. *Science* **297**, 1758–1760 (1997). URL http://www.sciencemag.org/content/277/5333/1758.short.

[3] Web page of the European Space Agency on Herschel - "How many stars are there in the universe". URL http://www.esa.int/Our_Activities/Space_Science/Herschel/How_many_stars_are_there_in_the_Universe.

[4] Cragg, B. The density of synapses and neurons in normal, mentally defective ageing human brains. *Brain: a journal of neurology* **98**, 81–90 (1975). URL http://europepmc.org/abstract/MED/123474.

[5] Azevedo, F. a. C. *et al.* Equal numbers of neuronal and nonneuronal cells make the human brain an isometrically scaled-up primate brain. *The Journal of comparative neurology* **513**, 532–41 (2009). URL http://www.ncbi.nlm.nih.gov/pubmed/19226510.

[6] Webpage of the Biophysical Society - "What is biophysics?". URL http://www.biophysics.org/ProfessionalDevelopment/

WhatisBiophysics/tabid/2287/Default.aspx.

[7] Hodgkin, A., Huxley, A. & Katz, B. Measurement of the current-voltage relations in the membrane of the giant axon of loligo. *The Journal of physiology* **116**, 424–448 (1952). URL http://www.ncbi.nlm.nih.gov/pmc/articles/PMC1392219/.

[8] Hodgkin, A. & Huxley, A. Currents carried by sodium and potassium ions through the membrane of the giant axon of Loligo. *The Journal of physiology* **116**, 449–472 (1952). URL http://www.ncbi.nlm.nih.gov/pmc/articles/PMC1392213/pdf/jphysiol01447-0082.pdf.

[9] Hodgkin, A. & Huxley, A. The components of membrane conductance in the giant axon of Loligo. *The Journal of physiology* **116**, 473–496 (1952). URL http://jp.physoc.org/content/116/4/473.full.pdf.

[10] Hodgkin, A. & Huxley, A. The dual effect of membrane potential on sodium conductance in the giant axon of Loligo. *The Journal of physiology* **116**, 497–506 (1952). URL http://jp.physoc.org/content/116/4/497.full.pdf.

[11] Hodgkin, A. & Huxley, A. A quantitative description of membrane current and its application to conduction and excitation in nerve. *The Journal of physiology* **117**, 500–544 (1952). URL http://www.ncbi.nlm.nih.gov/pmc/articles/pmc1392413/.

[12] Neher, E. & Sakmann, B. Single-channel currents recorded from membrane of denervated frog muscle fibres. *Nature* **260**, 799–801 (1976). URL http://www.nature.com/nature/journal/v260/n5554/pdf/260799a0.pdf.

[13] Hamill, O., Marty, A., Neher, E., Sakmann, B. & Sigworth, F. Improved patch-clamp techniques for high-resolution current recording from cells and cell-free membrane patches. *Pflügers Archiv - European Journal of Physiology* **391**, 85–100 (1981). URL http://link.springer.com/article/10.1007/BF00656997.

[14] Osterbroek, R. E. & van den Berg, A. *Lab-on-a-chip - Miniaturized systems for (bio)chemical analysis and synthesis* (Elsevier, Amsterdam, 2003), 1st edn.

[15] Dittrich, P. S. & Manz, A. Lab-on-a-chip: microfluidics in drug discovery. *Nature reviews. Drug discovery* **5**, 210–8 (2006). URL http://www.ncbi.nlm.nih.gov/pubmed/16518374.

[16] van den Berg, A. & Bergveld, P. Labs-on-a-Chip: origin, highlights and future perspectives. On the occasion of the 10th microTAS conference. *Lab on a chip* **6**, 1266–73 (2006). URL http://www.ncbi.nlm.nih.gov/pubmed/17102838.

[17] Whitesides, G. M. The origins and the future of microfluidics. *Nature* **442**, 368–73 (2006). URL http://www.ncbi.nlm.nih.gov/pubmed/16871203.

[18] Hutzler, M. High-Resolution Multitransistor Array Recording of Electrical Field Potentials in Cultured Brain Slices. *Journal of Neurophysiology* **96**, 1638–1645 (2006). URL http://jn.physiology.org/cgi/doi/10.1152/jn.00347.2006.

[19] Berdondini, L. *et al.* Active pixel sensor array for high spatio-temporal resolution electrophysiological recordings from single cell to large scale neuronal networks. *Lab on a chip* **9**, 2644–51 (2009). URL http://www.ncbi.nlm.nih.gov/pubmed/19704979.

[20] Frey, U., Egert, U., Heer, F., Hafizovic, S. & Hierlemann, a. Microelectronic system for high-resolution mapping of extracellular electric fields applied to brain slices. *Biosensors & bioelectronics* **24**, 2191–8 (2009). URL http://www.ncbi.nlm.nih.gov/pubmed/19157842.

[21] Huys, R. *et al.* Single-cell recording and stimulation with a 16k micro-nail electrode array integrated on a 0.18 μm CMOS chip. *Lab on a chip* **12**, 1274–80 (2012). URL http://www.ncbi.nlm.nih.gov/pubmed/22337001.

[22] Bakkum, D. J. *et al.* Tracking axonal action potential propagation on a high-density microelectrode array across hundreds of sites. *Nature communications* **4**, 2181 (2013). URL http://www.ncbi.nlm.nih.gov/pubmed/23867868.

[23] Spira, M. E. & Hai, A. Multi-electrode array technologies for neuroscience and cardiology. *Nature nanotechnology* **8**, 83–94 (2013). URL http://www.ncbi.nlm.nih.gov/pubmed/23380931.

[24] Kätelhön, E. *et al.* Nanocavity redox cycling sensors for the detection of dopamine fluctuations in microfluidic gradients. *Analytical chemistry* **82**, 8502–9 (2010). URL http://www.ncbi.nlm.nih.gov/pubmed/20849083.

[25] Yakushenko, A., Kätelhön, E. & Wolfrum, B. Parallel on-chip analysis of single vesicle neurotransmitter release. *Analytical chemistry* **85**, 5483–90 (2013). URL http://www.ncbi.nlm.nih.gov/pubmed/23642073.

[26] Shalek, A. K. *et al.* Vertical silicon nanowires as a universal platform for delivering biomolecules into living cells. *Proceedings of the National Academy of Sciences of the United States of America* **107**, 1870–5 (2010). URL http://www.pubmedcentral.nih.gov/articlerender.fcgi?artid=2836617&tool=pmcentrez&rendertype=abstract.

[27] Peer, E., Artzy-Schnirman, A., Gepstein, L. & Sivan, U. Hollow nanoneedle array and its utilization for repeated administration of biomolecules to the same cells. *ACS nano* **6**, 4940–6 (2012). URL http://www.ncbi.nlm.nih.gov/pubmed/22632128.

[28] Persson, H., Beech, J. & Samuelson, L. Vertical oxide nanotubes connected by subsurface microchannels. *Nano Research* **5**, 190–198 (2012). URL http://link.springer.com/10.1007/s12274-012-0199-0http://link.springer.com/article/10.1007/s12274-012-0199-0.

[29] VanDersarl, J. J., Xu, A. M. & Melosh, N. a. Nanostraws for direct fluidic intracellular access. *Nano letters* **12**, 3881–6 (2012). URL http://www.ncbi.nlm.nih.gov/pubmed/22166016.

[30] Xie, X. *et al.* Nanostraw-electroporation system for highly efficient intracellular delivery and transfection. *ACS nano* **7**, 4351–8 (2013). URL http://www.ncbi.nlm.nih.gov/pubmed/23597131.

[31] Sniadecki, N. J. *et al.* Magnetic microposts as an approach to apply forces to living cells. *Proceedings of the National Academy of Sciences of the United States of America* **104**, 14553–8 (2007). URL http://www.pubmedcentral.nih.gov/articlerender.fcgi?artid=1976246&tool=pmcentrez&rendertype=abstract.

[32] Tseng, P., Judy, J. W. & Di Carlo, D. Magnetic nanoparticle-mediated massively parallel mechanical modulation of single-cell behavior. *Nature methods* **9**, 1113–9 (2012). URL http://www.ncbi.nlm.nih.gov/pubmed/23064517.

[33] Gijs, M. A. M. Magnetic bead handling on-chip: new opportunities for analytical applications. *Microfluidics and Nanofluidics* **1**, 22–40 (2004). URL http://www.springerlink.com/index/10.1007/s10404-004-0010-y.

[34] Gijs, M. A. M. Magnetic Particle Handling in Lab-on-a-Chip Microsystems. *Magnetic Nanostructures in Modern Technology* 153–165 (2008). URL http://www.springerlink.com/index/N563J8HT5J62M435.pdf.

[35] Dobson, J. Magnetic nanoparticles for drug delivery. *Drug development research* **60**, 55–60 (2006). URL http://onlinelibrary.wiley.com/doi/10.1002/ddr.20067/abstract.

[36] Dobson, J. Remote control of cellular behaviour with magnetic nanoparticles. *Nature Nanotechnology* **3**, 139–43 (2008). URL http://www.ncbi.nlm.nih.gov/pubmed/18654485.

[37] Wang, N., Ostuni, E., Whitesides, G. M. & Ingber, D. E. Micropatterning tractional forces in living cells. *Cell motility and the cytoskeleton* **52**, 97–106 (2002). URL http://www.ncbi.nlm.nih.gov/pubmed/12112152.

[38] Irmscher, M., de Jong, A. M., Kress, H. & Prins, M. W. J. Probing the cell membrane by magnetic particle actuation and Euler angle tracking. *Biophysical journal* **102**, 698–708 (2012). URL http://www.pubmedcentral.nih.gov/articlerender.fcgi?artid=3274796&tool=pmcentrez&rendertype=abstract.

[39] Huang, H., Delikanli, S., Zeng, H., Ferkey, D. M. & Pralle, A. Remote control of ion channels and neurons through magnetic-field heating of nanoparticles. *Nature nanotechnology* **5**, 602–6 (2010). URL http://www.ncbi.nlm.nih.gov/pubmed/20581833.

[40] Mannix, R. J. *et al.* Nanomagnetic actuation of receptor-mediated signal transduction. *Nature nanotechnology* **3**, 36–40 (2008). URL http://www.ncbi.nlm.nih.gov/pubmed/18654448.

[41] Bonnemay, L., Hostachy, S., Hoffmann, C., Gautier, J. & Gueroui, Z. Engineering spatial gradients of signaling proteins using magnetic nanoparticles. *Nano letters* **13**, 5147–52 (2013). URL http://www.ncbi.nlm.nih.gov/pubmed/24111679.

[42] Etoc, F. *et al.* Subcellular control of Rac-GTPase signalling by magnetogenetic manipulation inside living cells. *Nature nanotechnology* **8**, 193–8 (2013). URL http://www.ncbi.nlm.nih.gov/pubmed/23455985.

[43] Gosse, C. & Croquette, V. Magnetic tweezers: micromanipulation and force measurement at the molecular level. *Biophysical Journal* **82**, 3314–3329 (2002). URL http://www.pubmedcentral.nih.gov/articlerender.fcgi?artid=1302119&tool=pmcentrez&rendertype=abstract.

[44] Tanase, M., Biais, N. & Sheetz, M. Magnetic tweezers in cell biology. *Methods in cell biology* **83**, 473–93 (2007). URL http://www.ncbi.nlm.nih.gov/pubmed/17613321.

[45] Pohl, H. & Hawk, I. Separation of living and dead cells by dielectrophoresis. *Science* **152**, 647 (1966). URL http://www.sciencemag.org/content/152/3722/647.2.short.

[46] Muller, T., Pfennig, A. & Klein, P. The potential of dielectrophoresis for single-cell experiments. *IEEE Engineering in Medicine and Biology* **22**, 51–61 (2003). URL http://ieeexplore.ieee.org/xpls/abs_all.jsp?arnumber=1266047.

[47] Khoshmanesh, K., Nahavandi, S., Baratchi, S., Mitchell, A. & Kalantar-Zadeh, K. Dielectrophoretic platforms for bio-microfluidic systems. *Biosensors & bioelectronics* **26**, 1800–1814 (2010). URL http://www.ncbi.nlm.nih.gov/pubmed/20933384http://www.ncbi.nlm.nih.gov/pubmed/21244523.

[48] Pethig, R. Dielectrophoresis: Status of the theory, technology, and applications. *Biomicrofluidics* **4** (2010). URL http://www.pubmedcentral.nih.gov/articlerender.fcgi?artid=2917862&tool=pmcentrez&rendertype=abstract.

[49] Morgan, H., Hughes, M. P. & Green, N. G. Separation of submicron bioparticles by dielectrophoresis. *Biophysical journal* **77**, 516–25 (1999). URL http://www.pubmedcentral.nih.gov/articlerender.fcgi?artid=1300348&tool=pmcentrez&rendertype=abstract.

[50] Gascoyne, P. & Vykoukal, J. Particle separation by dielectrophoresis. *Electrophoresis* **77**, 1973–1983 (2002). URL http://www.ncbi.nlm.nih.gov/pmc/articles/PMC2726256/.

[51] Ahn, K. *et al.* Dielectrophoretic manipulation of drops for high-speed microfluidic sorting devices. *Applied Physics Letters* **88**, 024104 (2006). URL http://link.aip.org/link/APPLAB/v88/i2/p024104/s1&Agg=doi.

[52] Kim, U. *et al.* Selection of mammalian cells based on their cell-cycle phase using dielectrophoresis. *Proceedings of the National Academy of Sciences of the United States of America* **104**, 20708–12 (2007). URL http://www.pubmedcentral.nih.gov/articlerender.fcgi?artid=2410067&tool=pmcentrez&rendertype=abstract.

[53] Valero, A. *et al.* Tracking and synchronization of the yeast cell cycle using dielectrophoretic opacity. *Lab on a chip* **11**, 1754–60 (2011). URL http://www.ncbi.nlm.nih.gov/pubmed/21445448.

[54] Manaresi, N. *et al.* A cmos chip for individual cell manipulation and detection. *IEEE Journal of Solid-State Circuits* **38**, 2297–2305 (2003). URL http://ieeexplore.ieee.org/lpdocs/epic03/wrapper.htm?arnumber=1253877.

[55] Hunt, T. P., Issadore, D. & Westervelt, R. M. Integrated circuit/microfluidic chip to programmably trap and move cells and droplets with dielectrophoresis. *Lab on a Chip* **8**, 81–7 (2008). URL http://www.ncbi.nlm.nih.gov/pubmed/18094765.

[56] Chiou, P. Y., Ohta, A. T. & Wu, M. C. Massively parallel manipulation of single cells and microparticles using optical images. *Nature* **436**, 370–2 (2005). URL http://www.ncbi.nlm.nih.gov/pubmed/16034413.

[57] Faweett, J. & Keynes, R. Peripheral nerve regeneration. *Annual review of neuroscience* **13**, 43–60 (1990). URL http://www.annualreviews.org/doi/pdf/10.1146/annurev.ne.13.030190.000355.

[58] Boomkamp, S., Riehle, M. & Wood, J. The development of a rat in vitro model of spinal cord injury demonstrating the additive effects of Rho and ROCK inhibitors on neurite outgrowth and myelination. *Glia* **60**, 441–456 (2012). URL http://onlinelibrary.wiley.com/doi/10.1002/glia.22278/full.

[59] Bradke, F., Fawcett, J. W. & Spira, M. E. Assembly of a new growth cone after axotomy: the precursor to axon regeneration. *Nature reviews. Neuroscience* **13**, 183–93 (2012). URL http://www.ncbi.nlm.nih.gov/pubmed/22334213.

[60] Bargmann, C. I. & Avery, L. Laser killing of cells in Caenorhabditis elegans. *Methods in cell biology* **48**, 225–250 (1995).

[61] Vogel, A. & Venugopalan, V. Mechanisms of pulsed laser ablation of biological tissues. *Chemical reviews* **103**, 577–644 (2003). URL http://www.ncbi.nlm.nih.gov/pubmed/12580643.

[62] Yanik, M., Cinar, H. & Chisholm, A. Functional regeneration after laser axotomy. *Nature* **432**, 822 (2004). URL http://www.nature.com/nature/journal/v432/n7019/abs/432822a.html.

[63] Soustelle, L., Aigouy, B., Asensio, M.-L. & Giangrande, A. UV laser mediated cell selective destruction by confocal microscopy. *Neural development* **3**, 11 (2008). URL http://www.pubmedcentral.nih.gov/articlerender.fcgi?artid=2387153&tool=pmcentrez&rendertype=abstract.

[64] Sweeney, S. T., Hidalgo, A., de Belle, J. S. & Keshishian, H. Setup for functional cell ablation with lasers: coupling of a laser to a microscope. *Cold Spring Harbor protocols* **2012**, 726–32 (2012). URL http://www.ncbi.nlm.nih.gov/pubmed/22661442.

[65] Taylor, A. M. *et al.* Microfluidic Multicompartment Device for Neuroscience Research. *Langmuir : the ACS journal of surfaces and colloids* **19**, 1551–1556 (2003). URL http://www.pubmedcentral.nih.gov/articlerender.fcgi?artid=2923462&tool=pmcentrez&rendertype=abstract.

[66] Park, J. W., Vahidi, B., Taylor, A. M., Rhee, S. W. & Jeon, N. L. Microfluidic culture platform for neuroscience research. *Nature protocols* **1**, 2128–36 (2006). URL http://www.ncbi.nlm.nih.gov/pubmed/17487204.

[67] Guo, S., Bourgeois, F., Chokshi, T. & Durr, N. Femtosecond laser nanoaxotomy lab-on-a-chip for in vivo nerve regeneration studies. *Nature ...* **5**, 531–533 (2008). URL http://www.nature.com/nmeth/journal/v5/n6/abs/nmeth.1203.html.

[68] Kim, Y.-t., Karthikeyan, K., Chirvi, S. & Davé, D. P. Neuro-optical microfluidic platform to study injury and regeneration of single axons. *Lab on a chip* **9**, 2576–81 (2009). URL http://www.ncbi.nlm.nih.gov/pubmed/19680581.

[69] Park, J. W., Kim, H. J., Kang, M. W. & Jeon, N. L. Advances in microfluidics-based experimental methods for neuroscience research. *Lab on a chip* **13**, 509–21 (2013). URL http://www.ncbi.nlm.nih.gov/pubmed/23306275.

[70] Taylor, A., Blurton-Jones, M. & Rhee, S. A microfluidic culture platform for CNS axonal injury, regeneration and transport. *Nature methods* **2**, 599–605 (2005). URL http://www.nature.com/nmeth/journal/v2/n8/abs/nmeth777.html.

[71] Yang, I. H., Siddique, R., Hosmane, S., Thakor, N. & Höke, A. Compartmentalized microfluidic culture platform to study mechanism of paclitaxel-induced axonal degeneration. *Experimental neurology* **218**, 124–8 (2009). URL http://www.ncbi.nlm.nih.gov/pubmed/19409381.

[72] Taylor, A. M. *et al.* Axonal mRNA in uninjured and regenerating cortical mammalian axons. *The Journal of neuroscience : the official journal of the Society for Neuroscience* **29**, 4697–707 (2009). URL http://www.pubmedcentral.nih.gov/articlerender.fcgi?artid=3632375&tool=pmcentrez&rendertype=abstract.

[73] Kilinc, D. *et al.* Wallerian-Like Degeneration of Central Neurons After Synchronized and Geometrically Registered Mass Axotomy in a Three-Compartmental Microfluidic Chip. *Neurotoxicity Research* **19**, 149–161 (2010). URL http://link.springer.com/10.1007/s12640-010-9152-8.

[74] Deleglise, B. *et al.* Synapto-protective drugs evaluation in reconstructed neuronal network. *PloS one* **8**, e71103 (2013). URL http://www.pubmedcentral.nih.gov/articlerender.fcgi?artid=3745451&tool=pmcentrez&rendertype=abstract.

[75] Lee, C. S., Lee, H. & Westervelt, R. M. Microelectromagnets for the control of magnetic nanoparticles. *Applied Physics Letters* **79**, 3308–3310 (2001). URL http://link.aip.org/link/APPLAB/v79/i20/p3308/s1/html.

[76] Lee, H., Purdon, A. M. & Westervelt, R. M. Manipulation of biological cells using a microelectromagnet matrix. *Applied Physics Letters* **85**, 1063–1065 (2004). URL http://link.aip.org/link/APPLAB/v85/i6/p1063/s1&Agg=doi.

[77] Lee, H., Purdon, A. M. & Westervelt, R. M. Micromanipulation of Biological Systems with Microelectromagnets. *IEEE Transactions on Magnetics* **40**, 2991–2993 (2004). URL http://ieeexplore.ieee.org/lpdocs/epic03/wrapper.htm?arnumber=1325709.

[78] Lee, H., Hunt, T. P. & Westervelt, R. M. Magnetic and electric manipulation of a single cell in fluid. In *Material Research Society Symp*, vol. 820, 1–8 (2004). URL http://meso.deas.harvard.edu/papers/Lee,MRS82002.3.1(2004).pdf.

[79] Wikitionary entry on "-phoresis". URL http://en.wiktionary.org/wiki/phoresis.

[80] Wikipedia entry on "Magnet". URL http://en.wikipedia.org/wiki/Magnet.

[81] Wikipedia entry "Magnetic field". URL http://en.wikipedia.org/wiki/Magnetic_field.

[82] Panofsky, W. K. H. & Phillips, M. *Classical Electricity and Magnetism* (Addison-Wesley Publishing Company, Reading, Massachusetts, 1962), 2nd edn.

[83] Demtröder, W. *Experimentalphysik 2 - Elektrizität und Optik* (Springer-Verlag, Heidelberg, 2004), 2nd edn.

[84] Fließ bach, T. *Elektrodynamik* (Spektrum Akademischer Verlag, Heidelberg, 2008), 5th edn.

[85] Wolfram Alpha. URL http://www.wolframalpha.com.

[86] Wikipedia entry "Diamagnetism". URL http://en.wikipedia.org/wiki/Diamagnet.

[87] Wikipedia entry "Paramagnetism". URL http://en.wikipedia.org/wiki/Paramagnetism.

[88] Wikipedia entry "Tungsten". URL http://en.wikipedia.org/wiki/Tungsten.

[89] Wikipedia entry "Aluminum". URL http://en.wikipedia.org/wiki/Aluminum.

[90] Wikipedia entry "Lithium". URL http://en.wikipedia.org/wiki/Lithium.

[91] Wikipedia entry "Magnesium". URL http://en.wikipedia.org/wiki/Magnesium.

[92] Wikipedia entry "Sodium". URL http://en.wikipedia.org/wiki/Sodium.

[93] Chikazumi, S. *Physics of Ferromagnetism* (Oxford University Press, New York, 1997), 2nd edn.

[94] Bean, C. P. & Livingston, J. D. Superparamagnetism. *Journal of Applied Physics* **30**, S120 (1959). URL http://scitation.aip.org/content/aip/journal/jap/30/4/10.1063/1.2185850.

[95] Bean, C. P. Hysteresis Loops of Mixtures of Ferromagnetic Micropowders. *Journal of Applied Physics* **26**, 1381 (1955). URL http://scitation.aip.org/content/aip/journal/jap/26/11/10.1063/1.1721912.

[96] Jackson, J. D. *Classical Electrodynamics* (John Wiley & Sons, Inc., New York, 1999), 3rd edn.

[97] Pohl, H. a. The Motion and Precipitation of Suspensoids in Divergent Electric Fields. *Journal of Applied Physics* **22**, 869 (1951). URL http://scitation.aip.org/content/aip/journal/jap/22/7/10.1063/1.1700065.

[98] Wikipedia entry "Relative Permittivity". URL http://en.wikipedia.org/wiki/Relative_permittivity.

[99] Ashcroft, N. W. & Mermin, N. D. *Solid State Physics* (Holt, Rinehart, and Wilson, New York, 1996), 1st edn.

[100] Kittel, C. *Introduction to Solid State physics* (John Wiley & Sons, Inc., Hoboken, New Jersey, 2005), 8th edn.

[101] Wikipedia entry "Free electron gas". URL http://en.wikipedia.org/wiki/Free_electron_gas.

[102] Debye, P. Zur theorie der spezifischen wärmen. *Annalen der Physik* **344**, 789–839 (1912). URL http://onlinelibrary.wiley.com/doi/10.1002/andp.19123441404/abstract.

[103] Huang, K. *Introduction to Statistical Physics* (CRC Press, Boca Rota, Florida, 2001), 2nd edn.

[104] Fließ bach, T. *Statistische Physik* (Spektrum Akademischer Verlag, Heidelberg, 2010), 5th edn.

[105] Müller, C. B., Weiss, K., Loman, A., Enderlein, J. & Richtering, W. Remote temperature measurements in femto-liter volumes using dual-focus-Fluorescence Correlation Spectroscopy. *Lab on a chip* **9**, 1248–53 (2009). URL http://www.ncbi.nlm.nih.gov/pubmed/19370244.

[106] van Munster, E. B. & Gadella, T. W. J. Fluorescence lifetime imaging microscopy (FLIM). *Advances in Biochemical Engineering* **95**, 143–175 (2005). URL http://link.springer.com/chapter/10.1007/b102213.

[107] Bers, D. Cardiac excitation–contraction coupling. *Nature* **415** (2002). URL http://www.nature.com/nature/journal/v415/n6868/abs/415198a.html.

[108] Wikipedia entry "Myofilament". URL http://en.wikipedia.org/wiki/Myofilament.

[109] Claycomb, W. C. *et al.* HL-1 cells: a cardiac muscle cell line that contracts and retains phenotypic characteristics of the adult cardiomyocyte. *Proceedings of the National Academy of Sciences of the United States of America* **95**, 2979–84 (1998). URL http://www.pubmedcentral.nih.gov/articlerender.fcgi?artid=19680&tool=pmcentrez&rendertype=abstract.

[110] Takahashi, A., Camacho, P., Lechleiter, J. D. & Herman, B. Measurement of intracellular calcium. *Physiological reviews* **79**, 1089–125 (1999). URL http://www.ncbi.nlm.nih.gov/pubmed/10508230.

[111] Grynkiewicz, G., Poenie, M. & Tsien, R. Y. A new generation of Ca2+ indicators with greatly improved fluorescence properties. *The Journal of biological chemistry* **260**, 3440–50 (1985). URL http://www.ncbi.nlm.nih.gov/pubmed/3838314.

[112] Tsien, R. A non-disruptive technique for loading calcium buffers and indicators into cells. *Nature* **290**, 527–528 (1981). URL http://www.nature.com/nature/journal/v290/n5806/abs/290527a0.html.

[113] Rinklin, P., Krause, H.-J. & Wolfrum, B. On-chip control of magnetic particles. *Physica Status Solidi (a)* **209**, 871–874 (2012). URL http://doi.wiley.com/10.1002/pssa.201100529.

[114] Otsu, N. A Threshold Selection Method from Gray-Level Histograms. *IEEE Transactions on Systems, Man, and Cybernetics* **SMC-9**, 62–66 (1979).

[115] Rinklin, P., Krause, H.-J. & Wolfrum, B. Actuation and tracking of a single magnetic particle on a chip. *Applied Physics Letters*

100, 014107 (2012). URL http://link.aip.org/link/APPLAB/v100/i1/p014107/s1&Agg=doi.

[116] Wang, Z. H., Lew, W. S. & Bland, J. A. C. Manipulation of superparamagnetic beads using on-chip current lines placed on a ferrite magnet. *Journal of Applied Physics* **99**, 08P104 (2006). URL http://link.aip.org/link/JAPIAU/v99/i8/p08P104/s1&Agg=doi.

[117] Fonnum, G., Johansson, C., Molteberg, A., Morup, S. & Aksnes, E. Characterisation of Dynabeads by magnetization measurements and Mössbauer spectroscopy. *Journal of Magnetism and Magnetic Materials* **293**, 41–47 (2005). URL http://linkinghub.elsevier.com/retrieve/pii/S030488530500106X.

[118] Klein, L. & Swift, C. An improved model for the dielectric constant of sea water at microwave frequencies. *Antennas and Propagation, IEEE ...* **AP-25**, 104–111 (1977). URL http://ieeexplore.ieee.org/xpls/abs_all.jsp?arnumber=1141539.

[119] Mercer, F. & Goodman, T. Effect of structural features and humidity on the dielectric constant of polyimides. *High Performance Polymers* **3**, 297–310 (1991). URL http://hip.sagepub.com/content/3/4/297.short.

[120] Liu, C., Lagae, L. & Borghs, G. Manipulation of magnetic particles on chip by magnetophoretic actuation and dielectrophoretic levitation. *Applied Physics Letters* **90**, 184109 (2007). URL http://link.aip.org/link/APPLAB/v90/i18/p184109/s1&Agg=doi.

[121] Rida, a., Fernandez, V. & Gijs, M. a. M. Long-range transport of magnetic microbeads using simple planar coils placed in a uniform magnetostatic field. *Applied Physics Letters* **83**, 2396 (2003). URL http://scitation.aip.org/content/aip/journal/apl/83/12/10.1063/1.1613038.

[122] Shah, U., Bien, H. & Entcheva, E. Cardiac arrhythmogenesis and temperature. In *Conference proceedings : ... Annual International Conference of the IEEE Engineering in Medicine and Biology Society. IEEE Engineering in Medicine and Biology Society. Conference*, vol. 1, 841–4 (2006). URL http://www.ncbi.nlm.nih.gov/pubmed/17946861.

[123] Giovangrandi, L., Gilchrist, K. H., Whittington, R. H. & T.A. Kovacs, G. Low-cost microelectrode array with integrated heater for extracellular recording of cardiomyocyte cultures using commercial flexible printed circuit technology. *Sensors and Actuators B: Chemical* **113**, 545–554 (2006). URL http://linkinghub.elsevier.com/retrieve/pii/S0925400505003485.

[124] Emohare, O., Hafez, M. I., Sandison, A., Coombs, R. R. H. & McCarthy, I. D. Laser-induced thermal stress and the heat shock response in neural cells. *Acta orthopaedica Scandinavica* **75**, 610–7 (2004). URL http://www.ncbi.nlm.nih.gov/pubmed/15513496.

[125] Pierce, K. L., Premont, R. T. & Lefkowitz, R. J. Seven-transmembrane receptors. *Nature reviews. Molecular cell biology* **3**, 639–50 (2002). URL http://www.ncbi.nlm.nih.gov/pubmed/12209124.

[126] Rosenbaum, D. M., Rasmussen, S. r. G. F. & Kobilka, B. K. The structure and function of G-protein-coupled receptors. *Nature* **459**, 356–63 (2009). URL http://www.ncbi.nlm.nih.gov/pubmed/19458711.

[127] Filmore, D. It's a GPCR world. *Modern Drug Discovery* **7**, 24–27 (2004). URL http://pubs.acs.org/subscribe/archive/mdd/v07/i11/html/1104feature_filmore.html.

[128] Overington, J. P., Al-Lazikani, B. & Hopkins, A. L. How many drug targets are there? *Nature reviews. Drug discovery* **5**, 993–6 (2006). URL http://www.ncbi.nlm.nih.gov/pubmed/17139284.

[129] Cui, J. *et al.* Monodisperse Polymer Capsules: Tailoring Size, Shell Thickness, and Hydrophobic Cargo Loading via Emulsion Templating. *Advanced Functional Materials* **20**, 1625–1631 (2010). URL http://doi.wiley.com/10.1002/adfm.201000209.

[130] Rivera-Gil, P., De Koker, S., De Geest, B. G. & Parak, W. J. Intracellular processing of proteins mediated by biodegradable polyelectrolyte capsules. *Nano letters* **9**, 4398–402 (2009). URL http://www.ncbi.nlm.nih.gov/pubmed/19860453.

[131] Carregal-Romero, S., Ochs, M. & Parak, W. J. Nanoparticle-functionalized microcapsules for in vitro delivery and sensing. *Nanophotonics* **1**, 171–180 (2012). URL http://www.degruyter.com/view/j/nanoph.2012.1.issue-2/nanoph-2012-0014/nanoph-2012-0014.xml.

[132] Ochs, M. *et al.* Light-Addressable Capsules as Caged Compound Matrix for Controlled Triggering of Cytosolic Reactions. *Angewandte Chemie* **125**, 723–727 (2013). URL http://doi.wiley.com/10.1002/ange.201206696.

[133] del Mercato, L. L., Abbasi, A. Z., Ochs, M. & Parak, W. J. Multiplexed sensing of ions with barcoded polyelectrolyte capsules. *ACS nano* **5**, 9668–74 (2011). URL http://www.ncbi.nlm.nih.gov/pubmed/22053744.

[134] Fricke, R. *et al.* Axon guidance of rat cortical neurons by microcontact printed gradients. *Biomaterials* **32**, 2070–6 (2011). URL http://www.ncbi.nlm.nih.gov/pubmed/21167596.

[135] Albers, J., Offenhäusser, A. & Meffert, S. Control of neuronal signal propagation by microstructured protein gradients. *in submission* (2014).

Author's list of publications

- Rinklin, P., Krause, H.-J. & Wolfrum, B. Actuation and tracking of a single magnetic particle on a chip. *Applied Physics Letters*, 100(1), 014107 (2012). doi:10.1063/1.3673909
- Rinklin, P., Krause, H.-J. & Wolfrum, B. On-chip control of magnetic particles. *Physica Status Solidi (a)*, 209(5), 871-874 (2012). doi:10.1002/pssa.201100529
- Carregal-Romero, S., Rinklin, P., Schulze, S., Schäfer, M., Ott, A., Hühn, D. & Parak, W. J. Ion Transport Through Polyelectrolyte Multilayers. *Macromolecular Rapid Communications*, 34(23-24), 1820-1826 (2013). doi:10.1002/marc.201300571
- Rinklin, P., Afanasenkau, D., Wiegand, S., Offenhäusser, A. & Wolfrum, B. Inducing microscopic thermal lesions for the dissection of functional cell networks on a chip. *in submission*

Danksagung

Das Verfassen der vorliegenden Arbeit sowie die dazu durchgeführte Forschung wäre mir allein nicht möglich gewesen. Für rat- und tatkräftige Unterstützung bedanke ich mich bei folgenden Personen:

- Prof. Dr. Bernhard Wolfrum danke ich für die Vergabe des Themas sowie die herausragende Betreuung. Seine stete Verfügbarkeit für Gespräche fachlicher Natur sowie das Gewähren weitreichenden Freiraums die Arbeit betreffend machen dem Begriff *Doktorvater* alle Ehre. Ebenso schätzte ich die zahlreichen Gesprächen allgemeiner Natur bei den noch zahlreicheren Treffen an der Kaffeemaschine oder auf dem Flur.

- Prof. Dr. Jörg Fitter danke ich für die Übernahme der Zweitbegutachtung meiner Arbeit.

- Prof. Dr. Andreas Offenhäusser danke ich für die Leitung unseres Institutes (ICS-8) und für die Leitung unseres Institutes (PGI-8). Seine stoische Haltung gegenüber den bürokratischen Wirren des akademischen Alltags ermöglicht die Institutsatmosphäre, die ich seit Beginn meiner Zeit in Jülich schätze.

- Marko Banzet danke ich für die Prozessierung der zahlreichen Wafer, die im Laufe der Arbeit gebraucht wurden. Sein sprühender Frohmut erhellt jeden frühen Morgen die Kaffeeküche.

- Norbert Wolters und dem Team der Elektronikwerkstatt (insbesondere Nadine Neumann) danke ich für den Bau der "Box". Ohne ihre Flexibilität im Verständnis meines "kreativen" Elektronikjargons sowie die zeitnahe Umsetzung aller Arbeiten wären viele der hier vorgestellten Experimente nicht möglich gewesen.

- Dieter Strobl und dem Team der mechanischen Werkstatt danke ich für die flexible und kompetente Unterstützung beim Bau des Chiphalters.

- Meiner Verlobten und baldigen Mutter unseres gemeinsamen Sohnes danke ich für alles! Insbesondere in der schweren Zeit vor dem Fertigwerden dieser Arbeit war sie mir eine große Stütze und ich bin stolz darauf weiterhin mit ihr durch dick und dünn gehen zu dürfen.

- Dzmitry Afanasenkau und Simone Wiegand danke ich für die Unterstützung und Durchführung der FLIM-Messungen sowie für die Zusammenarbeit an unserem Paper.

- Bettina Breuer und Rita Fricke danke ich für das Zusammenhalten des Laboralltags und die Tatsache, dass beinahe kein Besuch im Labor ohne Lächeln verging.

- Susanne Bippus danke ich für das verlässliche Kennen des kürzesten Dienstweges.

- Jan Schnitker danke ich für die zahlreichen Gespräche fachlicher und allgemeiner Natur. Für die ständige Bereitschaft zu einem Gespräch und das "Abkurbeln" der stressigen Tage sage ich herzlich: "01000100011000010110111001101011011001010010000 1"

- I would like to thank Francesca Santoro for the insight into the delightful Italian culture and its absolutely non-aggressive food. I always enjoyed the "fresh air" air when I still needed it.

- Volker Schöps danke ich für das dicke Fell, das man als mein Büronachbar braucht.

- Jonas Albers danke ich für die reichhaltige Matlab-Beratung und das Bereitstellen der Mikroskopaufnahmen in Figure 5.3.

- Wenfang Li danke ich für die erfolgreiche Zusammenarbeit und das Bereitstellen der Mikroskopaufnahmen in Figure 5.2.

I would also like to thank all the wonderful people I met in our group and in the institute that contribute to the inspiring work atmosphere (in particular Dzmitry Afanasenkau, Janis Brusius, Martin Hüske, Boris Hofmann, Enno Kätelhön, Vanessa Maybeck, Dirk Mayer, Koji Toma, Alexey Yakushenko). After more than four years in our institute it is still a joy to come to work everyday and for this I would like to thank you all.

Ich möchte an dieser Stelle auch meinen Eltern und meiner Familie danken, ohne die ich nicht der geworden wäre, der ich bin.

Band / Volume 87
Submolecular imaging with single particle atomic force sensors
G. Kichin (2014), 140 pp
ISBN: 978-3-89336-976-8

Band / Volume 88
Multiscale Multimodel Simulation of Micromagnetic Singularities
C. Andreas (2014), xix, 188 pp
ISBN: 978-3-89336-983-6

Band / Volume 89
***Ab initio* description of transverse transport due to impurity scattering in transition-metals**
B. C. Zimmermann (2014), 164 pp
ISBN: 978-3-89336-985-0

Band / Volume 90
Ladungstransport durch Graphenschichten und GaAs-Nanodrähte untersucht mit einem Multispitzen-Rastertunnelmikroskop
S. Korte (2014), 96 pp
ISBN: 978-3-89336-990-4

Band / Volume 91
6th Georgian-German School and Workshop in Basic Science
A. Kacharava (Ed.) (2014), CD
ISBN: 978-3-89336-991-1

Band / Volume 92
Ab initio investigations of π-conjugated-molecule-metal interfaces for molecular electronics and spintronics
M. Callsen (2014), viii, 155 pp
ISBN: 978-3-89336-992-8

Band / Volume 93
Ladungstransportmessungen an Si(111) Oberflächen mit einem Multispitzen-Rastertunnelmikroskop
M. Blab (2014), iv, 132, X pp
ISBN: 978-3-89336-997-3

Band / Volume 94
Functional Soft Matter
Lecture Notes of the 46th IFF Spring School 2015
23 February – 06 March, 2015 Jülich, Germany
ed. by J. Dhont, G. Gompper, G. Meier, D. Richter, G. Vliegenthart, R. Zorn
(2015), ca. 600 pp
ISBN: 978-3-89336-999-7

Band / Volume 95
2-Steps in 1-pot: enzyme cascades for the synthesis of chiral vicinal amino alcohols
T. Sehl (2014), XIV, 167 pp
ISBN: 978-3-95806-001-2

Band / Volume 96
Immunohistochemical and electrophysiological characterization of the mouse model for Retinitis Pigmentosa, *rd10*
S. Biswas (2014), XII, 119 pp
ISBN: 978-3-95806-011-1

Band / Volume 97
Single molecule localization microscopy: Imaging of cellular structures and a new three-dimensional localization technique
X. Fan (2014), XII, 92 pp
ISBN: 978-3-95806-014-2

Band / Volume 98
Cryogenic Break-Junction Characterization of Single Organic Molecules
T. Grellmann (2014), VI, 86 pp
ISBN: 978-3-95806-015-9

Band / Volume 99
Interacting Interactions: A Study on the Interplay of Molecule-Molecule and Molecule-Substrate Interactions at Metal-Organic Interfaces
M. Willenbockel (2014), IX, 245 pp
ISBN: 978-3-95806-018-0

Band / Volume 100
Microwire crossbar arrays for chemical, mechanical, and thermal stimulation of cells
P. Rinklin (2015), xii, 184 pp
ISBN: 978-3-95806-022-7

Weitere ***Schriften des Verlags im Forschungszentrum Jülich*** unter
http://wwwzb1.fz-juelich.de/verlagextern1/index.asp

Schlüsseltechnologien /
Key Technologies
Band / Volume 100
ISBN 978-3-95806-022-7